APPLIED
PHYSICS

Applied Physics
2025, No. 6

The journal was founded in 1994

The scientific and technical peer-reviewed journal is intended for the publication of articles on the latest achievements in the field of physics with prospects for advancements (technical and scientific) applications.

The periodicity is 6 issues per year.

Editor-in-Chief

Igor Burlakov,
Dr. Sci. (Eng.), Professor,
Research, Development and Production Center ORION, Joint-Stock Company – Russian Federation State Science Center

C O N T E N T S

PHYSICAL EQUIPMENT AND ITS ELEMENTS

INFORMATION

The effect of defects in oxide layers on the performance of silicon photodiodes

K. O. Boltar[1,2], M. N. Vildyaeva[1], S. S. Demidov[1], E. A. Klimanov[1,3,*], D. S. Molchanov[1],
E. A. Makarova[1], K. A. Popov[1], A. A. Zhukovich-Gardeeva[1], and A. V. Egorov[1]

[1] *RD&P Center ORION, JSC, Moscow, 111538 Russia*
[*] *E-mail: klimanov3@mail.ru*
[2] *Moscow Institute of Physics and Technology, Moscow Region, Dolgoprudny, 141701 Russia*
[3] *MIREA – Russian Technological University, Moscow, 119454 Russia*

***The mechanism of leakage current formation in p+-n junctions of photodiodes in the presence
of local defects is investigated. The patterns of formation of local defects in dielectric layers are
considered in order to determine the conditions that reduce their density. On n-type
monocrystalline silicon (Cz-Si) wafers with a diameter of 100 mm and a resistivity of
4–5 ohms.cm and orientation (100) were used to produce elements with a pad size of
1.4×1.4 mm². The manufacturing process cycle included the operations of oxidation in
$H_2O + HCl$ vapors, photolithography, corralling (precipitation) of boron from BN, boron
diffusion and phosphorus diffusion in various modes. Both liquid sources $POCL_3$ and PCL_3
and solid sources – aluminum metaphasate (MFA) ($Al_2O_3, 3P_2O_5$) plates were used as a
diffusant source during phosphorus diffusion. It has been established that the current-voltage
characteristic of silicon photodiodes with anomalous "soft" characteristics is determined by
the tunneling current flow mechanism. The use of optimal gettering modes leads to a sharp
decrease in the number of photosensitive elements with anomalous current-voltage
characteristic.***

Keywords: silicon photodiodes; monocrystalline silicon; defects; current-voltage characteristics.

Introduction

The cycle of manufacturing silicon photodiodes typically involves the diffusion of high concentrations of boron and phosphorus to form *p–n* junctions and doped regions. The process of phosphorus diffusion often leads to the formation of local defects in the dielectric layers acting as a protective mask [1–3]. These defects can lead to the formation of local n^+-channels in p^+–*n* junctions and defects on the silicone surface causing leak currents ("soft" volt-ampere characteristics) resulting in the increase of photodiodes noise, including low-frequency ones with 1/*f* type spectrum.

Paper [4] considers the patterns of formations of these defects to determine conditions reducing their density.

The purpose of this paper is to study the mechanism of formation of leak points in p^+–*n* junctions of photodiodes if the specified defects are present.

Experiment

Photosensitive elements (FSE) with a pad size of 1.4×1.4 mm² were manufactured on the *n*-type monocrystalline silicon (Cz-Si) plates with a diameter of 100 mm and specific resistance of 4–5 Ω·cm and orientation (100). Process cycle of

manufacturing included the processes of oxidation in H_2O + Hcl vapors, photolithography, pre-depositon (precipitation) of boron from BN, boron and phosphorus diffusion in different modes.

Both liquid $POCL_3$ and PCL solid sources such as aluminum metaphosphate plates ($Al_2O_3/3P_2O_5$) were used as a diffusant source during phosphorus diffusion.

The concentration and distribution of local defects over the plate were determined on the manufactured samples using an optical microscope. Optical, atomic-force microscope and REM were used to determine the dimensions and shape of defects. The manufactured samples were used to measure volt-ampere characteristics (VAC) of PSE in the temperature range from –60 °C to +70 °C and reverse voltage from 0.01 V to 20 V.

Results

Part of the samples showed a significant increase of dark currents (I_d) with the increase of reverse bias ("soft" VAC). To determine the causes of this phenomenon, measurements of VAC were carried out on such PSE in the temperature range from –60 °C to +70 °C and reverse voltage from 0.01 V to 20 V, the results are shown in fig. 1. The obtained results show a weakening of the temperature dependence of the dark current with the increase of reverse voltage and its near absence with large leak currents (voltage 20 V).

To determine the nature of the I_d except for reverse voltage, the VAC was plotted in I_d/V coordinates from $V^{-1/2}$ (fig. 2) which demonstrated a transition from the area with dependence $I_d \sim V^{1/2}$ characteristic of the generating current, to an area with exponential current increase.

Fig. 3 shows VAC in the area of "soft" characteristics at two temperatures (–60 °C and 25 °C) confirming exponential dependence of current on voltage and its weak dependence on temperature.
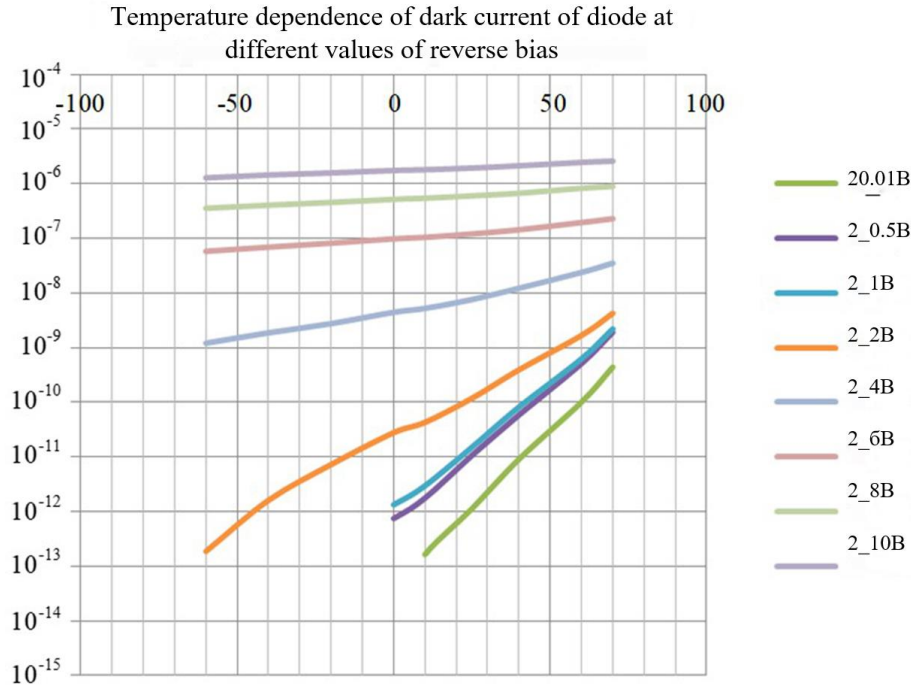
Fig. 1. Temperature dependencies of the current at different bias voltages
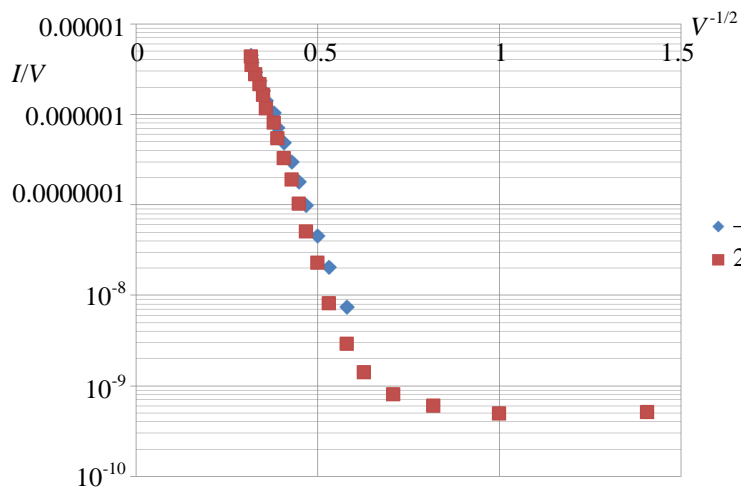
Fig. 2. Current dependence on voltage at temperatures of –60 °C and 25 °C in the voltage range of 0.4–10 V

$T = -60\ °C$

$y = 0.0095e^{-24.37x}$
$R^2 = 0.9985$

◆   2.65E-0,9

—— Exponential (2.65E-0,9)

a)

$T = -25\ °C$

$y = 0.0312e^{-28.19x}$
$R^2 = 0.998$

◆ Range 1

—— Exponential (Range 1)

b)
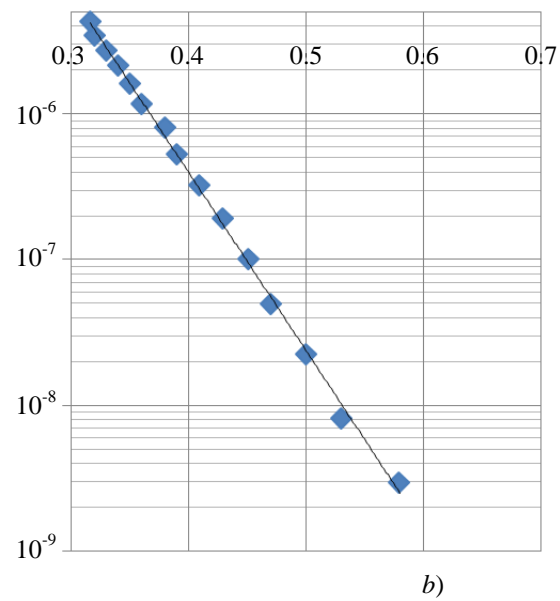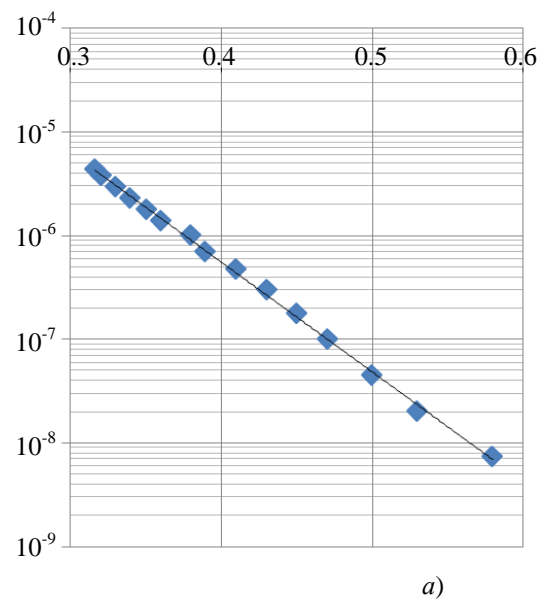
Fig. 3. Tunneling current dependence on voltage at temperatures of –60 °C and 25 °C in the voltage range of 3–10 V

Discussion of the results

Obtained dependencies of dark current on reverse voltage in the area of exponential growth indicate a tunneling mechanism of current flow.

Indeed, a known expression for the tunneling current is as follows [5]:

$$I = AE^2 \exp\left(-B/E\right) \qquad (1)$$

where E is the electric field strength; A, B – coefficients poorly depending on the electric field.

Dependence of the electric field in the sharp p^+–n-junction E on the voltage V if there are local areas with increased field voltage, can be represented as follows [6]:

$$E = \beta E_{max} = \beta \left(\frac{2qN_d}{\varepsilon_S}\right)\left(V_b + V\right)^{1/2} \qquad (2)$$

where V_b is inbuilt potential, N_d – concentration of charge carriers in the n-area, E_{max} – maximum field strength in a homogeneous area of the spatial charge, β – coefficient considering local field changes due to the defect, ε_s – dielectric constant.

Considering (1, 2), current dependence on voltage can be expressed as follows:

$$\ln\left(\frac{I}{V}\right) = \ln a - b\left(V_b + V\right)^{-1/2} \qquad (3)$$

where [5]:

$$a = \frac{\left(2m^*\right)^{1/2} q^3 EV}{4\pi^2 \left(\frac{h}{\pi}\right)^2 E_g^{1/2}}, \qquad (4a)$$

$$b = \frac{4\left(2m^*\right)^{1/2} E_g^{3/2}}{3q\left(\frac{h}{\pi}\right)\beta\left(\frac{2qN_d}{\varepsilon_s}\right)^{\frac{1}{2}}\left(V_b + V\right)^{1/2}} \qquad (4b)$$

where m^* – effective electron mass; E_g – band gap of silicone.

Experimental data shown in fig. 3 confirm with a high degree of certainty the presence of specified dependence between current value and applied voltage at values β in expression (4b) equal to 184.6 and 211.8 for temperatures –60 °C

and 25 °C, respectively. Obtained values β according to (2) lead to electric field values in the defective region $(3.1$–$3.6)\times10^6$ V/cm at $V = 1$ V and $(0.98$–$1.15)\times10^7$ V/cm at 10 V which significantly exceeds the field strength during avalanche breakdown in silicone $(\sim5\times10^5$ V/cm) and complies with literature data for tunnel breakdown [5, 6]. An additional argument confirming the tunneling mechanism of current flow is its weak temperature dependence with a negative temperature coefficient $(dI/dT < 0)$ (fig. 1).

Using expression (4a) and experimentally obtained dependencies of tunneling current on voltage (fig. 3):

$$I/V = 0.0095\exp\left(-24.37V^{-1/2}\right) \text{ at } -60 \text{ °C}, \quad (5a)$$

$$I/V = 0.031\exp\left(-28.18V^{-1/2}\right) \text{ at } 25 \text{ °C}, \quad (5b)$$

It is possible to determine the ratio of tunneling current to its density J_t and, respectively, the area of the emitting area A_t from the ratio $A_t = I/J_t$. Obtained values $A_t = 350$–650 A indicate the presence of local current flows making up to 5×10^{-10}–2×10^{-9} of the area of the p–n junction at temperatures of -60 °C and 25 °C, respectively.

Since the distribution of PSE with "soft" characteristics over the area of plates is random, it may be caused be local defects, such as oxide or the silicone surface defects formed by phosphorus diffusion [6]. The location of defects causing tunneling currents near the surface is confirmed by the fact that in the considered range of reverse voltages the width of the spatial charge area of the p^+–n junction with high field strength does not exceed 5 microns. Penetration defects of the specified type may result in tunnel breakdown of parasitic p^+–n^+ junctions due to a high concentration of alloying admixtures, as well as formation of local defect areas on the silicate surface (fig. 4) containing impurities of oxygen, carbon [6] and heavy metals (impurity precipitates) around which the electric field strength increases.

The influence of local defects on the formation of PSE with abnormal "soft" VAC is confirmed by a correlation between the number of PSE with low density of defects on the plate $(< 5 \text{ cm}^{-2})$ detected using an optical microscope (N_{def}) and the number of PSE with low dark

currents (Npse) (fig. 5). The data are specified for 100 plates from different batches, each of which contains 70 lines of 16 PSE. Consequently, an important task is to reduce the density of oxide

defects which is achieved by the optimization of phosphorous diffusion modes and improvement of the quality of the oxide formed before diffusion [1, 4].
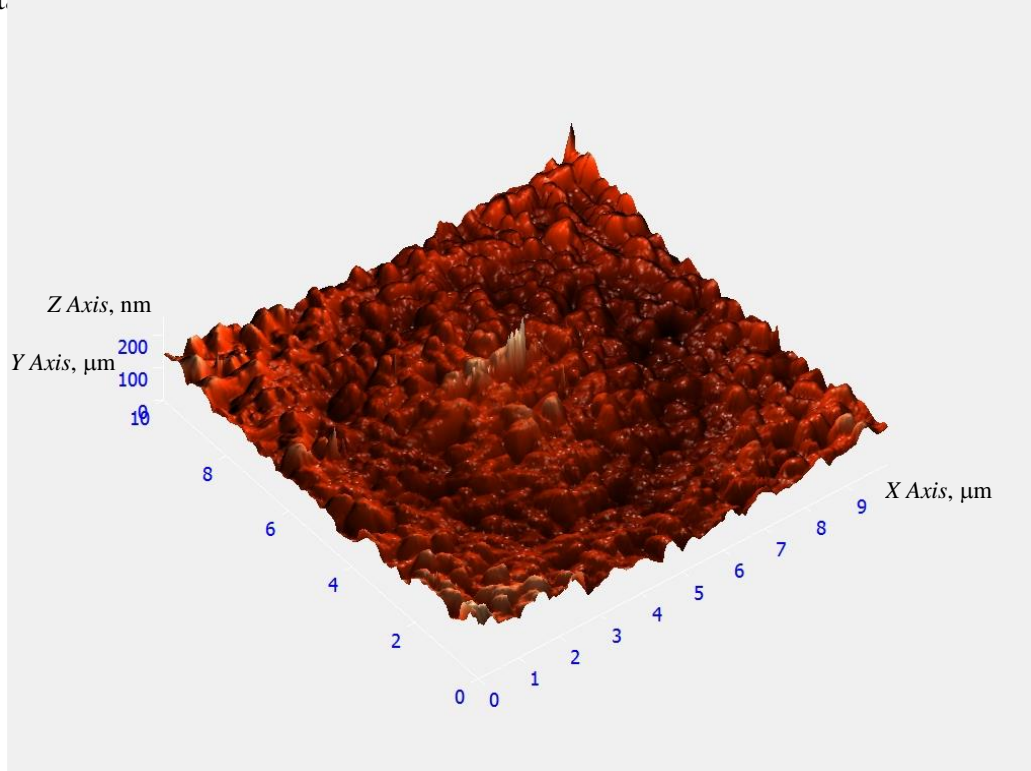
Fig. 4. Image of defect in silicone and atomic-force microscope
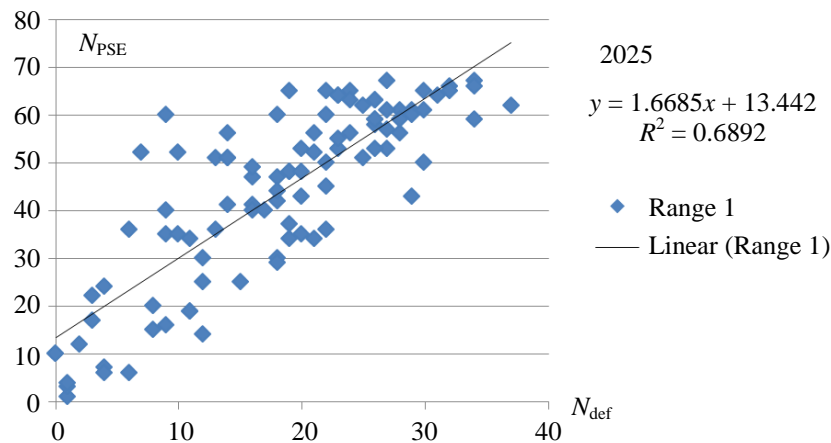
Fig. 5. Dependence of the number of PSE with $I_d < 1 \times 10^{-11}$ A at 10 mV on the number of PSE with density of defects less than 5 cm^{-2}

The formation of impurity precipitates near defects is more obvious out of two considered reasons of tunneling currents occurrence. Obviously, thermal operations following the phosphorous diffusion cannot remove the formed n^+-channel. At the same time, the selection of optimal modes of the subsequent gettering operation resulting in the removal of

contaminating impurities from silicone volume, including impurity precipitates, makes it possible to almost practically exclude the formation of PSE with abnormal characteristics.

Repeated carrying out of the impurity gettering operation on plates containing PSE with "soft" characteristics also leads to the reduction of such elements.

Conclusions

1. It is established that voltage-current characteristic (VAC) of silicone photodiodes with abnormal "soft" characteristics is determined by tunneling mechanism of current flow.

2. The cause of tunneling currents are local areas with a small area and electric field strength of 3×10^6–10^7 V/cm. The reason of occurrence of such areas can be impurity precipitates formed on the silicone surface during the formation of defects in the oxide.

3. Use of optimal modes of impurity gettering leads to sharp decrease in the number of photosensitive elements with abnormal VAC.

REFERENCES

1. Blackstone S., Henry W., Jastrzebski L. and Fisher A. W., Journal of Electrochemical Society **3**, 667–668 (1982).
2. Storch W., Mohr U., Elstner L. and Leihkauf R., Phys. Stat. Sol. (a) **132**, K109 (1992).
3. Miyashita M., Fukui H., Kubota A., Samata S., Hiratsuca H. and Matsushita Y., International Conference on Solid State Devices and Materials. Yocohama, 1991, pp. 568–570.
4. Boltar K. O., Vildyaeva M. A., Irodov N. A., Klimanov E. A., Lyalikov A. V., Malygin V. A., Molchanov D. S., Makarova E. A., Applied Physics, № 2, 39 (2025).
5. Zi S., Physics of Semiconductor Devices. Moscow, Mir, 1984.
6. Busta H. H. and Waggener H. A., Journal of Electrochemical Society **124** (9), 1424–1429 (1977).

About authors

Boltar Konstantin Olegovich, Head of Scientific and Technical Complex, Doctor of Physics and Mathematics, RD&P Center ORION, JSC (111538, Russia, Moscow. Kosinskaya st.,9). Moscow Institute of Physics and Technology (141701, Russia, Dolgoprudny, Moscow Region, 9, Institutsky lane). E-mail: boltarko@yandex.ru SPIN code 9249-2720, Author ID 171355

Vildyaeva Maria Nikolaevna, Engineer Cat. 1, RD&P Center ORION, JSC (111538, Russia, Moscow, Kosinskaya st., 9). E-mail: mari.vildyaeva@mail.ru

Demidov Stanislav Stefanovich, RD&P Center ORION, JSC (111538, Russia, Moscow Kosinskaya st., 9). SPIN code: 2028-9758, AuthorID: 780596

Klimanov Evgeniy Alekseevich, Senior Research Assistant, Professor, Doctor of Technical Sciences, RD&P Center ORION, JSC (111538, Russia, Moscow, Kosinskaya st., 9). MIREA – Russian Technological University (119454, Russia, Moscow, Vernadskogo Ave., 78). E-mail: klimanov3@mail.ru SPIN code 7697-4688, Author ID 171375

Molchanov Dmitry Sergeevich, Engineer, RD&P Center ORION, JSC (111538, Russia, Moscow. Kosinskaya st.,9).

Makarova Elina Alekseevna, Engineer Cat. 2, RD&P Center ORION, JSC (111538, Russia, Moscow, Kosinskaya st., 9).

Popov Konstantin Alekseevich, engineer RD&P Center ORION, JSC, (111538, Russia, Moscow, Kosinskaya st.,9). E-mail: kostya.popov.2001@gmail.com SPIN code: 5321-4009

Zhukovich-Gardeeva Aleksandra Aleksandrovna, Engineer Cat. 2 RD&P Center ORION, JSC (111538, Russia, Moscow, Kosinskaya st., 9).

Egorov Aleksandr Vasilevich, academic secretary, Assistant Professor, Candidate of Technical Sciences RD&P Center ORION, JSC (111538, Russia, Moscow, Kosinskaya st., 9).

On the possibility of quality control of semiconductor single crystals based on retrospective analysis of production control databases

N. Y. Komarovskiy[1,2,*], S. N. Knyazev[2], A. A. Trofimov[3], E. A. Savinykh[2],
E. A. Sokolovskaya[1], and A. V. Kudrya[1]

[1] *Sazhin Giredmet JSC, Moscow, 111524 Russia*
[*] *E-mail: nickkomarovskiy@mail.ru*
[2] *University of Science and Technology MISIS, Moscow, 119049 Russia*
[3] *RD&P Center ORION, JSC, Moscow, 111538 Russia*

A retrospective analysis of a production control database for growing tellurium-doped GaAs single crystals using the Czochralski method was conducted. The asymmetry and Smirnov criteria were used to evaluate the normal distribution of material and process parameters. The strength of the relationship between material parameters and process parameters was assessed using the gradation of the paired correlation coefficient $|r_{xy}| \in 0.013–0.420)$. A significant discrepan-

cy was observed between the actual and predicted results within the regression model (the correlation coefficient R varied in the range of 0.23–0.47). Using cognitive graphics techniques, it was shown that convective mixing of the melt with a flat crystallization front is necessary to achieve high free carrier mobility at a low density of structural defects ($N_d < 1.8 \times 10^4$ cm^{-2}).

REFERENCES

1. Mayanov E., Gasanov A., Knyazev S. and Naumov A., E`lektronika: nauka, texnologiya, biznes, № 2, 172–184 (2018). doi: 10.22184/1992-4178.2018.173.2.172.184
2. Komarovskiy N. Y., Parkhomenko Y. N., Molodtsova E. V. et al., Russ Microelectron **53**, 827–834 (2024). https://doi.org/10.1134/S1063739724701038
3. Machiev A. V., Innovative Science, № 12-2, 41–44 (2021).
4. Bosov E. V. Evaluation of the possibility of increasing the efficiency of retrospective analysis of industrial process and product control data arrays for metal product quality management tasks: dissertation abstract, MISIS, 2025.
5. Kudrya A. V. and Sokolovskaya E. A., Kachestvo i zhizn`, № 1, 27–35 (2017).
6. Nalimov V. V. Teoriya eksperimenta. Moscow, Nauka, 1971.
7. Book of semi standards 0600 – USA California – 2000 p.4837
8. Komarovskiy N. Yu. et al., Applied Physics, № 6, 54 (2023) [in Russian]. doi: 10.51368/1996-0948-2023-6-54-59
9. Chentsov N. N. Statistical decision rules and optimal inferences. Moscow, 1972.
10. Orlov A. A. and Orlov A. I., Kontrolling, № 4, 30 (2024).
11. Eddowes M. and Stansfield R. Methods of decision-making / Translated from English under the editorship of Corresponding Member of the Russian Academy of Sciences Eliseeva I. I. Moscow: Audit, UNITY, 1997.
12. Melnichenko A. S. Data Analysis in Materials Science. Part 2. Regression Analysis. Moscow, Izdatel`skij Dom MISiS, 2014.
13. Faiez R. and Asadian M., Journal of crystal rowth **311** (3), 688–694 (2009).
14. Bogdanova V. A. et al., Fizika tverdogo tela **50** (2), 236 (2008).
15. Faiez R., Najafi F. and Rezaei Y., Intern. J. of Computational Eng. Res. 2015
16. Chebanov S. V. Cognitive graphics as a way of depicting ideas // METHOD: Moscow yearbook of works from social science disciplines: Sat. of scientific works / RAS. INION. Center for advanced methodologies in social and humanit. research; ed. team: Ilyin M. V. (editor-in-chief) and others. Moscow, 2020. Iss. 10: Following Descartes. Ideal purity and material basis of thinking, cognition, and scientific methods, pp. 309–376. Access mode: http://www.doi.org/10.31249/metod/2020.10.16
17. Kudrya A. V., Sokolovskaya E. A., Trachenko V. A., and Korotneva K. V., Vector of Science TSU, № 3, 202–204 (2013).

Об авторах

Комаровский Никита Юрьевич, руководитель направления лаборатории высокотемпературных полупроводниковых соединений $A^{III}B^{V}$, АО «Гиредмет» (111524, Россия, Москва, ул. Электродная, д. 2, стр. 1). Национальный исследовательский технологический университет «МИСИС» (119049, Россия, Москва, Ленинский просп., д. 4, стр. 1). E-mail: nickkomarovskiy@mail.ru, NYKomarovsky@rosatom.ru https://orcid.org/0000-0002-7869-7886, Scopus Author ID 58510893300, Web of Science Researcher ID NRX-9045-2025, SPIN-код: 9642-8920

Князев Станислав Николаевич, к.т.н., начальник лаборатории, АО «Гиредмет» (111524, Россия, Москва, ул. Электродная, д. 2, стр. 1).

Трофимов Александр Александрович, к.т.н., заместитель начальника серийного производства, АО «НПО «Орион» (111538, Россия, Москва, ул. Косинская, 9). E-mail: aa-trofimov@yandex.ru SPIN-код: 3716-5536, AuthorID: 818356

Савиных Екатерина Александровна, студент, Национальный исследовательский технологический университет «МИСИС» (119049, Россия, Москва, Ленинский просп., д. 4, стр. 1). E-mail: swa.ekaterina@yandex.ru https://orcid.org/0009-0005-0748-7629

Соколовская Элина Александровна, к.т.н., доцент кафедры металловедения и физики прочности, Национальный исследовательский технологический университет «МИСИС» (119049, Россия, Москва, Ленинский просп., д. 4, стр. 1). E-mail: sokolovskaya@misis.ru ORCID 0000-0001-9381-9223, Web of Science Researcher ID AAM-6419-2021, Scopus Author ID 15077468100, SPIN-код: 2633-6344, AuthorID: 185426

Кудря Александр Викторович, д.т.н., профессор, заместитель заведующего кафедрой металловедения и физики прочности, Национальный исследовательский технологический университет «МИСИС» (119049, Россия, Москва, Ленинский просп., д. 4, стр. 1). E-mail: AVKudrya@misis.ru ORCID: 0000-0002-0339-2391, Web of Science Researcher ID GWZ-8579-2022, Scopus Author ID 6603628218, SPIN-код: 6497-2109, AuthorID: 11030

Conformal thermal metamaterials – new opportunities for managing heat flows in electronics

Yu. I. Sakunenko[1,*], V. S. Kondratenko[2], and A. A. Trofimov[3]

[1] *LLC "Termointerfeisy", Skolkovo Foundation, Moscow, 121205 Russia*
[2] *MIREA – Russian Technological University, Moscow, 119454 Russia*
[3] *RD&P Center ORION, JSC, Moscow, 111538 Russia*

Overheating is a fundamental barrier to the development of electronics due to the rapid increase in heat flux density (up to 200 W/cm² in processors). The paper presents the results of the development and validation of a new class of materials – Conformal Thermal Metamaterials (CTM), possessing a unique triad of properties: pronounced thermal conductivity anisotropy ($\lambda xy/\lambda z \approx 20$–$30$, where $\lambda xy = 60$–80 W/(m·K), $\lambda z = 2$–4 W/(m·K)), enabling "heat flow turning"; conformality – the ability to precisely replicate surface topography and bend up to $180°$ for geometric flow control; auto-effect of thermal contact improvement due to micro-extrusion of internal thermal paste. CTMs occupy an intermediate position (level L1+ "flexible planar routing") between rigid anisotropic plates and heat pipes, combining their advantages at a lower cost. Validation experiments on LED strips, point LED sources, and power resistors showed a reduction in crystal temperature by 28–45 °C, equivalent to a 2–3 times increase in service life. The efficiency of CTMs, comparable to aluminum radiators, has been proven, with the potential to create completely flat, radiator-free devices.

Keywords: thermal metamaterials; thermal conductivity anisotropy; conformal materials; thermal routing; LEDs.

Introduction

The issue of excess heat dissipation accompanies the development of any technology, but in electronics it is particularly critical. As the specific power increases (e.g., up 10–15 W/mm² in LED systems and up to 200 W/cm² in processors), so does the heat generation, thus leading to overheating and reduced efficiency and reliability of components. Traditional solutions, such as bulky isotropic heat sinks and thermal interfaces, have exhausted their potential as a result of facing limitations including incomplete contact, rigid geometry, and isotropic thermal conductivity. Therefore, the search for alternative materials for heat dissipation has become a major industrial priority. One promising solution is the use of synthetic diamonds grown by chemical vapor deposition from carbon plasma followed by polishing to an ideal crystalline structure. As a result, they fit to the chip surface as tightly as possible and ensure efficient heat dissipation from hotspots [1]. However, the cost of this solution remains high due to complex manufacturing processes. Hybrid solutions, such as diamond-copper heat sinks, are being developed simultaneously [2]. Considering that the leading global manufacturers adopt manufacturing of 2 nm chips and implement increasingly complex chip packages, the search for new solutions ensuring effective heat dissipation and thermal flow management has become a vital problem [3].

One of such fundamentally new approaches is the use of thermal metamaterials [4], whose properties are determined not by chemical

composition, but by a specially designed microarchitecture. Such materials feature unique properties that cannot be developed using natural substances [5] and consist of numerous elementary cells of a specific shape and size arranged in a periodic pattern [6].

This paper presents the results of the development and experimental validation of conformal thermal metamaterials (CTMM), a new class of materials that combine strong anisotropy of thermal conductivity with geometric flexibility and manufacturability.

Materials and methods

The basis of CTMM is a metal matrix frame [7, 8], which is an assembly of specially bonded micro-profiled and micro-perforated sheets of aluminum foil (see Fig. 1). This matrix is fully impregnated with a highly viscous thermal paste based on zinc oxides. The thickness of sheet samples is 1–1.5 mm.

CTMM shown in Fig. 1 feature a unique triad of characteristics that cannot be found in natural materials.

One such characteristic of CTMM thermal properties is thermal conductivity anisotropy. The developed architecture provides the anisotropy having a technical significance. The transverse thermal conductivity (λz) is 2–4 W/(m·K) (measurements were conducted in LG and Foxconn laboratories), while the longitudinal thermal conductivity (λxy) is 60–80 W/(m·K) (measurements were conducted in laboratories in Sweden and Germany). The anisotropy coefficient reaches 20–30, enabling the effective implementation of the heat flow "turn" effect and its transport within the material's plane.
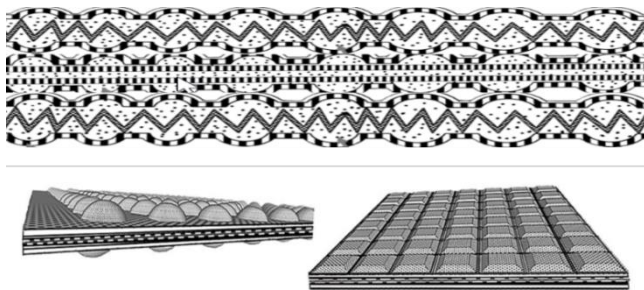
Fig. 1. Topology variants of conformal thermal metamaterials

Another key (mechanical) characteristic is the conformity and flexibility of presented CTMM. Due to the presence of numerous micro-cells and use of thin, ductile foil, CTMM is able to precisely replicate the shape of almost any contacting surface – from a rectangular chip on a printed circuit board to a cylindrical laser – even under minimum pressure. The material bends easily in any direction (up to 180°), thus offering fundamentally new prospects for the geometric management of heat flows. For example, obstacles can be bypassed by simply bending CTMM, which is infeasible for rigid graphene plates.

The third feature (technological) is automatic improving of thermal contact (autothermal contact). During mounting, the thermal paste is extruded through micro-perforations onto the surface (resulting in a "honeycomb effect"), which displaces air, the main enemy of heat transfer, and ensures practically ideal contact in combination with the matrix plasticity.

If CTMM are considered in terms of their ability to manipulate heat flows (heat collection in area A (collector), concentration, transportation, and unloading in area B (emitter), then the concept of thermal routing can be introduced to systematize the capabilities of CTMM, which allows classifying the existing solutions into the following levels:

• L0 (no routing) – isotropic materials (metals, plastics, ceramics), where the flow direction is dictated by external gradients;

• L1 (rigid planar 2D routing) – anisotropic materials (graphenes) that conduct heat in a straight line due to their rigidity;

• L2 (3D routing) – heat pipes, which effectively transfer the heat from point A to point B but are expensive and require additional bulky collectors and heat sinks.

In this classification, CTMM take an intermediate position marked as L1+ (flexible planar 2D+ routing). They not only collect and transport the heat like graphenes, but, due to their conformity and flexibility, can also easily change the trajectory and final destination of heat delivery, bypassing obstacles and adapting to the actual three-dimensional geometry of the device.

Experimental validation of CTMM thermal characteristics was conducted using LED strips, point LED modules, and high-power resistors. Temperature fields were recorded using Testo 873 thermal imager in Super Resolution mode.

Experimental section

To evaluate the effectiveness of CTMM for distributed heat sources, an experiment was conducted to cool an LED strip. The strip was mounted in a plastic profile: its one half was cooled passively, its other half – with an inserted piece of CTMM (see Fig. 2).

As can be seen from Fig. 2, the LED strip at 15 V reached the temperature of 126 °C with passive cooling and 86 °C when cooled using the inserted piece of CTMM. Thus, the temperature difference across lenses (chip temperature indicator) was approximately ~ 40 °C in favor of the section comprising CTM. Temperature reduction by 40 °C can extend the service life of LED several times or allow for a significant increase of light flux.

Steady-state junction temperatures (see Fig. 3) proved to be practically identical, thus confirming the feasibility of front-side cooling and heat flow redirection.

To compare the effectiveness of CTM with standard heat sinks, an experiment was conducted to cool high-power resistors. Several cooling schemes were applied (Fig. 4): a basic scheme using only thermal paste for cooling; a traditional scheme using a E-shaped heat sink for cooling; and a scheme using CTM, where two CTM plates formed a closed "cocoon"-like shell around the resistor.
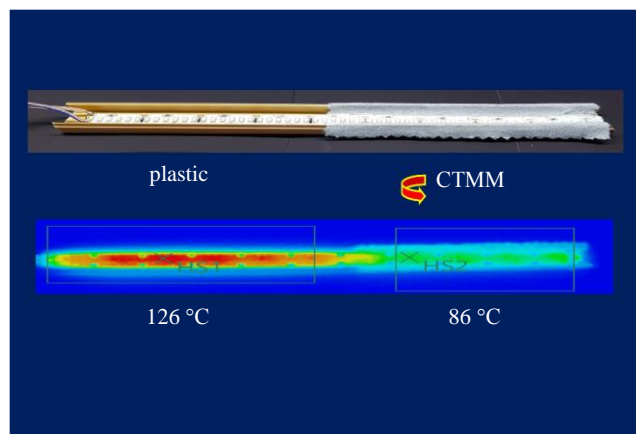
Fig. 2. Comparison of temperature fields of the LED strip in standard cooling conditions (plastic profile) and with the use of CTMM

To demonstrate the "thermal turn" effect, the ability to redirect the heat flow by 180° was shown using high-power point LEDs. One LED was cooled by a traditional E-shaped heat sink, while the other was cooled by tulip-shaped CTM that enveloped the sides and rear and redirected the heat forward (Fig. 3).
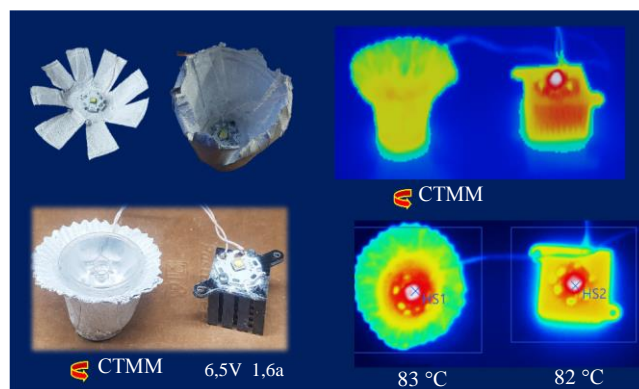
Fig. 3. Temperature comparison of high-power point LEDs under traditional (rear) cooling (U-shaped aluminum heat sink) and with the use of tulip-shaped CTMM (front cooling)

| a) | b) | c) |
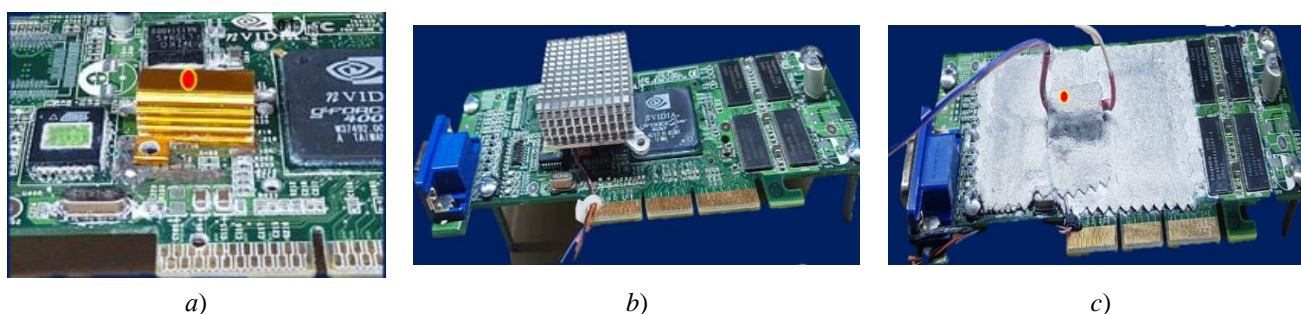
Fig. 4. Cooling schemes for the high-power resistor: a) – thermal paste only; b) – standard aluminum heat sink; c) – CTM cooling ("cocoon' configuration)

Temperature of high-power resistors vs. dissipated electrical power for all three cooling schemes is shown in Fig. 5.
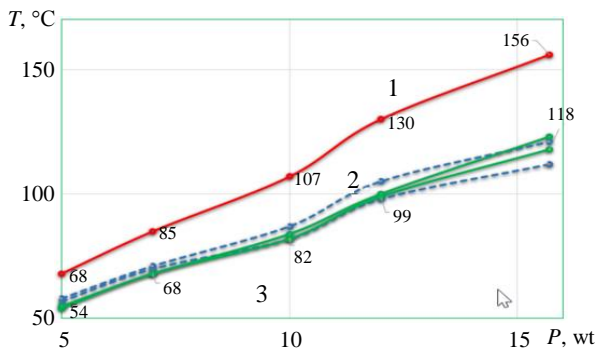
Fig. 5. Temperature of high-power resistors vs. dissipated electrical power for the cooling schemes: 1 – thermal paste only; 2 – standard aluminum heat sink; 3 – CTM ("cocoon" configuration)

As can be seen from the curve in Fig. 5, the use of CTM in the "cocoon" configuration (line 3) across the entire load range up to 16 W provided the efficiency equivalent to that of a standard aluminum heat sink (dashed line 2) and significantly outperformed the scheme with thermal paste only (line 1). Thus, the feasibility of turning a printed circuit board into an actual effective flat heat sink using CTM is confirmed.

Conclusion

The developed conformal thermal metamaterials represent a full-featured solution for controlling heat flows in modern electronics. CTM exhibit a unique triad of properties: anisotropy ($\lambda xy/\lambda z \approx 20\text{--}30$), conformability (bending up to 180°), and autothermal contact, which provides unprecedented flexibility in heat control. Temperature reduction of LED chips by 28–45 °C has been experimentally confirmed, which is equivalent to increase of service life by 2–3 times. In terms of cooling capacity, CTM are equivalent to traditional heat sinks in a number of cases, while they provide a significant reduction of device size and mass, opening the way for flat designs not comprising heat sinks. The concept of L1+ level thermal routing has been implemented to enable full manipulation of heat with CTM: heat collection, concentration, transportation, and directional dissipation, including its turn by 180°. Future applications of CTM include cooling of devices with pulsed heat generation (lasers, lidars) and using CTM for electromagnetic shielding elements of printed circuit boards.

REFERENCES

1. www.nytimes.com/2025/10/08/science/diamonds-computer-chips-ai.html
2. https://www.techpowerup.com/331456/element-six-introduces-copper-diamond-composite-material-to-enhance-cooling-of-advanced-semiconductor-devices
3. https://asia.nikkei.com/business/tech/semiconductors/applied-materials-says-chipmaking-is-entering-the-atomic-era
4. Cahill D. G., Ford W. K., Goodson K. E. et al., J. Appl. Phys. **93**, 793–818 (2003).
5. Semchenko I., Hahomov S., Samofalov A. and Balmakov A., Nauka i innovacii, № 8, 23–27 (2020) [in Russian]. https://doi.org/10.29235/1818-9857-2020-8-23-27
6. Yan Zhao et al., New J. Phys. **12**, 103045 (2010). doi:10.1088/1367-2630/12/10/103045
7. Sakunenko Yu. I. Heat removal device for heat-generating objects: Pat. RU 217975 U1 Russian Federation; filed 06.03.2023 № 2023105094 [in Russian].
8. Kondratenko V. S., Sakunenko Yu. I. and Vysokanov A. A., Applied Physics, № 1, 85–89 (2017) [in Russian].

About authors

Sakunenko Yuri Ivanovich, Candidate of Technical Sciences, General Director, LLC "Termointerfeisy" (121205, Russia, Moscow, Nobel Street 7) E-mail: teplostok.plastic@gmail.com

Kondratenko Vladimir Stepanovich, Doctor of Technical Sciences, Professor, Chief Research Assistant of the Engineering Center, Rectorate Advisor MIREA – Russian Technological University, (119454, Moscow, Vernadsky Avenue). E-mail: vsk1950@mail.ru AuthorID: 497953, Orcid ID 0000-002-2559-535X, Scopus Author ID 15834985700

Trofimov Alexander Aleksandrovich, Ph.D. of Technical Sciences, Deputy Head of mass RD&P Center ORION, JSC (111538, Russia, Moscow, Kosinskaya st., 9). E-mail: aa-trofimov@yandex.ru SPIN code: 3716-5536, AuthorID: 818356

Effect of negative corona discharge on the contamination of sunflower seeds

V. L. Bychkov[*], A. A. Logunov, D. N. Vaulin, A. P. Shvarov, A. M. Izotov,
B. A. Tarasenko and D. P. Dudarev

M. V. Lomonosov Moscow State University, Moscow, 119991 Russia
[*] *E-mail: bychvl@gmail.com*

Studies of the influence of negative corona discharge on the contamination of sunflower oilseeds have been conducted. Treatment of seeds of this crop with cold plasma corona discharge helps to reduce their infection with fungi that cause plant diseases. As the duration of exposure increases, the effectiveness of cold plasma increases. With an exposure of 180 and 240 minutes, the negative corona reduced the rust contamination of medium-sized sunflower seeds by 100 %, but was ineffective on large ones.

Introduction

To combat fungal diseases of sunflower (such as *rust – Puccinia helianthi Schwein., Phomopsis – Diaporthe helianthi (Phomopsis helianthi) Muntañola-Cvetković, Mihaljcevic & Petrov. white rot (Sclerotinia rot) – Sclerotinia sclerotiorum (Lib.) de Bary, gray rot – Botrytis cinerea Pers. ex. Fr.* and many others), seed treatment with chemicals is commonly used. Widespread use of pesticides in agriculture is known [1] to have led to environmental problems – environmental pollution and deterioration of human health. The trend toward production of healthy organic products has been growing and requires the greening and biologization of agricultural technologies. Papers [2, 3] show that plasma has a sterilizing effect on fungi, bacteria, and viruses. Its application does not harm the natural environment, humans, or animals, is more economically beneficial than the use of chemical or natural fungicides, and represents a promising direction for the greening and biologization of agricultural production.

Cold plasma treatment has been evaluated in various studies as a successful technology for surface contamination and seed germination stimulation [3, 4]. Our research has established that low-temperature plasma has a decontaminating capability, for which reason this property needs more thorough investigation to determine the optimal application parameters for greening the preparation of field crop seeds for sowing [5–8]. The effects of corona discharges on the surface of winter wheat and barley seeds were examined in our papers [6–8]. Exposure to positive and negative corona has been shown to reduce fungal disease infection in a number of cases, which indicates that use of corona discharges for grain disinfection can be promising. This paper continues those studies [6–8]. It investigates the impact of a negative corona discharge on the overall infection level of sunflower seeds. Such studies have not been conducted previously, although the need to explore methods for affecting fungi on sunflower seeds was indicated in paper [1]. The choice of a negative corona is based on experiments [6–8]

which demonstrated that fungi are eradicated by a negative corona more intensively than by a positive one.

Experimental unit

This study utilized the same setup described in papers [7, 8], which presents the schematic diagram and photographs of the setup used to study the effect of a corona discharge on fungal diseases. It consists of a cuvette filled with the substance under study and an electrical circuit. The upper electrode assembly of 19 needles (with a tip radius of 0.4 mm) was positioned 8 mm above the grain surface. The space between electrodes in the multi-electrode configuration was 11 mm. The electrodes were under the negative voltage. The cuvette was dielectric, with a metal electrode at its bottom, cylindrical, with a cuvette diameter of 90 mm, the treated area equaled to 6400 mm², and the cuvette height was 18 mm. To treat the substance in the cuvette more uniformly, an electric motor was used to mix grains in the vertical plane. The grain mass in the cuvette was 70 g in all cases. Grains in the cuvette formed approximately 12 layers. Each layer contained 98–100 grains, with a layer weight of about 6 g. A DC power supply was used; the voltage in the experiment varied within $U = 8–10$ kV, and the current varied within $I = 20–100$ µA.

Measurement results

The table presents data on the time dependence of average parameters of the negative corona discharge. The table shows that discharge parameters changed during measurements, which was due to the inconstancy of current and voltage magnitude at the discharge. At the same time, the amount of energy deposited into the grain changed by an average of 30 % for treatment durations of 3 and 4 hours.

Table

Time dependence of average parameters of the negative corona discharge

Time	1 h	2 h	3 h	4 h
Voltage, kV	8	8.7	8.7	8.6
Current, µA	6.5	8.3	9.1	5

Sunflower seeds were monitored for inspection extent according to the procedures developed by the Federal State Budgetary Institution "All-Russian Center for Plant Quarantine" FSBI "VNIIKR" and outlined in their methodological recommendations 67-2021, using the "Plant Disease Identification Guide" [9]. Seeds were placed in Petri dishes sterilized in an autoclave, with two layers of sterilized filter paper moistened with water that had been boiled for 30 minutes in a closed flask (or sterilized). Seed germination was carried out in a thermostat at a temperature of 22–23 °C. After 10 and 14 days, the infection of sunflower seeds was determined using a microscope. Tests were performed for all major fungal diseases of sunflower. It was established that the seeds were infected only with rust.

After the exposure during 180 and 240 minutes, the negative corona contributed to complete disinfection of medium-sized seeds (weight of 1000 seeds – 55.8 g) of oilseed sunflower from rust and had no effect on this disease in large seeds (weight of 1000 seeds – 79.7 g). Our experiment did not reveal any provable effect of decontamination by cold plasma on large sunflower seeds. This is most likely related to the thickness of the seed coat and the degree of seed plumpness (Seed plumpness refers to the degree of its maturity and filling, the completion of synthesis processes for the substances constituting the mature seed). In the case of small and medium-sized sunflower seeds, their seed coat is thin and smooth, whereas in the case the seed coat of large seeds is denser and ribbed.

According to the results, plasma ions and active particles generated in the corona discharge do not manage to penetrate the thickened seed coat of sunflower seeds during the treatment time. Therefore, the treatment time or, correspondingly, the setup power becomes important when the corona discharge plasma is used. When small and medium-sized sunflower seeds are treated, the discharge voltage can be increased to 20–25 kV, which would halve the grain treatment time.

Another important factor is the seed coat thickness. The use of corona discharge plasma is only effective in the case of thin seed coats. It should be noted that our experience of working with wheat and barley grain shows that the results of treatment with a negative corona are better than with a positive corona. This is primarily related to the different molecular composition of

the plasma, as in the negative corona plasma, more negative atomic oxygen ions O^- and oxygen atoms O are produced via dissociative sticking of electrons e to oxygen molecules O_2 $(e + O_2 \rightarrow O + O^-)$ [10]. These particles are converted into ozone molecules O_3 in the reactions $O^- + O_2 \rightarrow e + O_3$ и $O + O_2 + N_2 \rightarrow O_3 + N_2$ [10], which enhance the sterilizing effect of the grain surface.

Conclusion

The treatment of oilseed sunflower seeds with cold corona discharge plasma contributes to significant reduction of their infection with rust (*Puccinia helianthi Schwein*). As the exposure duration increases, the effectiveness of cold plasma application improves. After the exposures during 180 and 240 minutes, the negative corona led to complete (100%) disinfection of medium-sized sunflower seeds from the rust germ and had no decontaminating effect on large sunflower seeds. To use corona discharge for treating sunflower seeds, varieties with a thin seed coat should be selected. When considering the impact of cold plasma on potato seeds, there is no difference from treating sunflower grain and potato seeds.

REFERENCES

1. Balayan V. M. Pharmacy for plants. Moscow, Prosveshenie, 1985 [in Russian].
2. 1st International Workshop on Plasma Agriculture [Electronic resource]: www.iwopa.org
3. 2nd International Workshop on Plasma Agriculture [Electronic resource]: www.iwopa2.org
4. Los A., Ziuzina D. and Bourke P., Food Sci. **83**, 1–10 (2018). doi: 10.1111/1750-3841.14181
5. Gordeev Yu. A. Stimulation of biological processes in plant seeds by low-temperature plasma radiation. Smolensk, Smolensk State Agricultural Academy, 2008 [in Russian].
6. Bychkov V. L., Chernikov V. A., Deshko K. I., Izotov A. M., Tarasenko B. A. and Dudarev D. P., IEEE Trans. Plasma Sci. **49** (3), 1034–1040 (2021).
7. Bychkov V. L., Goriachkin P. A., Chernikov V. A. et al. Proc. Intern Conf. Atmosphere, Ionosphere, Safety. / Eds. Borchevkina O. P., Golubkov M. G., Karpov I. V., Kaliningrad, 2023, pp. 307–310.
8. Bychkov V. L., Goriachkin P. A., Chernikov V. A., Shvarov A. P., Izotov A. M. et al., Applied Physics, № 2, 15–21 (2023) [in Russian].
9. Khokhryakov K. M., Dobrozrakova T. L., Stepanov K. M. and Letova M. F., Disease determinant plants / Ed. Khokhryakov M. K., St. Petersburg-Moscow-Krasnodar, Lan, 2003 [in Russian].
10. Lunin V. V., Samoilovich V. G., Tkachenko S. N. and Tkachenko I. S. Theory and practice of obtaining and applying ozone. Moscow, Publishing House of Moscow University, 2023 [in Russian].

About authors

Bychkov Vladimir Lvovich, Dr. Sci. (Phys.-Math.), Senior Research Scientist M. V. Lomonosov Moscow State University (119991, Russia, Moscow, Leninskie Gory, 1, bd. 2). E-mail: bychvl@gmail.com; ORCID 0000-0002-5470-1297; Scopus Author ID 7102540048; WoS Researcher ID V-7141-2018. SPIN code: 2936-116; AuthorID: 18266

Logunov Alexander Aleksandrovich, Cand. Sci. (Phys.-Math.), Junior Research Scientist M. V. Lomonosov Moscow State University (119991, Russia, Moscow, Leninskie Gory, 1, bd. 2). E-mail: logunov_aa@physics.msu.ru; Scopus ID: 57214977963

Vaulin Dmitry Nikolayevich, Cand. Sci. (Phys.-Math.), Lead Engineer M. V. Lomonosov Moscow State University (119991, Russia, Moscow, Leninskie Gory, 1, bd. 2). E-mail: vaud@yandex.ru; Scopus ID: 36107282900

Shvarov Alexander Petrovich, Cand. Sci. (Biol.), Associate Professor M. V. Lomonosov Moscow State University (119991, Russia, Moscow, Leninskie Gory, 1, bd. 2). SPIN code: 5431-8919, AuthorID: 91766; Scopus ID 6505890527

Izotov Anatoly Mikhailovich, Doctor of Biological Sciences, Chief Research Assistant M. V. Lomonosov Moscow State University (119991, Russia, Moscow, Leninskie Gory, 1, bd. 2). E-mail:a.m.izotov@mail.ru; WoS ResearcherID ABA-6764-2021; Scopus AuthorID 57212196289; ORCID 0000-0003-0286-9757; SPIN code: 5193-9448; AuthorID: 799465

Tarasenko Boris Alekseyevich, Cand. Sci. (Agricult.), Associate Professor M. V. Lomonosov Moscow State University (119991, Russia, Moscow, Leninskie Gory, 1, bd. 2). E-mail: boris.tarasenko.58@mail.ru; Scopus AuthorID 57220263009; ORCID 0000-0003-2024-833X; SPIN code: 9033-9958; AuthorID: 800486

Dudarev Dmitriy Petrovich, Cand. Sci. (Agricult.), Associate Professor M. V. Lomonosov Moscow State University (119991, Russia, Moscow, Leninskie Gory, 1, bd. 2). E-mail: kdime_80@mail.ru; WoS ResearcherID ABA-6307-2021; Scopus Author ID 57214127008; ORCID 0000-0002-9800-2682; SPIN code: 8779-8810; AuthorID: 795113

PLASMA PHYSICS AND PLASMA METHODS

Features of pulsed discharge formation in pre-ionized helium

V. S. Kurbanismailov[1], G. B. Ragimkhanov[1,*], D. V. Tereshonok[2], Z. R. Khalikova[1],
S. A. Maiorov[2] and Kh. M. Abakarova[1]

[1] *Dagestan State University, Republic of Dagestan, Makhachkala, 367025 Russia*
[2] *Joint Institute for High Temperatures of Russian Academy of Sciences, Moscow, 125412 Russia*
[*] E-mail: gb-r@mail.ru

The results of an experimental study of pulsed gas discharge in helium at atmospheric pressure with ultraviolet pre-ionization of the gas in a "mesh cathode – flat anode" system are presented. The voltage on the discharge capacitor was varied in the range of 3–14 kV. It was found that the peak current value increases monotonically from several tens to ~1000 A with increasing applied voltage, demonstrating an almost linear dependence of the peak current value (I_{max}) on the applied voltage.

Introduction

The study of physical processes in pulsed gas discharges at atmospheric and higher pressures is of significant interest from both fundamental and applied perspectives, particularly for the development of efficient radiation sources in the VUV, UV, and visible ranges, as well as for pumping gas lasers. Substantial roles in the formation of such discharges are played by gas pre-ionization mechanisms, electrode system geometry, high-voltage voltage pulse parameters, and working gas medium properties.

The review by Osipov V. V. [1] outlines the current state of research in the field of physics of high-power electrical discharges capable of exciting large gas volumes. The properties and characteristics of self-sustained high-pressure discharges are described. Experimental results and physical models of their formation and contraction are examined. The lower ignition limit of a volume discharge is shown to be associated with cathode instability. The challenges in deriving a complete theory of

volume discharge are noted. One of the main reasons for discharge contraction is the development of explosive processes on the electrode surfaces, ectons, a topic addressed in the review paper by G. A. Mesyats.

The review paper by V. F. Tarasenko et al. [3] summarizes data on diffuse and volume high-pressure discharges with transverse pumping. It emphasizes that the major difference between them is due to the ignition mechanism: a volume discharge requires pre-ionization and a uniform field, while a diffuse discharge is enabled through streamer-type breakdown and runaway electrons, especially with a small electrode radius of curvature.

The series of modern studies using high-voltage pulses [3–7] have shown that the structure and dynamics of the discharge channel depend on the ionization history, field distribution, and gas pressure. It has been established that, an oscillatory current regime can develop due to parasitic circuit inductance under certain circuit and gas parameters [8–10], while the spatial structure of the discharge can change from diffuse to spark pattern.

The previous studies [11–13] provide the detailed analysis of electrical, optical, and spectral characteristics of a pulsed discharge in helium subjected to UV pre-ionization (solid cathode, mesh anode). The paper [11] analyzes the process of contraction of a volume discharge in helium at the atmospheric pressure while the initial experimental conditions are being changed. The paper [12] reveals the features of the emission spectrum of the gas under study and electrode material's spectrum under various initial conditions: specifically, in the mode of homogeneous burning of the volume discharge, in the mode of transition from the volume discharge to the spark channel, and in the mode of transition from the volume discharge to the high-current diffuse mode in the helium pulsed discharge of high pressure. The paper [13] outlines the experimental results of studying the emission spectrum of the pulsed discharge in helium vapor-gas mixtures of high pressure, where easily ionizable impurities of electrode material vapours (Fe, Al) appear due to sputtering of electrodes subjected to ion bombardment. The electrode material vapours were shown to have significant influence on the discharge and largely determine its spectral characteristics.

This paper presents the results of the experimental study of a pulsed gas discharge in helium at the atmospheric pressure subjected to ultraviolet pre-ionization of gas in a "mesh cathode – flat anode" system, and compares experimental data to the calculations of the equivalent circuit parameters.

Experimental Setup and Measurements

Figure 1 shows the schematic diagram of the setup for studying the pulsed discharge in helium. After capacitor C_0 was charged to 3–14 kV, the voltage therefrom was applied to two electrodes: a flat anode with radii $r_0 = 2$ cm and a mesh cathode, with a distance $d = 1$ cm between

them. Pre-ionization was performed with a spark discharge.

A photo of discharge glow was taken using mirrorless digital camera Sony Alpha A7 III (ILCE-7M3B). The discharge voltage and current were recorded using Tektronix TDS 2024B digital oscilloscope with 200 MHz bandwidth, low-resistance shunt R_b and ohmic voltage divider R_1, R_2.
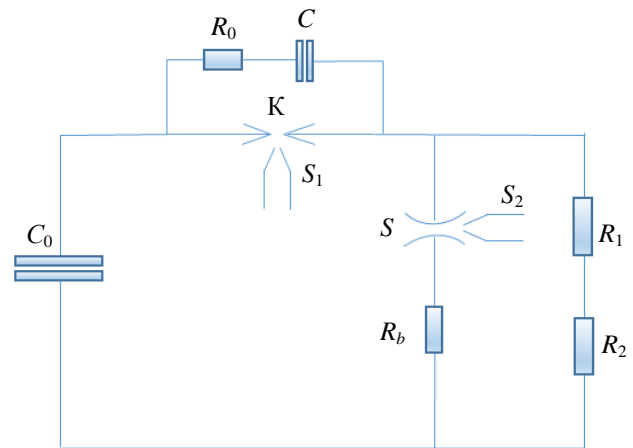
Fig. 1. Schematic diagram of the setup. C_0 – discharge capacitor, Rb – ballast resistor, K – switch, S_1 – pre-ionization source for the switch's gas medium, S – main discharge gap, S_2 – pre-ionization source for the main discharge gap ($R_0 = 300$ Ω, $R_1 = 21.3$ kΩ, $R_2 = 50$ Ω, $C = 4$ nF, $C_0 = 15$ nF)

Results of Studying the Aperiodic Discharge Characteristics

Figure 2 shows the oscillograms of the current discharge in the aperiodic current conduction mode for two values of the voltage applied. In the aperiodic mode, the current pulse shape changes depending on the voltage applied, which indicates a complex dynamics of processes in the discharge gap. At low voltage values U_0, the current pulse is bell-shaped, while at high values of the field applied, oscillations can be seen.

a)

b)
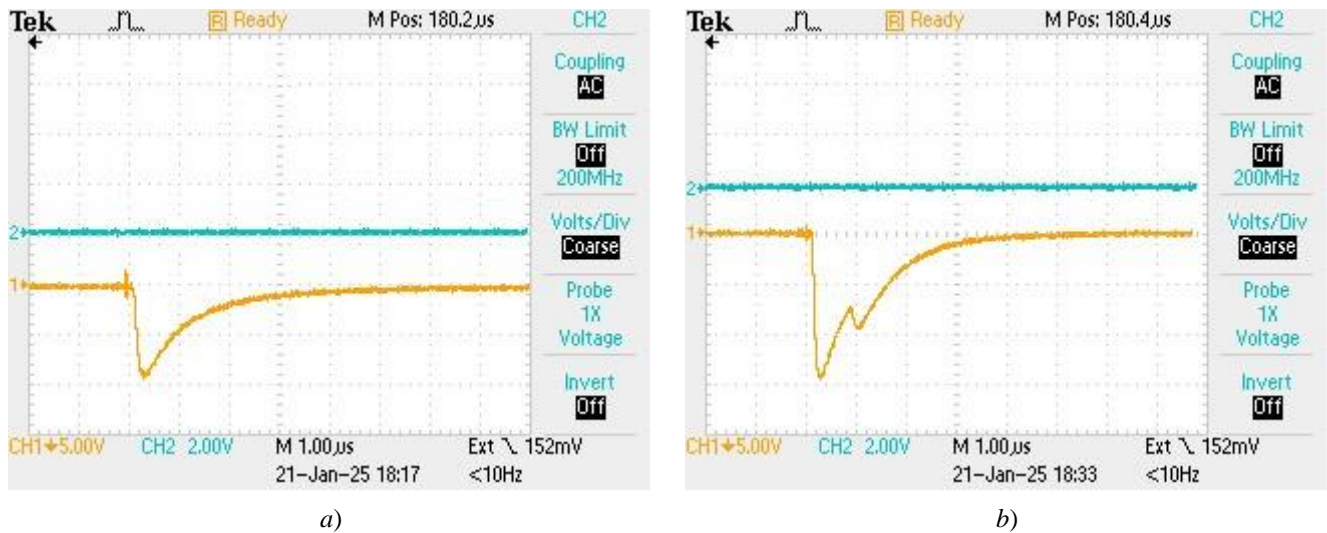
Fig. 2. Characteristic oscillograms of the discharge current in the aperiodic current conduction mode at pressure $p = 3$ atm and $R_b = 2\ \Omega$: a) – $U_0 = 8$ kV, b) – $U_0 = 11$ kV

As the gas pressure increases, the current amplitude decreases (see Fig. 3*b*) along with concurrent increase in the duration of the discharge current flow. Where a spark channel develops against the background of a volume discharge, two characteristic maxima appear on the current oscillogram (Fig. 2*b*). The first corresponds to the formation of the volume discharge, and the second – to the transition into a spark channel.

As the voltage amplitude grows from 3 to 14 kV, a linear growth in the peak current value from tens to hundreds of amperes can be seen (Fig. 3*a*, *b*). Moreover, the peak current value increases as the ballast resistance decreases.

a)

b)
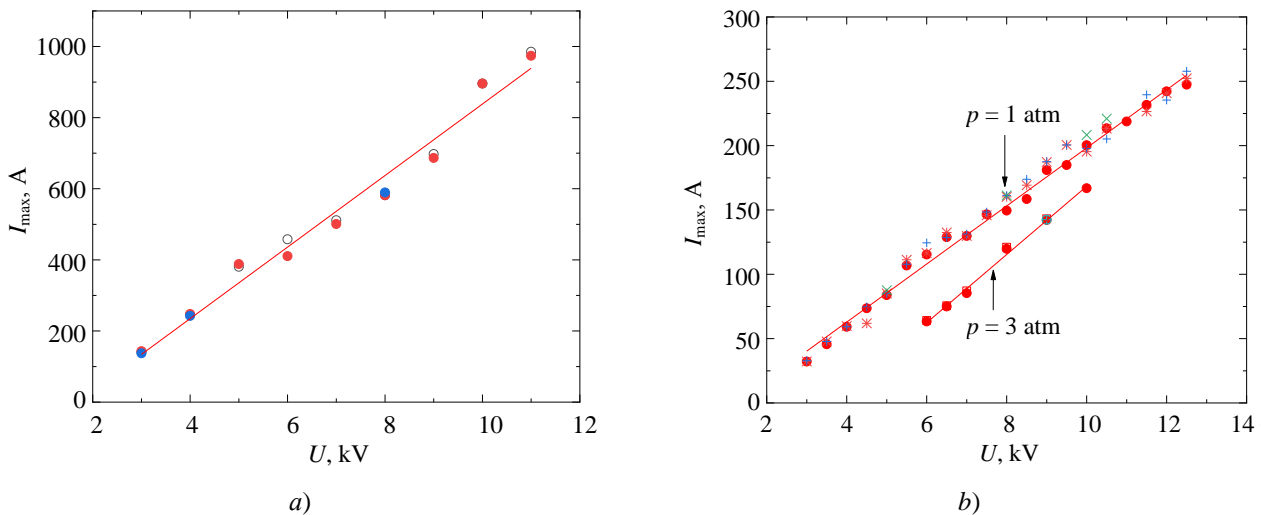
Fig. 3. Amplitude values of the discharge current in the aperiodic mode in various experiment conditions: a) $R_b = 2\ \Omega$, $p = 1$ atm, b) $R_b = 52\ \Omega$, $p = 1$ atm and 3 atm.

Figure 4 shows integral images of discharge glow in the aperiodic mode at $R_b = 2\ \Omega$. The lower electrode is mesh (cathode), the upper one is solid (anode). As can be seen, a volume discharge, which is a collection of diffuse channels attached to the cathode, is formed at the voltage of 3 kV under conditions of gas pre-ionization. As the gas pressure increases and at higher voltages, diffuse channels, that is localizations of current in the form of bright narrow channels, primarily near the mesh cathode, may appear. Starting from 7 kV, at the

atmospheric pressure, bright luminous spots develop on the anode. As voltage $U_0 \geq 8$ kV increases, the spark channels can be seen to develop, both from the cathode and anode; the channels can overlap each other, while the number of anode spots increases. The characteristic diameter of the channels, when estimated by the glow, is about 0.6–0.7 mm.

When the pressure is increased to 2 atmospheres, a significant number of current channels are observed, which are mainly concentrated in the central part of the discharge gap. At high voltages, one pronounced spark channel with a diameter of about 2 mm forms against a background of numerous diffuse channels. The spark channel is smaller in diameter at the pressure of 2 atm than at the atmospheric pressure. This effect is apparently related to the enhancement of self-contraction under conditions of increased gas density.

3 kV, 1 atm   7 kV, 1 atm   8 kV, 1 atm

10 kV, 1 atm   12 kV, 1 atm   14 kV, 1 atm

3 kV, 2 atm   7 kV, 2 atm   8 kV, 2 atm

10 kV, 2 atm   12 kV, 2 atm   14 kV, 2 atm
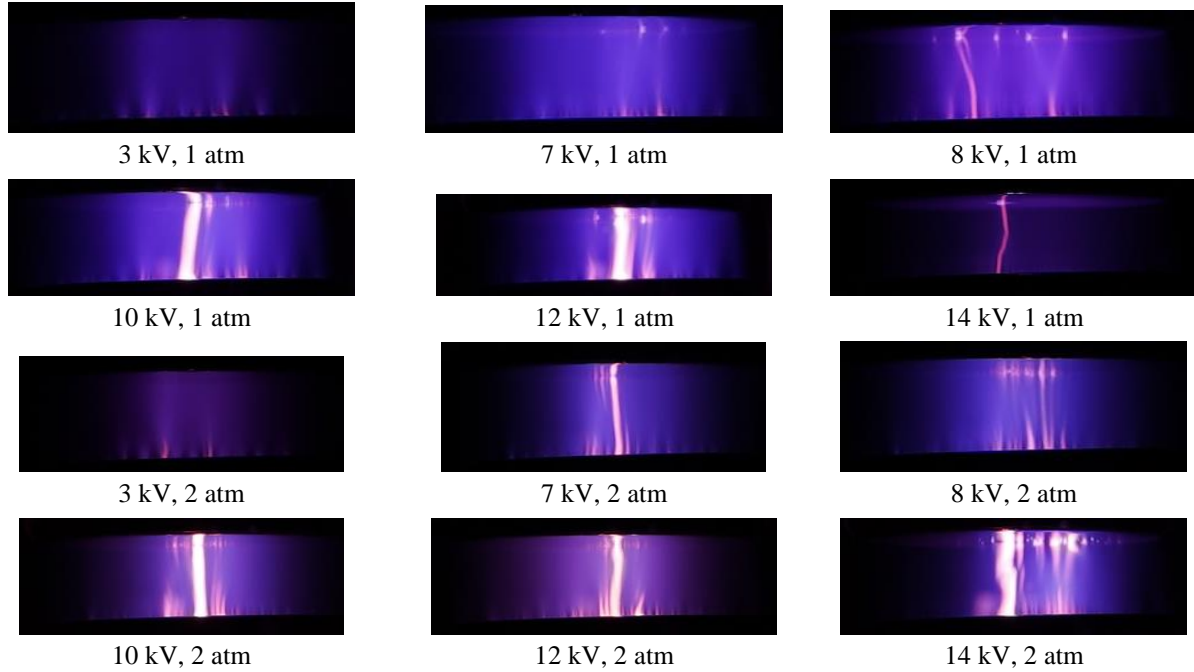
Fig. 4. Integral images of discharge glow (aperiodic mode) at $R_b = 2\ \Omega$

As it was mentioned above, minor oscillations could be observed on the oscillogram as the applied voltage increased (Fig. 5).
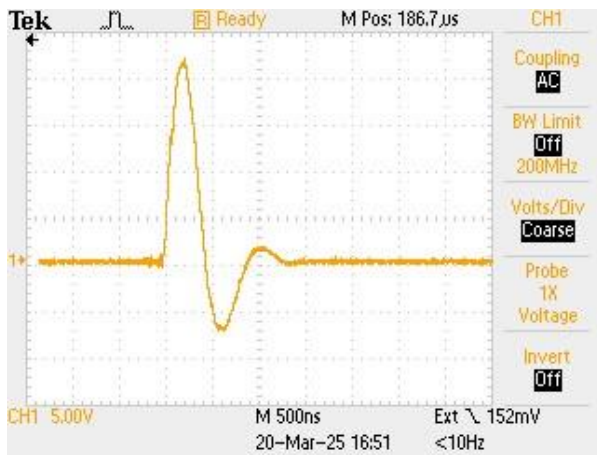
Fig. 5. Characteristic oscillograms of the discharge current: $p = 1$ atm, $U_0 = 8$ kV, $R_b = 2\ \Omega$

The presence of the oscillatory mode allows for the discharge gap to use a closed *RLC* circuit with resistance R_d, inductance L_d, and capacitance C_d, where current oscillations I are described by the expression: $I(t) = I_0 e^{-\delta t} \cos(\omega t)$, where t is time, $\omega = \sqrt{\omega_0{}^2 - \delta^2} = \dfrac{2\pi}{T}$, T is oscillation period, $I(t = 0) = I_0$ is current amplitude, $\delta = \dfrac{R_d}{2L_d}$, $\omega_0 = \dfrac{1}{\sqrt{L_d C_d}}$. Conditions of oscillatory mode presence are determined by inequation: $L_d > \dfrac{R_d^2 C_d}{4}$.

If oscillations begin after a certain distance in the switch is reached, it can be assumed that effective inductance L_d of the circuit under study

increases with the growth of the switch's interelectrode gap. This is qualitatively consistent with experimental observations. All other conditions being equal (values of R_b and U_0), the aperiodic mode transitions to the oscillatory one when the switch's interelectrode gap increases.

It should be noted that damping coefficient δ is determined by the ratio of current amplitudes with an interval equaling to one period, i.e. $\delta = \dfrac{\ln\left(I_0 / I(T)\right)}{T}$. The results in $\delta \approx \dfrac{\ln(11)}{T}$. Therefore, we get $\omega \approx \omega_0$ from definition $\omega = \sqrt{\omega_0{}^2 - \delta^2} = \dfrac{2\pi}{T}$.

In accordance with the previously calculations [11], the electron concentration in the discharge gap in the diffuse mode at the atmospheric pressure is at a level of $n_0 \sim 10^{20}$ m^{-3}, which gives the discharge gap resistance $R_d \approx (\pi r_0^2 e n_e \mu_e)^{-1} d \approx 5$ Ω, where e is electron charge, n_e, μ_e are concentration and mobility, $\mu_e \approx 0{,}1$ m^2/(s·V) at the normal gas density [14, 15].

As the effective capacitance value, we take the capacitance of the discharge capacitor $C_d = C_0 = 1.5\times10^{-8}$ F. This assumption is justified by the fact that discharge gap capacitance $C_g \sim \varepsilon_0 \pi r_0^2 / d \sim 1$ pF and plasma capacitance $C_p \sim 2\pi\varepsilon_0 d \sim 0{,}6$ pF are much smaller than C_0. Then, in accordance with the definition of δ, we find the inductance: $L_d = \dfrac{R_d T}{2\ln(11)} \approx 0.84$ μH. From graph 2*b*, we see that the oscillation period is 0.8 μs, then for the inductance we obtain $L_d = \left(\dfrac{T}{2\pi}\right)^2 / C_d \approx 1.1$ μH. The value of L_d in the equivalent circuit proved to be quite large, which is apparently due to the parasitic inductance of the setup. The plasma inductance is quite small: $L_p \sim \dfrac{\mu_0 d}{2\pi} = 2$ nH (μ_0 is the magnetic constant) compared to L_d. Meanwhile, a connecting wire with length $l = 1$ m and radius $r = 1$ mm has an inductance of $L_w \sim \dfrac{\mu_0 l}{2\pi}\ln\left(\dfrac{l}{r}\right) \approx 1.4$ μH, which is comparable to the estimates of L_d.

Thus, while the presence of parasitic inductance leads to current oscillations, it also allows obtaining a diffuse discharge in helium at the atmospheric and higher pressures with the time over 1 μs, which can be used in gas-discharge applications.

Conclusion

Thus, under conditions of gas pre-ionization in the range of 3–14 kV and ballast resistance of 2 Ω in helium at the atmospheric pressure, two discharge burning modes have been identified: oscillatory and aperiodic. It has also been found that the interelectrode distance in the switch determines the transition from the aperiodic to the oscillatory discharge burning mode. The aperiodic current conduction mode is characterized by almost linear dependence of discharge peak current I_{max} on the voltage applied, with typical current values ranging from tens to approximately ~1000 A. Increase in gas pressure from 1 to 3 atm leads to decrease in the peak current value. Optical diagnostics show that a diffuse volume discharge forms at 3 kV, while starting from 7–8 kV, localized current filaments with a diameter of 0.6–0.7 mm appear, their number increasing with voltage. However, a single bright spark channel can be observed at 14 kV.

Based on this experimental fact and analysis of the conditions for discharge current oscillations to exist, the interelectrode distance in the switch has been proposed to determine the inductance value in the equivalent RLC circuit. The effective inductance of the setup under consideration was determined based on current oscillograms.

The established patterns allow for the targeted selection of circuit parameters (capacitance, ballast resistance, length of connecting buses) to suppress oscillations in the single-pulse current mode, which is critical for pumping VUV/UV lasers and other plasma applications requiring high peak energies without subsequent dampening.

REFERENCES

1. Osipov V. V., Usp. Fiz. Nauk **170**, 225–245 (2000).
2. Mesyats G. A., Usp. Fiz. Nauk **165**, 6, 601–626 (1995).
3. Tarasenko V. F., Panchenko A. N. and Beloplotov D. V., Usp. Prikl. Fiz. (Advances in Applied Physics) **7** (6), 535–544 (2019) [in Russian].
4. Lu Y., Li W., Zhang J. et al., Plasma Sources Sci. Technol. **24** (4), 044005 (2015). doi: 10.1088/0963-0252/24/4/044005
5. Motallebi S., Sadighzadeh A., Safari S. A. et al., J. Appl. Phys. **134**, 203303 (2023). doi: 10.1063/5.0164607
6. Feng Y., Li H., Fang K. et al., Chin. Phys. B **32** (4), 045206 (2023). doi: 10.1088/1674-1056/adc670
7. Gao M., Zhu Y., Shi J. et al., J. Phys. D: Appl. Phys. **56**, 255201 (2023). doi: 10.1088/1361-6463/adcace
8. Li H., Wang Y., Chen M. et al., Plasma Sources Sci. Technol. **33**, 015001 (2024). doi: 10.1088/1361-6595/ad8308
9. Xie H., Yu H., Li Y. et al., Plasma Res. Express **6**, 015009 (2024). doi: 10.1088/2058-6272/ad5ca0
10. Lu Y., Zhang J., Li W. et al., Plasma Sources Sci. Technol. **29**, 015012 (2020). doi: 10.1088/1361-6595/ab6da6
11. Kurbanysmailov V. S. and Omarov O. A., High Temperature. **33** (3), 346–350 (1995).
12. Kurbanysmailov V. S., Omarov O. A., Ragimkhanov G. B. et al., Usp. Prikl. Fiz. (Advances in Applied Physics) **2** (3), 234 (2014) [in Russian].
13. Kurbanysmailov V. S., Omarov O. A., Ashurbekov N. A., Ragimkhanov G. B. and Gadzhiev M. Kh., Applied Physics, № 3, 41–46 (2004) [in Russian].
14. Maiorov S. A., Golyatina R. I., Kodanova S. K. and Ramazanov T. S., Plasma Phys. Rep. **50** (8), 1029–1041 (2024).
15. Maiorov S. A. and Golyatina R. I., High Temperature **43** (3), 326–332 (2025).

About authors

Kurbanismailov Vali Suleimanovich, Professor, Doctor of Physical and Mathematical Sciences Dagestan State University, (367025, Russia, Republic of Dagestan, Makhachkala, M. Gadzhiev st., 43a) E-mail: vali_60@mail.ru SPIN code: 3774-5509, AuthorID: 124135

Ragimkhanov Gadzhimirza Balaglanovich, Candidate of Physical and Mathematical Sciences, Associate Professor Dagestan State University, (367025, Russia, Republic of Dagestan, Makhachkala, M. Gadzhiev st., 43a) E-mail: gb-r@mail.ru SPIN code: 8156-8736, AuthorID: 417790

Tereshonok Dmitry Viktorovich, Candidate of Physical and Mathematical Sciences, Leading Research Scientist Joint Institute for High Temperatures of Russian Academy of Sciences (125412, Russia, Moscow, Izhorskaya st., 13, bldg. 2) SPIN code: 3790-9092, AuthorID: 601492

Khalikova Zaira Rasulovna, Dagestan State University, (367025, Russia, Republic of Dagestan, Makhachkala, M. Gadzhiev st., 43a). SPIN code: 3112-0424, AuthorID: 1031654

Maiorov Sergey Alekseevich, Doctor of Physical and Mathematical Sciences, Leading Research Scientist, Joint Institute for High Temperatures of Russian Academy of Sciences (Russia, 125412, Moscow, Izhorskaya st., 13, bldg. 2) E-mail: mayorov_sa@mail.ru SPIN code: 9331-1751, AuthorID: 24761

Abakarova Khalimat Magomelovna, Head of Office, Dagestan State University, т (367025, Russia, Republic of Dagestan, Makhachkala, M. Gadzhiev st., 43a) E-mail: abakarova2412@mail.ru

Guided discharge in water with the aid of NaCl crystals

V. A. Panov[*], A. S. Saveliev and Yu. M. Kulikov

Joint Institute for High Temperatures of Russian Academy of Sciences, Moscow 125412 Russia
[*] *E-mail: panovvladislav@gmail.com*

For the first time, the possibility of controlling the direction of propagation of an electric discharge channel in water by creating local zones of increased conductivity that arise in the "trace" of a table salt crystal moving in water has been demonstrated. A directed discharge was obtained in water with an electrical conductivity of 350 μS/cm under the action of a millisecond-duration pulse voltage with an amplitude of 7 kV in an 8 mm interelectrode gap. The effect consists in the discharge channel changing its direction of propagation when it encounters the "trace" of a sinking crystal, i.e. normal horizontal (relative to the direction of gravity) propagation from the anode to the cathode is replaced by directed vertical propagation along the "trace" with increased conductivity due to the gradual dissolution of the crystal.

Introduction

A directed electrical discharge occurs in cases where the medium through which it propagates features a spatial non-uniformity of electrical strength associated with local additional charge carriers. Such non-uniformities can exist in the medium in a stationary state or be created for a certain period immediately before the electrical discharge channel propagates.

An example of such stationary non-uniformity in electrical conductivity can be vertical stratification of soil composition, which determines the mode and efficiency of grounding system operation [1], amplitudes of electric and magnetic fields generated by a lightning discharge [2], as well as transient voltage [3] and current characteristics [4].

Either quasi-stationary or short-term non-uniformities (of density, conductivity) can occur in gases due to strong diffusion compared to solids. Examples of such non-uniformities include shock waves and rarefaction waves, where changes in density act as a kind of "gas-dynamic diode" for streamers [5]. For some types of discharges, a time-constant spatial distribution of density can be obtained using acoustic pressure fields [6], which leads to the possibility of stationary control over the position and shape of the discharge channel. However, the authors of paper [6] note that the channel's path cannot be influenced for other types of discharges due to the effects caused by temperature (density) gradients prevailing over acoustic pressure. An example of a short-term impact is laser pulsed heating of the gas in the interelectrode gap along the beam path, along which an electrical discharge propagates after that [7]. The guiding action in this case is associated with decrease in density and increase in the mean free path in the gas after laser heating. If the energy density exceeds a certain value, optical breakdown is possible in the form of individual plasma initiation sites along the radiation path [8]. Active lightning protection systems based on these phenomena are being developed [9].

Directed electrical discharge in water plays a significant role in electrohydraulic technology

for processing various materials through pulsed high-pressure impact and electrochemical effects [10]. Its essence lies in conversion of electrical energy into mechanical energy via rapid energy release in a thin discharge channel, followed by fluid motion and formation of shock waves. The efficiency of this conversion depends on many parameters – current pulse amplitude, distance between electrodes, duration and steepness of pulse fronts, shock capacitance magnitude, and others. However, the primary and most significant factor is the need to obtain long (and ultra-long) discharge channels, which is quite difficult due to the ionic conductivity of water. To solve this problem, the author [10] proposed a method of electrical (thermal) explosion of a conductor, typically a wire, which was initially connected to the electrodes and determined the direction of the future discharge channel when a high-density current was passed through it. The same author proposed an alternative method of directed radiative (including laser) exposure, where the current propagates along a channel with lower density, which occurred as a result of radiation propagating through the fluid.

As a new method for creating a region of preferential discharge channel development in water in the form of a local zone of increased conductivity, the motion of a salt crystal within the interelectrode gap is considered. The method essentially consists in gradual dissolution of the crystal as it moves and a trail is formed behind it with a locally increased concentration of salt ions (i.e., with increased electrical conductivity). This approach, on one hand, does not require mechanical repositioning of a wire, as in the case of its electrical explosion, and on the other hand, does not require additional equipment, as in the case of breakdown guided by laser radiation. Using salt also prevents of contamination of electrodes, which occurs when parts of the exploded metal conductor are welded onto them. An additional advantage is the relatively long lifetime of the trail as compared to the discharge duration, which makes it easier to synchronize introduction of the crystal into the discharge gap and apply the voltage pulse.

The aim of this paper is to obtain a directed discharge in conductive water under the influence of a millisecond-duration pulsed voltage using common salt crystals.

Experimental Setup and Methods

The study uses the setup described in paper [11] and modified according to the purpose of the study. Distilled water was poured into a transparent acrylic container (1 in Fig. 1). Below the water level, electrodes were placed – a pointed high-voltage electrode (2) and a cylindrical electrode (3) made of a tungsten rod, which were positioned 8 mm apart from each other. The lateral surfaces of the electrodes were insulated from the water, except for the working ends. The water level in the container was such that it completely covered the electrodes, while the distance from the water surface to the surface of the high-voltage electrode was about 1 cm. This relatively small distance allows common salt crystals to reach the interelectrode gap at a constant speed, as their diameter changes insignificantly during dissolution. As the visualization results suggest, this ensures the formation of a trail of practically constant diameter. The crystal falling through the water leaves a thin trail in the form of an extended region of increased conductivity due to the partial dissolution of the salt (see Fig. 1) as a dashed line near electrode 2.

To visualize the process of high-conductivity trail formation, an optical scheme based on the shadowgraph method is used, which is sensitive to local changes in fluid density due to the partial dissolution of the crystal. Luminescent LED 4 and converging lens 5 create a parallel light beam illuminating the area near the high-voltage electrode. High-speed digital video camera 6 equipped with long-focus lens 7 continuously records the shadow pattern near the tip of electrode 2 with a spatial resolution of 95 μm/pixel. The video camera records the process into memory and, when started, sends a synchronization pulse to the trigger inputs of pulse generator 8 ("TRIG") and oscilloscope ("Ext/10"). After that generator 8 produces a trigger pulse for high-voltage switch 10, with a duration of about 1 ms. Switch 10, without delay (rise time ~0.1 μs), switches the high voltage from battery C charged through ballast resistor R_b (1 MΩ) by high-voltage source 11 up to 7 kV, via limiting resistor R_l (5 kΩ) to the high-voltage electrode.

To correlate the frame number of the cinegram with the moment of high-voltage

application, the F_SYNC signal from the video camera corresponding to the start of exposure for each frame is sent to channel 1 of oscilloscope 9, and the signal from generator 8 is sent to channel 2. Additionally, the signal from high-voltage divider 12 (1:1000) connected to high-voltage electrode 2, is sent to channel 3 of the oscilloscope, and the voltage from current shunt R_s for measuring the circuit current is sent to channel 4.

Results and Discussion

Figure 2 shows photographs of the discharge gap at various moments after applying the voltage from capacitor C charged to 12 kV. The charging voltage was chosen so that, the gap would not short-circuit to plasma channel during discharge in the absence of salt trails. The state of the gap at the moment of voltage application is shown in frame #0. Trajectories of a group of moving crystals can be seen near the anode tip as bright filaments with dark edges, along with two crystals found closer to the cathode and appearing as dark dots with a diameter of about 0.4 mm, which remain practically stationary during the 1 ms pulse duration. The discharge development begins at the anode tip, where within the first 80 µs, water is heated, and a vapour-gas region stretching toward the cathode is formed (90 µs, #2). As soon as it reaches the nearest trail, the plasma of the discharge channel begins to glow more intensely, and its shape becomes T-shaped. From this moment on, the channel changes its direction of propagation and moves vertically along the crystal's trajectory, simultaneously upward and downward. The symmetry of the channel's propagation is indicative of medium's similar parameters, including conductivity within the trail, both along and against the crystal's motion direction. The channel growth rate was calculated between frames #3 and #4 and equaled to at least 7 m/s, which is characteristic of the thermal breakdown mechanism in conductive water [12]. Further development of the vapour-gas region, where channel (#5–#7) is located, occurs due to increase of its diameter with only minor elongation. Its structure maintains symmetry relative to the horizontal plane passing through the electrode axis. Simultaneously, the initial vapour-gas region, whose shape is close to

spherical, develops. A characteristic feature of the structure is the conical shape of the channel vertices with an angle of about 60°. At later stages of breakdown development, a second plasma region is initiated from the catode. It is associated solely with thermal processes near the surface without salt crystals being involved. By the end of the voltage pulse, the vapour-gas region and the discharge channel at the anode lose their initial structure and exist as a unified region.
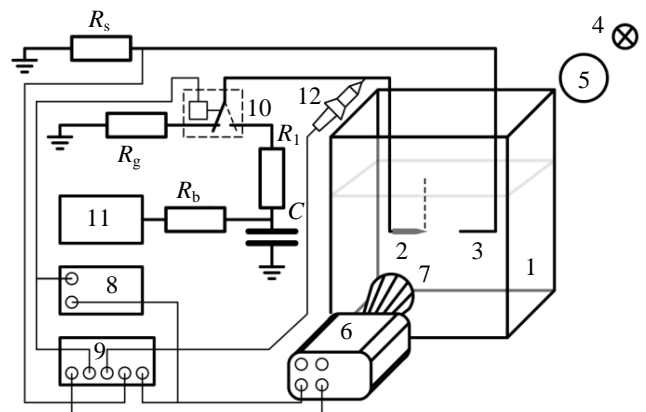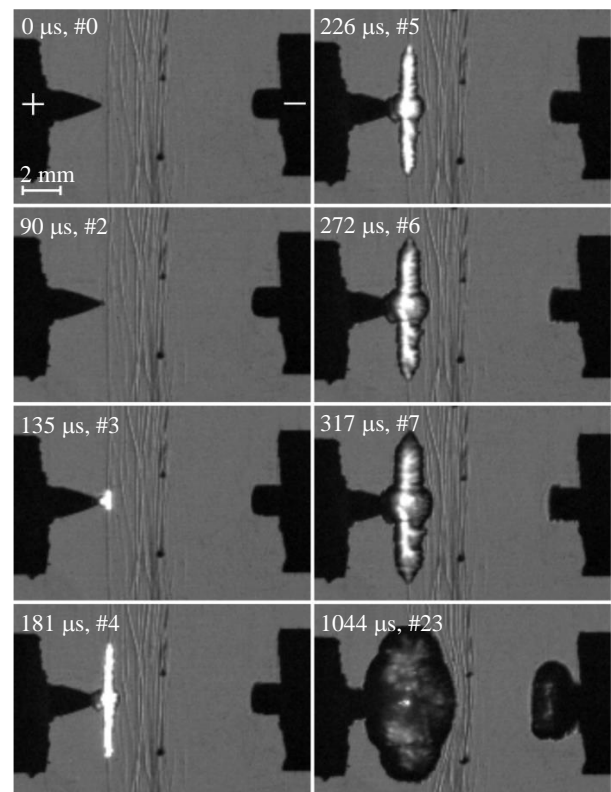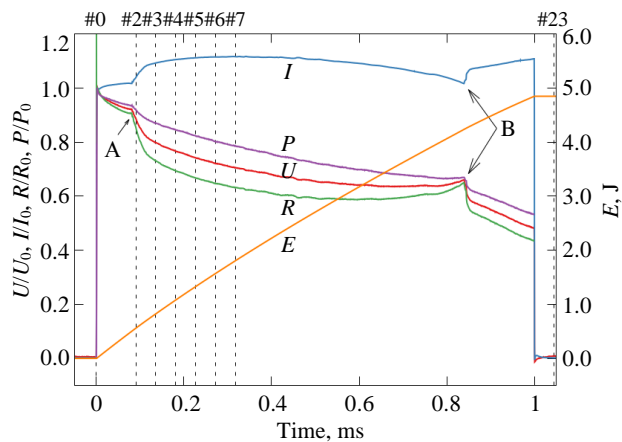

Fig. 1. Experimental setup diagram

Fig. 2. Photos of the discharge gap during development of electric discharge in water guided by the trace from the sinking sodium chloride crystal. Exposure time 0.9 µs

Fig. 3. Oscillograms of values normalized to their initial values (t = 0): voltage (U), current (I), resistance (R), power (P), and absolute value of dissipated energy (E) across the discharge gap during propagation of the directed discharge in water. [U₀, I₀, R₀, P₀]=[5.1 kV, 1.3 A, 3.9 kΩ, 6.6 kW]. Dashed lines indicate the exposure moments of frames with corresponding numbers shown above the lines. Point A (80 µs) is the beginning of plasma formation at the anode tip; Point B (840 µs) is the beginning of plasma formation at the cathode.

The oscillograms of voltage, current, resistance, and dissipated power exhibit characteristic segments reflecting the phenomena observed in the photos. In the segment from 0 µs to point A (Fig. 3), 80 µs, water is heated near the anode tip and a vapour-gas region is formed. At point A, plasma formation begins within the formed vapour-gas region. This is accompanied by current increase due to the growing conductivity within this region and overall contact area with the surrounding liquid. The main current growth and decrease in the overall gap resistance occur at the stage of channel propagation along the crystal's trajectory: additional 20% drop of resistance from the initial value takes place between 90 and 135 µs. After the discharge ignites at point A, the power required to sustain it decreases, and the overall gap resistance continues to fall. However, this trend reverses into resistance increase as it approaches point B (840 µs). This is most likely associated with the growth of the vapour-gas bubble near the cathode, which reduces the effective contact area of the cathode with water and impedes current flow until plasma occurs. After breakdown occurs within this bubble, the gap resistance drops sharply within a few microseconds and continues to decrease until the voltage application ends. The dissipated energy was increasing almost linearly during pulse duration. The total energy amounted to approximately 5 J.

Conclusions

The possibility of controlling the propagation direction of the electrical discharge channel in water has been demonstrated for the first time by creating local zones of increased conductivity that form in the trail of a common salt crystal moving in water. A directed discharge was obtained in water with the electrical conductivity of 350 µS/cm under the influence of a millisecond-duration pulsed voltage with the amplitude of 7 kV across the 8 mm interelectrode gap. The effect is expressed by the discharge channel changing its propagation direction upon encountering the trail of a sinking crystal, that is, the normal horizontal propagation from the anode to the cathode is changed by directed vertical propagation along the trajectory with increased conductivity resulting from gradual dissolution of the crystal. In this case, the discharge develops via a thermal mechanism characteristic of conductive water under relatively low voltages and long pulse durations. Analysis of the current and voltage oscillograms indicates a significant reduction in resistance between the electrodes at the moment when the discharge channel begins to propagate along the trail. The power dissipated in the discharge gap and the voltage drop across it also decrease at this moment, while the discharge current, conversely, increases. The time-dependence of the energy dissipated in the water grows linearly.

REFERENCES

1. Vasilyak L. M., Pecherkin V. Y., Vetchinin S. P., Panov V. A., Son E. E., Efimov B. V., Danilin A. N., Kolobov V. V., Selivanov V. N. and Ivonin V. V., Journal of Physics D: Applied Physics **48** (28), 285201 (2015).
2. Delfino F., Procopio R., Rossi M., Shoory A. and Rachidi F. Proc. 2010 IEEE International Symposium on Electromagnetic Compatibility. Fort Lauderdale, FL, USA, 2010, pp. 45–50.
3. Anderson R. J. de Araújo, L. M. de Azevedo W., Pissolato Filho J., S. L. Colqui J. and Kurokawa S. Proc. Anais do Congresso Brasileiro de Automática. Brasil, 2020. 10.48011/asba.v2i1.1182.

4. de Azevedo W. L. M., da Silva W. C., D'Annibale J. L. A., de Araújo A. R. J., Colqui J. S. L. and Filho J. P., Procedings do XVI Simpósio Brasileiro de Automação Inteligente / X Simpósio Brasileiro de Sistemas Elétricos. Brasil, 2023. 10.20906/sbai-sbse-2023/3980.

5. Starikovskiy A. Y. and Aleksandrov N. L., Plasma Sources Science and Technology **28** (9), 095022 (2019).

6. Irisarri J., Ezcurdia I., Iriarte N., Sirkka M., Nikolaev D., Mäkinen J., Martinez-Marchese A., Iablonskyi D., Salmi A. and Marzo A., Science Advances **11** (6), (2025).

7. Aihara Y., Shindo T., Miki M. and Suzuki T., Electrical Engineering in Japan **113** (4), 66–77 (1993).

8. Vasilyak L., Kostyuchenko S., Kudryavtsev N. and Filyugin I., Uspekhi Fizicheskih Nauk **164** (3), 263 (1994).

9. Ball L. M., Applied Optics **13** (10), 2292 (1974).

10. Yutkin L. A. Elektrogidravlicheskij effekt i ego primenenie v promyshlennosti. L.: Mashinostroenie, 1986 [in Russian].

11. Panov V. A., Pecherkin V. Ya., Vasilyak L. M., Kulikov Yu. M., Saveliev A. S. and Filatkin A. A., Applied Physics, No. 6, 29–34 (2022) [in Russian].

12. Panov V. A., Vasilyak L. M., Vetchinin S. P., Pecherkin V. Y. and Son E. E., Journal of Physics D: Applied Physics **49** (38), 385202 (2016).

About authors

Panov Vladislav Aleksandrovich, Candidate of Physical and Mathematical Sciences, senior research scientist, Joint Institute for High Temperatures of Russian Academy of Sciences (125412, Russia, Moscow, 13, Izhorskaya st., bldg. 2). E-mail: panovvladislav@gmail.com SPIN code: 5821-2776, AuthorID: 755538

Saveliev Andrey Sergeevich, Candidate of Physical and Mathematical Sciences, senior research scientist, Joint Institute for High Temperatures of Russian Academy of Sciences (125412, Russia, Moscow, 13, Izhorskaya st., bldg. 2). E-mail: fisteh@mail.ru SPIN code: 6888-7369, AuthorID: 866343

Kulikov Yuri Matveevich , Candidate of Physical and Mathematical Sciences, senior research scientist Joint Institute for High Temperatures of Russian Academy of Sciences (125412, Russia, Moscow, 13, Izhorskaya st., bldg. 2). E-mail: kulikov-yurii@yandex.ru SPIN code: 7719-8459, AuthorID: 1130937

========= PLASMA PHYSICS AND PLASMA METHODS =========

On the mean square displacement of an active Brownian particle with rotational inertia in a harmonic trap

E. A. Lisin[1,2,*] and I. I. Lisina[1,2]

[1] *Joint Institute for High Temperatures, Russian Academy of Sciences, Moscow, 125412 Russia*
* E-mail: eaLisin@yandex.ru
[2] *Moscow Institute of Physics and Technology, Moscow Region, Dolgoprudny, 141701 Russia*

One of the unsolved problems in the physics of active matter is providing an analytical description of the mean square displacement of an active Brownian particle in a harmonic trap that takes into account the particle's translational and rotational inertia. Solving this problem is relevant because inertial effects can play a significant role in a number of experiments and applications involving active particles. Within the framework of an active Brownian particle model with translational and rotational inertia, an analytical expression describing the evolution of the mean square displacement of a particle in a harmonic trap has been obtained.

Keywords: active matter; active Brownian particles; mean square displacement.

Introduction

Active matter is a special form of "soft" condensed matter, which represents a dispersion medium containing finely dispersed active particles. Despite their simplicity and lack of moving parts, such particles (also called nano- and micromotors) can autonomously convert environmental energy into directed motion [1–3]. Systems of such particles are of great interest for statistical mechanics and materials science and have numerous promising applications, from purely technical to biomedical ones. Synthetic active particles are ideal building blocks for the dynamic self-assembly of new-generation functional microstructures capable of performing specific tasks autonomously and in a targeted manner. Colloidal active matter is promising in the context of developing new materials with a "programmable" response. Applications related to biochemical analysis, substance separation, collective cargo delivery, and energy utilization from chaotic motion are also being developed [1, 2].

One of the unresolved fundamental problems in active matter physics is the analytical description of the mean square displacement, MSD(t), of an active Brownian particle in a harmonic potential, taking into account both the translational and rotational inertia of the particle. Solving this problem is of high relevance due to numerous experiments with active particles where inertial effects can play a significant role [4–9]. At present, the problem has been solved only for a number of specific (limiting) cases, namely: MSD(t) of an inertia-free active Brownian particle in a trap [10–15]; MSD(t) of an active Ornstein-Uhlenbeck particle with translational inertia in a trap [16, 17]; MSD(t) of a free, fully inertial active Brownian particle (with both translational and rotational inertia) [18, 19]; and MSD(at $t = \infty$) of a fully inertial active Brownian particle in a trap [20].

This paper is the first to derive an exact analytical expression describing the evolution of the mean square displacement, MSD(t), of a fully inertial active Brownian particle in a harmonic trap.

Basic Equations

Within the model of an active Brownian

particle with translational and rotational inertia, the two-dimensional motion of a spherical particle (with mass M and moment of inertia J) in a harmonic trap (characterized by frequency ω_0) projected onto an arbitrary X-axis is described by the following equations [18–20]:

$$M\ddot{x}(t) = -\nu_t M\dot{x}(t) + F_A \cos(\phi(t)) - \\ -M\omega_0^2 x(t) + F_B^{(x)}, \tag{1}$$

$$\ddot{\phi}(t) = -\nu_r\left(\dot{\phi}(t) + \sqrt{2D_r}\,\zeta_r(t)\right), \tag{2}$$

where ν_t and ν_r are damping coefficients for the translational and rotational motion of the particle in a viscous medium; F_A is active (propulsive) force, whose direction is determined by orientational angle $\phi(t)$ measured from X axis; $F_B^{(x)}$ is x component of the Brownian force ("translational" noise); $D_r = T/(\nu_r J)$ is rotational diffusion coefficient (here, T is the medium temperature expressed in energy units); and ζ_r is Gaussian white noise with zero mean and unit variance.

In the stationary state, the time-dependent mean square displacement of the particle along X axis is defined as

$$\mathrm{MSD}(t) \equiv \left\langle [x(t) - x(0)]^2 \right\rangle = \\ = 2\langle x^2 \rangle - 2\langle x(t)x(0) \rangle, \tag{3}$$

where $\langle x(t)x(0) \rangle$ is auto-correlation function of the particle position. Note that $\mathrm{MSD}(\infty) = 2\langle x^2 \rangle$. Since the "translational" and "rotational" noises do not correlate, $\mathrm{MSD}(t)$ can be written as the sum of two terms: the first term is the well-known Uhlenbeck–Ornstein formula for a passive Brownian particle [21], and the second term is the result of the contribution from the active (propulsive) force. Here, we intentionally disable the translational noise (setting $F_B = 0$) to focus on studying the contribution of the active force.

According to the Khinchin–Kolmogorov theorem, the autocorrelation function of the particle position can be written as

$$\langle x(t)x(0) \rangle = \frac{1}{2\pi}\int_{-\infty}^{+\infty} e^{-i\omega t} H^2(\omega) S(\omega)\, d\omega, \tag{4}$$

where $H(\omega) = (F_A/M)/(\omega_0^2 - \omega^2 + i\nu_t\omega)$ is transfer function, and $S(\omega)$ is power spectral density of the process $\cos(\phi(t))$. For a stationary process, the power spectral density is written as the Fourier transform of the autocorrelation function:

$$S(\omega) = 2\int_0^{\infty} \cos(\omega t)\langle \cos(\phi(t))\,\cos(\phi(0))\rangle\, dt, \tag{5}$$

where the autocorrelation function looks as follows [19, 20]

$$\langle \cos(\phi(t))\,\cos(\phi(t))\rangle = \\ = \frac{1}{2}\exp\left[-\frac{D_r}{\nu_r}\left(\nu_r t - 1 + e^{-\nu_r t}\right)\right]. \tag{6}$$

Results and Discussion

Integrating equation (5) after expanding the autocorrelation function (6) into a series allows deriving the power spectral density of the process $\cos(\phi(t))$ in the stationary state:

$$S(\omega) = e^{D_r/\nu_r}\sum_{m=0}^{\infty}\frac{(-D_r/\nu_r)^m}{m!}\frac{D_r + m\nu_r}{(D_r + m\nu_r)^2 + \omega^2}. \tag{7}$$

Substituting transfer function $H(\omega)$ and expression (7) into equation (4), and applying the residue theorem, we obtained the following formulas.

For non-oscillatory particle motion in the trap ($\omega_0/\nu_t < 1/2$),

$$\langle x(t)x(0) \rangle = \frac{V_0^2 \alpha e^{\xi}}{8\omega_0^2} \times \\ \times \left\{\begin{array}{l} e^{-\frac{\nu_t t}{2}}\left[C_+ G_1 e^{\tilde{\Omega}t} + C_- G_2 e^{-\tilde{\Omega}t}\right] + \\ + e^{-D_r t}\left[C_+ F_1(t) + C_- F_2(t)\right] \end{array}\right\}, \tag{8a}$$

where $V_0 = F_A/M\nu_t$ is the self-propulsion velocity of the particle, which is calculated from the formal balance of active and dissipative forces in the absence of translational and rotational noises; $\alpha = \nu_t/\nu_r$, $\xi = D_r/\nu_r$, $C_+ = 1 + 0{,}5\nu_t/\tilde{\Omega}$,

$C_- = 1 - 0{,}5 \nu_t / \tilde{\Omega}$, $\qquad$ $\tilde{\Omega} = \sqrt{\nu^2 / 4 - \omega_0^2}$,

$G_j = \xi^{-a_j} \gamma(a_j, \xi) + \xi^{-b_j} \gamma(b_j, \xi)$ $\quad$ and $\quad$ $F_j(t) =$

$= z^{-a_j}(t) \gamma(a_j, z(t)) - z^{-b_j}(t) \gamma(b_j, z(t))$, $\qquad$ here

$a_j = \xi + i\omega_j / \nu_r$, $\quad$ $b_j = \xi - i\omega_j / \nu_r$, $\quad$ $z(t) = \xi e^{-\nu_r t}$,

$\omega_{1,2} = -i\nu_t / 2 \pm i\tilde{\Omega}$, a $\gamma(s, z) = \int_0^z y^{s-1} e^{-y} dy$ is the

lower incomplete gamma function.

In the oscillatory motion regime $(\omega_0 / \nu_t > 1/2)$,

$$\langle x(t) x(0) \rangle = \frac{V_0^2 \alpha e^\xi}{4\omega_0^2} \times$$

$$\times \left\{ \begin{array}{l} e^{-\frac{\nu_t t}{2}} \left[\begin{array}{l} \left(\mathrm{Re}[G_2] + \dfrac{\nu_t}{2\Omega} \mathrm{Im}[G_2] \right) \cos(\Omega t) + \\[2mm] + \left(\dfrac{\nu_t}{2\Omega} \mathrm{Re}[G_2] - \mathrm{Im}[G_2] \right) \sin(\Omega t) \end{array} \right] + \\[6mm] + e^{-D_r t} \left(\mathrm{Re}[F_2(t)] + \dfrac{\nu_t}{2\Omega} \mathrm{Im}[F_2(t)] \right) \end{array} \right\}, \qquad (8b)$$

where $\mathrm{Re}[\ldots]$ and $\mathrm{Im}[\ldots]$ are real and imaginary parts of complex functions, and $\Omega = i\tilde{\Omega}$.

In the stationary state at $t = 0$, function $\langle x(t) x(0) \rangle$ describes the mean square position of the particle relative to the trap center:

$$\langle x^2 \rangle = \frac{V_0^2 \alpha e^\xi}{4\omega_0^2} \left\{ C_+ \frac{\gamma(a_1, \xi)}{\xi^{a_1}} + C_- \frac{\gamma(a_2, \xi)}{\xi^{a_2}} \right\} \quad \text{for}$$

$\omega_0 / \nu_t < 1/2$, $\qquad\qquad\qquad (9a)$

and

$$\langle x^2 \rangle = \frac{V_0^2 \alpha e^\xi}{2\omega_0^2} \left\{ \mathrm{Re} \left[\frac{\gamma(a_2, \xi)}{\xi^{a_2}} \right] + \frac{\nu_t}{2\Omega} \mathrm{Im} \left[\frac{\gamma(a_2, \xi)}{\xi^{a_2}} \right] \right\}$$

for $\omega_0 / \nu_t > 1/2$. $\qquad\qquad (9b)$

Now, to calculate the evolution function of the particle's mean square displacement in the stationary state, $\mathrm{MSD}(t)$, it is sufficient to substitute (8)–(9) into (3).

It is important to note that equations (9a) and (9b) coincide with those previously obtained in paper [20] and verified against the numerical simulation results. It can also be easily shown that when $\nu_r \to \infty$, equation (8a) reduces to the

known autocorrelation function $\langle x(t) x(0) \rangle_{\mathrm{AOUP}}$ for the active Ornstein-Uhlembeck particle model, which is often used for the approximate description of active Brownian particle dynamics with only translational inertia considered [16, 17]. When $\omega_0 = 0$, the expression for $\mathrm{MSD}(t)$ can be reduced to the formula derived in paper [19] for a free, fully inertial active Brownian particle. The listed facts confirm that the formulas derived in this paper are correct.

With high trap frequency ($\omega_0 \to \infty$) at times $t \gg \omega_0^{-1}$, the expression applying to particle's $\mathrm{MSD}(t)$ and described by formulas (3), (8b), and (9b), becomes significantly simpler and can be represented in terms of elementary functions:

$$\mathrm{MSD}(t) \approx \mathrm{MSD}(\infty) \times$$
$$\times \left\{ 1 - \exp \left[-\frac{D_r}{\nu_r} \left(\nu_r t - 1 + e^{-\nu_r t} \right) \right] \right\}, \qquad (10)$$

where

$$\mathrm{MSD}(\infty) = \frac{(V_0 \nu_t)^2}{\omega_0^4}. \qquad (11)$$

An interesting feature is the absence of oscillations in formula (10), which are specific to the mean square displacement evolution for both passive particles [21] and active Ornstein-Uhlenbeck particles [16]. The figure shows normalized $\mathrm{MSD}(t)$ for a spherical active Brownian particle with $D_r / \nu_r = 1$ and $\omega_0 / \nu_t = 1000$. For comparison, $\mathrm{MSD}(t)$ for the active Ornstein-Uhlenbeck particle (AOUP) with $\omega_0 / \nu_t = 1000$ and without considering the particle's rotational inertia is added to the figure.

It is easy to see that within a strong trap, $\mathrm{MSD}(\infty)$ of a fully inertial active particle does not depend on ν_r, and therefore, on particle's rotational inertia. Furthermore, $\mathrm{MSD}(\infty)$ coincides with the mean square displacement of the active Ornstein-Uhlenbeck particle [16] when $t\nu_t \gg 1$ and $D_r / \nu_t \ll 1$. The latter is true, for example, for a particle with a radius of ~ 1 μm in a gas at a pressure of ~ 1000 Pa or higher.
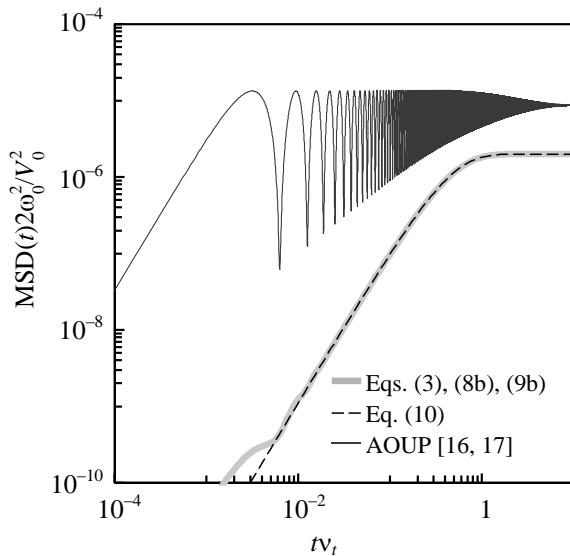
Normalized mean square displacement of an active particle at $\omega_0/\nu_t = 1000$ as a function of time. The thick solid line represents the fully inertial model with $D_r/\nu_t = 1$; the thin solid line represents the AOUP model without accounting for the particle's rotational inertia.

Conclusion

Analytical expressions describing the evolution of a particle's mean square displacement in a harmonic trap have been derived for the first time within the framework of the active Brownian particle model with translational and rotational inertia. The results of this paper can be useful for describing the dynamics of light-sensitive active microparticles in gas discharge plasmas [4, 5], superfluid helium [6], and vacuum optical traps [22], as well as microswimmers in acoustic traps [23], macroscopic vibrobots in parabolic confinement [9], and others. Macroscopic inertial active particles driven by vibration and moving along finite trajectories can be used as a controllable analogue of vehicles or pedestrians for modeling congestion at bottlenecks in optimizing transportation systems and designing public spaces [24]. Macroscopic inertial active particles can be used in creating mechanical metamaterials and autonomous devices driven by vibration [25, 26]. Ideas for creating microscopic heat engines based on inertial active matter are also discussed [27, 28].

REFERENCES

1. Aranson I. S., Active colloids. Physics-Uspekhi **56** (1), 79 (2013).
2. Elgeti J., Winkler R. G. and Gompper G., Rep. Prog. Phys. **78**, 056601 (2015).
3. Bechinger C., Di Leonardo R., Löwen H., Reichhardt C., Volpe G. and Volpe G., Rev. Mod. Phys. **88**, 045006 (2016).
4. Nosenko V., Luoni F., Kaouk A., Rubin-Zuzic M. and Thomas H., Phys. Rev. Res. **2**, 033226 (2020).
5. Arkar K., Vasiliev M. M., Petrov O. F., Kononov E. A. and Trukhachev F. M., Molecules **26**, 561 (2021).
6. Petrov O. F., Boltnev R. E. and Vasiliev M. M., Sci. Rep. **12**, 6085 (2022).
7. Leoni M., Paoluzzi M., Eldeen S., Estrada A., Nguyen L., Alexandrescu M., Sherb K. and Ahmed W. W., Physical Review Research **2** (4), 043299 (2020).
8. Deblais A., Barois T., Guerin T., Delville P. H., Vaudaine R., Lintuvuori J. S., Boudet J. F., Baret J. C. and Kellay H., Physical review letters **120** (18), 188002 (2018).
9. Dauchot O. and Démery V., Physical review letters **122** (6), 068002 (2019).
10. Jiang H. R., Yoshinaga N. and Sano M., Physical review letters **105** (26), 268302 (2010).
11. ten Hagen B., van Teeffelen S. and Lowen H., J. Phys.: Condens. Matter **23**, 194119 (2011).
12. Szamel G., Physical Review E **90** (1), 012111 (2014).
13. Das S., Gompper G. and Winkler R. G., New Journal of Physics **20** (1), 015001 (2018).
14. Chaudhuri D. and Dhar A., Journal of Statistical Mechanics: Theory and Experiment **2021** (1), 013207 (2021).
15. Caraglio, M. and Franosch, T. Physical Review Letters **129** (15), 158001 (2022).
16. L. Caprini and U. M. B. Marconi, The Journal of Chemical Physics, **154** (2), 024902 (2021).
17. Nguyen G. P., Wittmann R. and Löwen H., Journal of Physics: Condensed Matter. **34** (3), 035101 (2021).
18. Lisin E. A., Vaulina O. S., Lisina I. I. and Petrov O. F., Physical Chemistry Chemical Physics **24** (23), 14150–14158 (2022).
19. Sprenger A. R., Caprini L., Löwen H. and Wittmann R., Journal of Physics: Condensed Matter. **35** (30), 305101 (2023).

20. Gutierrez-Martinez L. L. and Sandoval M., The Journal of Chemical Physics **153** (4), 044906 (2020).

21. Uhlenbeck G. E. and Ornstein L. S., Physical review **36** (5), 823 (1930).

22. Li T., Kheifets S., Medellin D. and Raizen M. G., Science **328** (5986), 1673–1675 (2010).

23. Takatori S. C., De Dier R., Vermant J. and Brady J. F., Nature communications **7** (1), 10694 (2016).

24. Rozenblit A., Buzakov M., Molodtsova A., Dmitriev A. and Olekhno N. 18th International Conference on Management of Large-Scale System Development, 2025. doi: 10.1109/MLSD65526.2025.11220665

25. Wang J., Wang G., Chen H., Liu Y., Wang P., Yuan D., Liu L. et al., Nature communications **15** (1), 8853 (2024).

26. Ning L., Zhu H., Yang J., Zhang Q., Liu P., Ni R. and Zheng N., National Science Open **3** (4), 20240005 (2024).

27. Kumari A., Pal P. S., Saha A. and Lahiri S., Physical Review E **101** (3), 032109 (2020).

28. Hecht L., Mandal S., Löwen H. and Liebchen B., Physical Review Letters **129** (17), 178001 (2022).

About authors

Lisin Evgeny Alexandrovich, Candidate of Physical and Mathematical Sciences, Senior Researcher, Laboratory of Dusty Plasma Diagnostics, Joint Institute for High Temperatures, Russian Academy of Sciences (125412, Russia, Moscow, Izhorskaya st., 13, bldg. 2); Senior Researcher, Laboratory of Active Matter and Systems Physics, Moscow Institute of Physics and Technology (141701, Russia, Moscow region, Dolgoprudny, Institutsky Per., 9). E-mail: eaLisin@yandex.ru AuthorID: 179843, Scopus Author ID 32867795100, ORCID 0000-0001-5498-0321, Web of Science Researcher M-1738-2016

Lisina Irina Igorevna, Candidate of Physical and Mathematical Sciences, Senior Researcher, Laboratory of Dusty Plasma Diagnostics, Joint Institute for High Temperatures, Russian Academy of Sciences (125412, Russia, Moscow, Izhorskaya st., 13, bldg. 2); Senior Researcher, Laboratory of Active Matter and Systems Physics, Moscow Institute of Physics and Technology (141701, Russia, Moscow region, Dolgoprudny, Institutsky Per., 9). E-mail: irina.lisina@mail.ru SPIN code: 5802-2312, AuthorID: 923626, Scopus Author ID 21743105800, Web of Science Researcher E-8876-2017

━━━━━━━━━━━━━━━━━━ PHYSICAL SCIENCE OF MATERIALS ━━━━━━━━━━━━━━━━━━

Electrical and optical properties of silicon-carbon films deposited by electron beam evaporation of silicon carbide in gas environment

V. A. Burdovitsin[*], L. J. Ngon A Kiki, E. M. Oks and F. A. Sukhovolsky

Tomsk State University of Control Systems and Radioelectronics, Tomsk, 634050 Russia
[*] E-mail: burdov@fet.tusur.ru

Silicon-carbon films were prepared by electron beam evaporation of silicon carbide in nitrogen, oxygen, helium and propane. Electron beam was produced by electron source with plasma cathode. The resistivity, conductivity activation energy, optical band gap as well as element content of silicon-carbon films obtained at different temperatures were measured. It is shown that a change in the films properties with the deposition temperature correlates with a change in the ratio of elements in the films.

Introduction

Silicon-carbon (SiC) films, i.e., films made of silicon carbide containing additional elements such as oxygen, nitrogen, and hydrogen, are used for passivating contacts of silicon solar cells [1, 2] and also as a material for solar cells [3]. This promotes the interest in the electrical properties of such films. Among multiple methods for depositing silicon-carbon films, a specific place is occupied by vacuum methods, and in particular, electron beam evaporation. The advantages of this method compared to traditional plasma-chemical deposition include a relatively high deposition rate (up to several micrometers per minute), ability to deposit at low (down to room) temperatures of a substrate, and absence of toxic organometallic compounds. In papers [4–6], silicon carbide was evaporated using thermionic electron guns, which imposes limitations on both the range of operating pressures and the ability to evaporate material in reactive gases. This paper utilizes an electron source with a plasma cathode [7], which provides operability in various gases at pressures within the range of units to tens of Pascals. As some papers [8–10] emphasize, the electrical and optical properties of silicon-carbon films are largely determined by deposition conditions. Films deposited by the plasma-chemical deposition method with plasma generated by radio-frequency discharge feature the activation mechanism of electrical conductivity with activation energy $Ea = 0.1–0.9$ eV [8], which increases as the power input into the discharge grows. At the same time, the resistivity also increases within the range of $10^2–10^9$ $\Omega \cdot$cm. The paper authors report that the increase in power is accompanied by a change in the Si/C atomic concentration ratio from 9 to 2.3, i.e., by elimination of excess silicon. Films deposited by reactive magnetron sputtering of silicon in methane [10] have the resistivity ranging from 1.3×10^3 to 9.4×10^9 $\Omega \cdot$cm and the activation energy of 0.16 to 1 eV with the methane flow rate increasing. At the same time, the deposition rate decreases from 30 to 12 nm/min, and Si/C atomic concentration ratio also decreases from 2.5 to

0.17. It should also be noted that optical band gap Eg grows from 1.7 to 2.7 eV. Only one paper [4] is devoted to studying the electrical conductivity mechanism of the films deposited by electron beam evaporation. As indicated in paper [4], the film resistivity exhibits non-monotonical dependence on the deposition temperature in the range of 300–575 K, while the activation energy is 0.16 eV.

According to paper [5], the resistivity of thin silicon carbide films generated by electron beam evaporation does not depend on the deposition temperature. Both in [4] and [5], the composition of the gas environment in the vacuum chamber was not controlled. These results call for further studies of the electrical properties of silicon-carbon films vs. the deposition temperature and gas environment composition during electron beam evaporation.

The purpose of this work is to study the electrical and optical properties of silicon-carbon films deposited by the electron beam evaporation of silicon carbide in various gases vs. the deposition temperature.

Experimental technique and methodology

The experiments were conducted using the electron beam evaporation setup described previously in paper [11]. The stainless steel working chamber housed a black-lead crucible with a target sintered from silicon carbide powder, and three substrate holders with individual heaters equipped with thermocouples for measuring the deposition temperature T_{dep}. The substrate holders were shielded by motorized shutters. Optical measurements were performed using SF 2000 spectrophotometer for the films deposited on quartz substrates. Polycore plates sized 15×20 mm and 1-mm thick were used as substrates for electrical measurements. Copper strips 1 mm wide were pre-deposited onto the substrates by vacuum evaporation.

The substrates were placed in the substrate holders, and the working chamber was evacuated using a mechanical pump to a pressure of 1 Pa. After this, the working gas such as nitrogen, oxygen, helium, or propane was injected into the chamber, followed by purging during 10 minutes with simultaneous heating of the substrate holders. At the operating pressure of 4 Pa, the electron source was activated, and emission current I_e and accelerating voltage U_a were gradually increased until evaporation of the target began. After the operating parameters of $I_e = 90$ mA and $U_a = 11$ kV were reached, the shutters were opened, and films were deposited. The process ended by switching off the electron source. After being cooled, the substrates were removed from the chamber and placed in the thermal evaporation setup, where copper strips were deposited perpendicular to the lower ones. The capacitor structures prepared this way were placed in a temperature-controlled space, and current-voltage characteristics were measured at different temperatures. Current was measured using F 195 instrument (Russia). Film thickness was determined using MII-4 interference microscope (LOMO, Russia). Based on these measurements, the resistivity was calculated. The elemental composition was determined using TM-1000 scanning electron microscope (Hitachi, Japan) equipped with EDS-SWIFT energy-dispersive spectroscopy attachment (Great Britain).

Experiment results and discussion

The current-voltage characteristics of metal–SiC film–metal structures exhibited a linear pattern. The slope of the characteristics changed as the measurement temperature changed. Resistance was determined based on the value of derivative dU/dI at U = 0 [12]. The curves of resistivity ρ of the films deposited in different gases (Fig. 1) show a decrease of ρ as the deposition temperature increased. Moreover, the highest resistivity was demonstrated by the films deposited in oxygen and propane.

The logarithm of film resistance features the linear dependence on the reciprocal temperature, thus indicating the conductivity activation mechanism. Conductivity activation energies E_a, determined from the slope of the straight lines are shown in Fig. 2a. As is seen, the values of E_a also decrease as the deposition temperature increases. The nature of the derived curves correlates with the behavior of optical band gap E_g, derived from processing transmittance spectra in the visible region using Tauc coordinates [13] (Fig. 2b). It is worth noting that the values of E_a and E_g differ significantly.
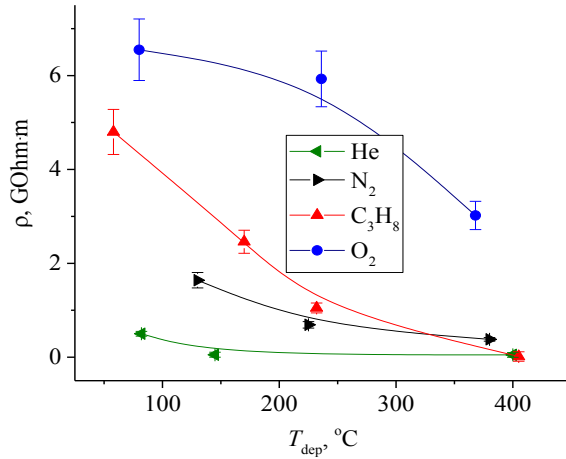
Fig. 1. Resistivity of the films deposited different gases vs. deposition temperature T_{de}

a)

b)
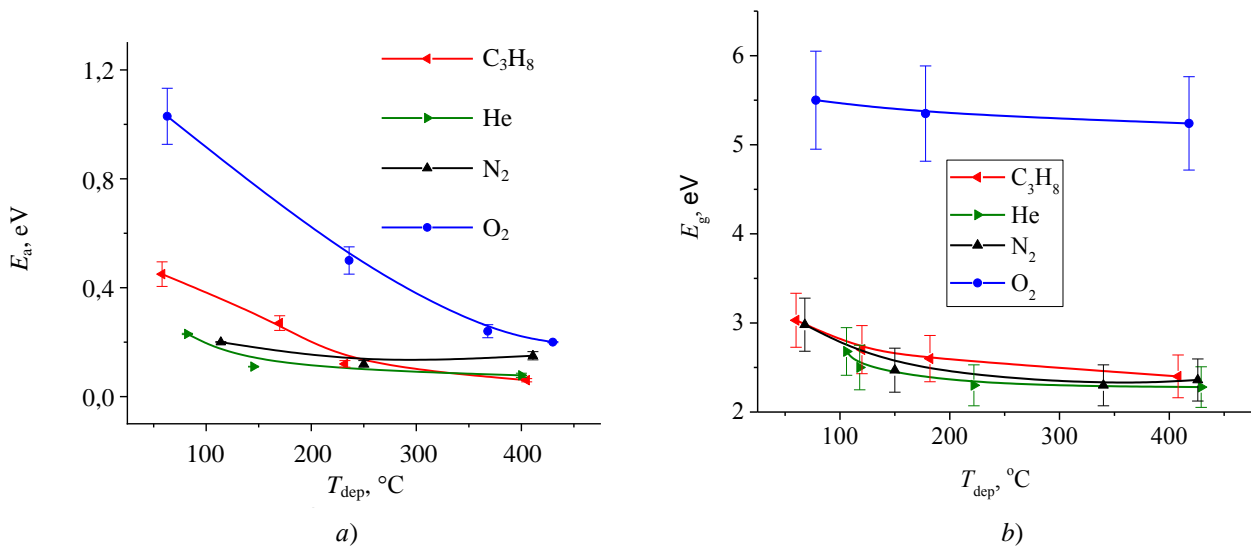
Fig. 2. Values of activation energy E_a (a) and optical band gap E_g vs. deposition temperature Tdep in different gases

Parallel measurements of film composition allow for some assumptions regarding the reasons for the change in resistivity depending on the deposition temperature. Temperature increase causes a rise in the relative silicon content (Fig. 3). This result agrees with the data presented in papers [4, 6] where decreased atomic concentration ratio Si/C is recognized as the primary cause for the increase in E_g and E_a values. It should be noted, however, that in our case, oxygen plays a certain role. Its content changes only slightly as the deposition temperature increases; consequently, the Si/O ratio increases as well with the rising deposition temperature. The reason for the increased silicon content with temperature is likely due to a faster decrease in the adsorption of gas molecules and carbon atoms compared to silicon atoms. An argument in favor of this assumption is the higher adsorption energy of carbon compared to

silicon, and therefore a stronger dependence of its adsorption on temperature [14]. Furthermore, since carbon monoxide is a gas, the interaction of carbon with oxygen as the temperature grows also contributes to decreased carbon content in the film, as the gas is carried away into the pumping system. Resistivity values of the deposited films allow them to be classified as semiconductor materials. The relatively low activation energy indicates that the film material has properties differing significantly from those of crystalline silicon carbide. This is also evident during the analysis of optical transmittance spectra. The E_g value determined from these spectra and lying within 2–3 eV (Fig. 2b) is in reasonable agreement with the values of this parameter for crystalline SiC. The difference observed between the values of E_g and E_a can be explained by the fact that donor-type impurity levels [15] are assumed to be present within the band gap of the

films, with a depth corresponding to the measured E_a values. These levels can be caused both by impurities, namely hydrogen and oxygen, and by the amorphous structure of the film. The latter assumption is quite probable because the known papers [8–10] devoted to the electrical properties of silicon-carbon films report E_a values equaling to the deciles of electronvolt.
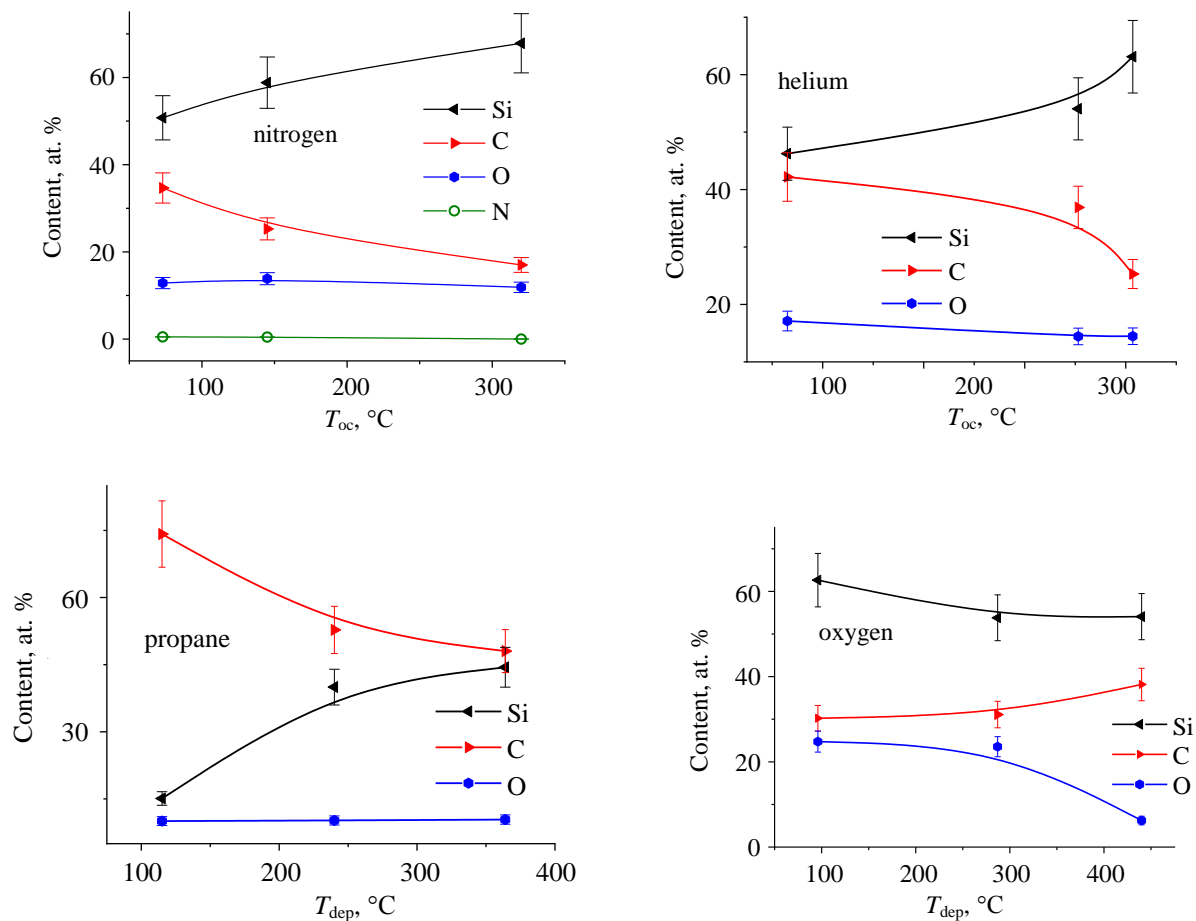
Fig. 3. Composition of the films deposited in different gases vs. deposition temperature T_{dep}

Conclusion

The measurements performed are indicative of the conductivity activation mechanism for silicon-carbon films produced by electron beam evaporation of silicon carbide in different gases. The activation energy value ranges from 1.0-0.1 eV depending on the gas type and decreases as the deposition temperature increases. The resistivity of the films is 10^8–10^9 Ω·m and tends to decrease with the increasing deposition temperature. The observed regularities are explained within the framework of concepts about the change in film composition towards silicon enrichment with the increasing deposition temperature.

REFERENCES

1. Xu Z., Tao K., Jiang S., Jia R., Li W., Zhou Y. et al., Solar Energy Materials and Solar Cells. **206**, 110329 (2020).
2. Muhanad A. A., Mohammed M. S. and Wathiq R. A., The Scientific Journal of Koya University **9**, 10852 (2021).
3. Shan D., Sun D., Wang M. and Cao Y., Crystals **14**, 45 (2024).

4. Bunton G. V., J. Phys. D: Appl. Phys. **3**, 232–236 (1970).

5. Yi J., He X. D. and Sun Y., Journal of Alloys and Compounds. **461**, L11–L13 (2008).

6. Zheng J., Ye L., Hu Y., Huang Y., Yu J. and Chen T., Vacuum **211**, 111979 (2023).

7. Burdovitsin V. A. and Oks E. M., Russian Physics Journal **63**, 1678–1685 (2021).

8. Ambrosone G., Basa D. K., Coscia U., Santamaria L., Pinto N., Ficcadenti M. et al., Energy Procedia **2**, 3–7 (2010).

9. Vetter M., Voz C., Ferre R., Martin I., Orpella A. et al., Thin Solid Films **511–512**, 290–294 (2006).

10. Tavsanoglu T., Zayim E. O., Agirseven O., Yildirim S. and Yucel O., Thin Solid Films **674**, 1–6 (2019).

11. Burdovitsin V., Bakeev I., Ngon A. Kiki L., Oks E. and Tyunkov A., High Temperature Material Processes **29**, 1–7 (2024).

12. Chang C. Y., Fang Y. K. and Sze S. M., Solid-State Electronics **14**, 541–550 (1971).

13. Tauc J., Materials Research Bulletin **3**, 37–46 (1968).

14. Cahyadi Erica. UCLA Electronic Theses and Dissertations. 2012. https://escholarship.org/uc/item/7c35n3n0

15. Dubrovskii G. B. and Radovanova E. I., Phys. Stat. Sol. (b) **48**, 875–879 (1971).

About authors

Burdovitsin Viktor Alekseyevich, Dr. Sci. (Eng.), Senior Research Scientist Tomsk State University of Control Systems and Radioelectronics (634050, Russia, Tomsk, 40 Lenina Prospekt). E-mail: burdov@fet.tusur.ru SPIN code: 5044-2693, AuthorID: 36336

Ngon A Kiki Lionel Joel, Engineer Tomsk State University of Control Systems and Radioelectronics (634050, Russia, Tomsk, 40 Lenina Prospekt). E-mail: joelngon52@gmail.com SPIN code: 2617-5472, AuthorID: 1273207

Oks Efim Mikhailovich, Dr. Sci. (Eng.), Professor, Head of Laboratory Tomsk State University of Control Systems and Radioelectronics (634050, Russia, Tomsk, 40 Lenina Prospekt). E-mail: oks@fet.tusur.ru SPIN code: 6422-5057, AuthorID: 18767

Sukhovolsky Fyodor Aleksandrovich, Master's Student Tomsk State University of Control Systems and Radioelectronics (634050, Russia, Tomsk, 40 Lenina Prospekt). E-mail: spectrumz12@yandex.ru

Enhanced permeability of polyamide fabrics for silver nanoparticles via modification with boron nitride

I. V. Loktionova[1,*], P. V. Abakumov[2], A. P. Kuzmenko[1], A. I. Kolpakov[1], V. A. Mamontov[1], E. A. Novikov[1] and L. P. Petrova[1]

[1] *Southwest State University, Kursk, 305040 Russia*
[*] *E-mail: ms.chuhaeva@mail.ru*
[2] *Kursk State Medical University, Kursk 305041 Russia*

Polyamide membranes modified with boron nitride nanoparticles were studied for silver nanoparticle filtration. Atomic force microscopy revealed the formation of ordered nanolayers (particle size ~ 20 nm, roughness 24 nm). Raman spectroscopy confirmed the formation of chemical bonds while preserving the polyamide structure. The modified samples exhibited a high transmission coefficient (97–98%), exceeding that of the unmodified fabric by 35%, which is consistent with molecular dynamics simulation data. The obtained results demonstrate the potential of using modified polyamide membranes for efficient silver nanoparticle filtration.

Introduction

Filtration of colloidal solutions of metal nanoparticles, such as Ag, Au, Pt, Cu, Fe, and others presents a particular challenge in various applications of nanomaterials due to aggregation and interaction of the solutions with surfaces of filtering materials [1]. Polyamide membranes in filtration systems have found widespread use due to their availability, mechanical strength, stability, and durability in aggressive environments [2]. Modifying polyamide with nanoparticles of boron nitride (BN) featuring unique properties [3] enables the formation of ordered nanoporous structures with low hydrodynamic resistance and increased throughput, partly due to their resistance to swelling [4, 5]. Thus, paper [6] shows that introducing 5 wt.% BN into polyamide increases the average pore size from 50 nm to 80–100 nm and overall porosity by 15–20 %, creating branched nanochannels that enhance filtration

rates by 25–30 % [7, 8]. Incorporation of 3 wt.% BN reduces water flow resistance by 40% compared to unmodified polyamide [9], while introducing 5 % BN halves water absorption [10].

This reduces swelling, prevents pore clogging, and deformation of membrane cells, thus ensuring long-term stability of characteristics [7, 9]. Thus, modification of polyamide materials with boron nitride improves their throughput and operational stability.

This paper is aimed to research the features of filtering a colloidal solution of silver nanoparticles through PA6 fabric modified with boron nitride nanoparticles by the Langmuir-Blodgett method and magnetron sputtering.

Materials and Methods

Two methods were used to deposit nanofilms of boron nitride nanoparticles onto polyamide fabric (PA 6) with a thread diameter of

~400 μm, which consists of hundreds of thin filaments and has a smooth mesh surface. The Langmuir-Blodgett (LB) method was employed to form LB NF *h*-BN / PA 6 nanofilms (NF) on the surface of deionized water (18 MΩ·cm) under normal conditions using KSV Nima 2002 setup from a colloidal system (CS) of BN nanoparticles stabilized with stearic acid (SA). CS of 3-μl volume was applied onto the subphase surface. The transfer pressure was 20 mN/m. The high-frequency magnetron sputtering (MR) method was used to deposit MR NF BN / PA 6 nanofilms using MSU TM-MAGNA setup. A target of hexagonal boron nitride (*h*-BN) with a diameter of 100 mm was used. The working atmosphere consisted of nitrogen (0.25 l/h N_2) with the addition of argon (0.03–0.2 l/h Ar). The MR process was conducted during 3600 s at the power of 300 W. Prior to sputtering, the chamber was evacuated to 5×10^{-4} mmHg. The polyamide substrate was heated to 420 K.

The morphology of the Langmuir nanofilms was studied using scanning probe microscopy (SPM) SmartSPM (AIST-NT). Raman spectroscopy (RS) was performed using microspectrometer OmegaScope (AIST-NT) in $ZXX\overline{Z}$ geometry ($\lambda = 473$ nm, from 170 cm^{-1}) and spectrometer LabRAM HR (Horiba) in $ZXY\overline{Z}$ geometry ($\lambda = 532$ nm, from 50 cm^{-1}), both with an identical spectral resolution of 0.8 cm^{-1}. The optical properties of CS were measured using spectrophotometer SF-2000 (range of 190–1100 nm). Filtration efficiency was determined by changes of the optical density of CS after passing it through original PA 6 fabric and modified samples (LB NF *h*-BN/PA 6 and MR NF BN/PA 6). To establish the reproducibility of findings, all experiments were conducted three times. The CS nanoparticle sizes were determined by small-angle X-ray scattering (SAXS) on SAXSess mc^2 diffractometer (Anton Paar, Cu Kα, $\lambda = 0.154$ nm, resolution 0.03–28 nm^{-1}). The colloidal system of silver nanoparticles was synthesized using the Kerry Lee method.

Filtration of Ag particles by the PA 6 matrix was modeled in Materials Studio 2020 using Forcite and Amorphous Cell modules. At first atomic-scale models of PA 6, water, and silver were created, with geometry optimization performed using the Universal Force Field (including van der Waals and Coulombic interactions, Ewald summation method). Then, in Amorphous Cell, a periodic cell of an aqueous Ag solution (~10 wt.%) was formed, its structure was optimized, and molecular dynamics simulation was carried out (NVT ensemble, 298 K, 105 ps, time step 1.5 fs).

Findings and Discussion

Analysis of the formed nanostructured layer LB NF *h*-BN / PA 6 by SPM method revealed characteristic lateral particle sizes of ~20 nm (Fig. 1). The root-mean-square roughness of the LB NF *h*BN film layer on the PA 6 surface slightly increased and reached 24 nm (inset in Fig. 1). The roughness was measured at five different points on the membrane, and the calculated standard deviation from these measurements was 1.3 nm, which reflects surface variability and reliability of estimated mean values. A predominant orientation of particles between the primary fibers (filaments) of the fabric was observed, which is attributed to the action of capillary forces during formation of LB NF *h*-BN / PA 6.
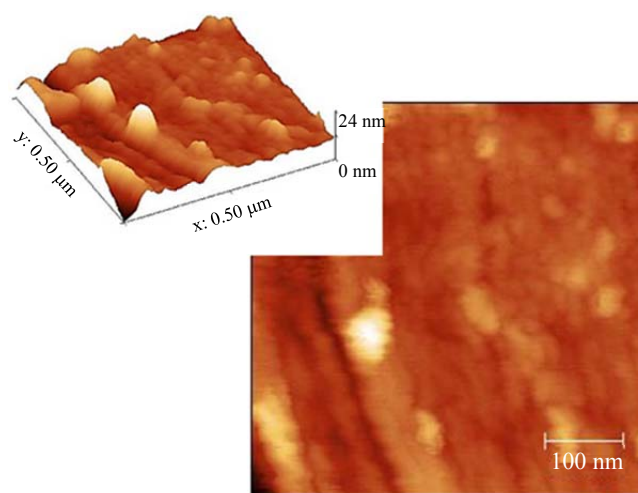

Fig. 1. SPM image of polyamide fabric modified with boron nitride nanoparticles. The inset shows the root-mean-square roughness of the LB NF h-BN film layer.

In $ZXY\overline{Z}$ RS spectra of LB NF *h*-BN / PA 6 and MR NF BN / PA 6 samples, vibrational modes characteristic of both the polymer matrix

and deposited functionalized film were observed (Fig. 2). In the low-frequency region of the spectrum (< 500 cm^{-1}), the *LA* mode of the boron-nitrogen lattice vibrations of *h*-BN at 149 cm^{-1} was excited. Its intensity was noted to grow after functionalization of *h*-BN with stearic acid. These changes in the surface polarizability of NF are due to the formation of chemical bonds between BN and carboxylate groups [11, 12].

The 478 cm^{-1} line corresponds to deformation vibrations of B–O bonds arising from partial oxidation of the *h*-BN surface or to low-frequency modes of amorphous BN (B–N–B bending vibrations). The 518 cm^{-1} signal can be attributed either to skeletal vibrations of the polyamide matrix (C–C–N–C deformation) or to defect modes of BN associated with nitrogen vacancies or boron atom substitutions [10].
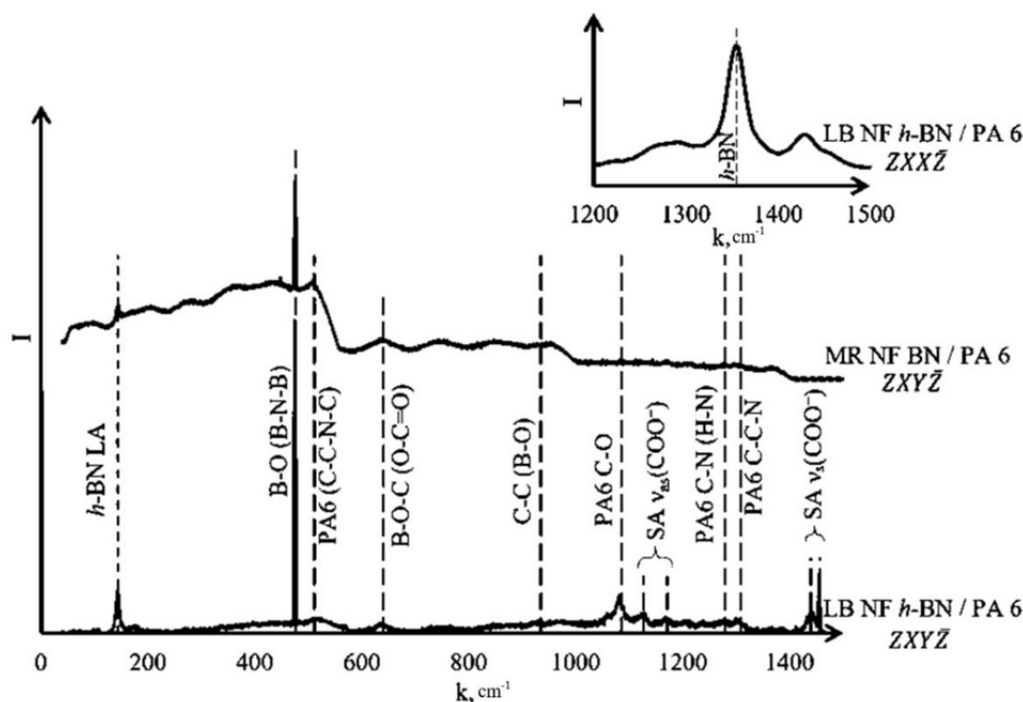
Fig. 2. Polarized ZXYZ̄ Raman spectra for filter samples obtained by modifying PA6 with BN nanoparticles using LB and MR methods. The inset shows an example of the ZXXZ̄ Raman spectrum for LB NF h-BN / PA 6 sample.

In the mid-frequency region (500–1000 cm^{-1}), vibrations associated with the interaction between BN and stearic acid dominated. For instance, the peak at 643 cm^{-1} corresponded to deformation vibrations of carboxylate groups (O–C=O) in boron stearate, as well as to valence vibrations of B–O–C bonds, which confirmed the formation of chemical bonds between stearic acid molecules and BN surface. The signal at 930 cm^{-1} included contributions from valence vibrations of C–C in the polyamide chain and symmetric vibrations of B–O in boroxol structures (B–O–B), which could form due to partial hydrolysis of BN [13, 14].

In the 1000–1500 cm^{-1} region, key modes were associated with carboxylate groups and amide structures. The peak at 1085 cm^{-1}

corresponded to valence vibrations of C–O in ether bonds of polyamide and antisymmetric vibrations of carboxylates (v_{as}(COO$^-$)). The doublet at 1132/1182 cm^{-1} unambiguously identified the carboxylate group of stearic acid, where 1132 cm^{-1} corresponded to symmetric (v_s(COO$^-$)) and 1182 cm^{-1} to antisymmetric (v_{as}(COO$^-$)) vibrations. This indicated the deprotonation of acid and the formation of boron stearate. The peak at 1285 cm^{-1} is characteristic of amide III in polyamides (combination of C–N stretching and N–H deformation), which indicated that the structural integrity of the polymer matrix remained. The signal at 1310 cm^{-1} is related to crystalline phases of polyamide (ordered C–C–N segments) and deformation vibrations of CH$_2$ groups. Peaks at 1423 cm^{-1} and

1457 cm^{-1} corresponded to symmetric carboxylate vibrations ($\nu_s(\text{COO}^-)$) and deformation vibrations of CH_2 chains in polyamide and stearic acid, thus confirming that both components were present in the system in accordance with [11, 12]. The main peak for h-BN at 1370 cm^{-1} in the non-polarized $ZXX\overline{Z}$ Raman $ZXX\overline{Z}$-spectrum confirmed the successful deposition of nanoparticles onto PA 6 fibers (inset to Fig. 2).

The absorption spectrum of CS of silver nanoparticles exhibited two distinct but diffused maxima in the wavelength regions around 440 nm and 720 nm (Fig. 3).

These peaks corresponded to characteristic manifestations of the surface plasmon resonance (SPR), which arose from collective oscillations of free electrons on the surface of metallic nanoparticles under the influence of the electromagnetic field of incident light [15]. The inset in Figure 3 also shows the SAXS results for this CS, which indicate its heterogeneous nature with nanoparticles sized 29, 56 and 100 nm. The conclusions drawn from the absorption spectra (Fig. 3) were supported by three well-defined peaks observed in the SAXS spectrum. Their occurrence indicated a discrete particle size distribution and good stabilization of CS. Similar polymodal SAXS spectrum structure is typical for complex CS. The symmetry and width of the dominant 56 nm peak suggested a high degree of CS monodispersity. The peak width at 100 nm indicated a significant spread of sizes within this group.
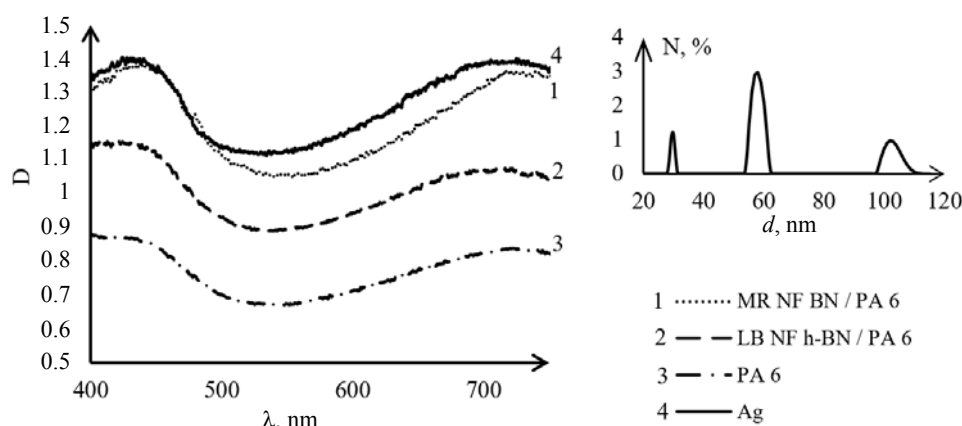
Fig. 3. Photometric spectra of CS of Ag nanoparticles before and after filtration. The inset shows the size distribution of silver particles (SAXS)

1 ········ MR NF BN / PA 6
2 — — LB NF h-BN / PA 6
3 — · · - PA 6
4 ——— Ag

For CSs containing monodisperse spherical silver nanoparticles of small sizes (10–30 nm), SPR is typically observed in the blue part of the spectrum, around 400 nm. However, in this case, the main peak is shifted to the 440 nm region and is noticeably broadened, which allowed concluding about the polydisperse nature of the solution, i.e., the presence of particles sized within a broad spread. The shift toward longer wavelengths (red shift) could be due to the increased average particle diameter: as the size of silver nanoparticles grows (inset to Fig. 3 – 56 nm), SPR shifts to the region of lower energies with a longer wavelength, resulting in a bathochromic shift. The occurrence of SPR maximum in the 720 nm region indicated the formation of silver nanoparticle aggregates. According to paper [16], the interaction between their plasmon modes in such conditions was accompanied by additional absorption bands typically occurring in the red or near-infrared region of the spectrum, and is attributed either to direct contact of particles or their close proximity in the CS solution – within the framework of so-called "plasmon coupling". The decrease of optical density in the yellow and green regions of the spectrum could be caused by intensified light scattering by silver nanoparticle aggregates with sizes over 100 nm.

According to the Lambert-Beer-Bouguer law, optical density D is directly proportional to concentration c of CS. Therefore, dependence $D(\lambda)$ in Figure 3 is unambiguously related to the concentration of Ag nanoparticles in CS. Consequently, the transmission of Ag nanoparticles through the filter samples (MR NF BN / PA 6 and LB h-NF BN / PA 6) varied depending on their sizes, as confirmed by the excitation of two SPR peaks and intensified light scattering. Furthermore, the same figure reveals

the closest correspondence between the absorption spectra of CS of Ag nanoparticles before and after filtration through the MR NF BN / PA 6 sample. A comparative assessment of transmission capacity T = DMR/DAg was conducted. Its value was found to be the highest for MR NF BN / PA 6 – T = 98% for Ag nanoparticle sizes of 56 nm, and even for the largest Ag nanoparticle sizes (around 100 nm), T = 97%. In contrast, for the pure fabric, T = 62%. For the LB NF h-BN / PA 6 sample, T = 82%. Thus, a significant increase in the transmission coefficient of Ag nanoparticles was achieved for both PA6-based filter samples modified with boron nitride.

However, when subjected to magnetron sputtering, BN particles penetrate into the polyamide, thus creating a volumetrically modified layer, whereas the LB method forms only a surface film, for which reason it is less effective in reducing the hydrodynamic resistance. The presented findings and their qualitative justification are consistent with the data cited in the introduction.

To assess the degree of penetration and interaction of silver ions with the polyamide structure, curves showing the concentration distribution of silver particles along the vertical axis were plotted for the PA 6 and MR NF BN / PA 6 samples (Fig. 4). The modeled computational cell of 100×100×100 Å was visualized before (0 ps) and after (105 ps) filtration. At the initial time point, water molecules (90 wt.%) and silver particles (10 wt.%) represented within the model as individual atoms with corresponding potentials were located above, in immediate proximity to the membrane.
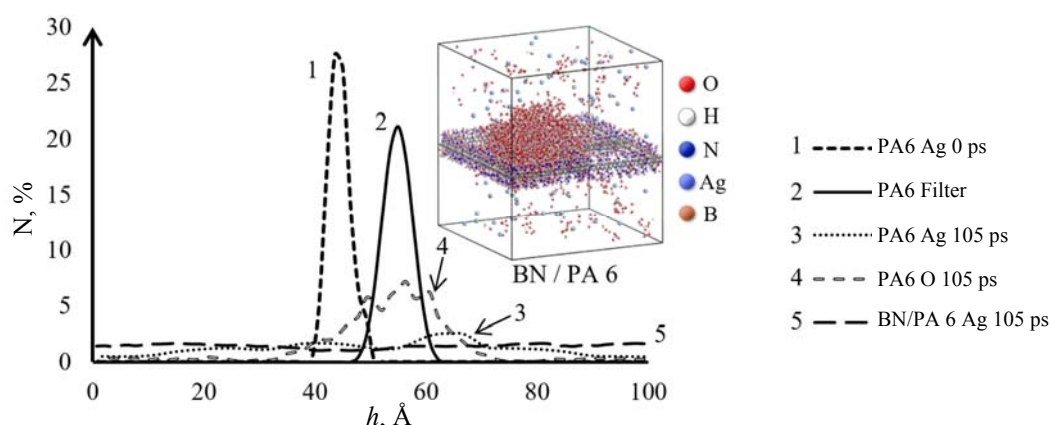
Fig. 4. Spatial distribution of atoms after their passage through the filter, according to Materials Studio 2020 data.

The filtration process involved spatial redistribution of molecules and particles. Thus, during the filtration of Ag particles through MR NF BN / PA 6, the concentration of Ag within the modeled cell became more uniform, and its gradient was minimized, which indicated the minimal interaction between BN and Ag. That is, the transmission capacity of the polyamide fabric for Ag nanoparticles increased. In the sample of pure PA 6 fabric (Fig. 4), redistribution of Ag particles was also noted, with a local increase in their concentration in the boundary regions of the filter (as can be seen in Fig. 4 – PA 6) due to van der Waals interactions. Thus, the results of molecular dynamics modeling fully confirmed the experimental data.

Conclusion

Filter samples based on polyamide fabric PA6 and modified with boron nitride nanoparticles using the Langmuir-Blodgett and magnetron sputtering methods demonstrated an increased transmission coefficient for the colloidal solution of silver nanoparticles. The introduction of boron nitride nanoparticles provided an overall improvement by reducing swelling and hydrodynamic resistance, thereby increasing the transmission capacity of the studied filter samples. This contributed to an increase in their transmission capacity, as demonstrated using the polydisperse (29, 56 and 100 nm) colloidal system of silver nanoparticles. These findings were confirmed by spectroscopic studies

consistent with the conclusions of molecular dynamics modeling that accounted for diffusion and surface effects during filtration.

REFERENCES

1. Yadav K. K. et al., Mater. Today Chem. **40**, 102226 (2024).
2. Seah M. Q. et al., J. Environ. Chem. Eng. 112628 (2024).
3. Molaei M. J. et al., ACS Appl. Electron. Mater. **3** (12), 5165–5187 (2021).
4. Bragaglia M. et al., J. Thermoplast. Compos. Mater. **36** (7), 2862–2882 (2023).
5. Xu Q. et al., Mater. Adv. **4** (6), 1490–1501 (2023).
6. Coogan Á. et al., J. Mater. Chem. A **11** (23), 12266–12281 (2023).
7. Vatanpour V. et al., Ind. Eng. Chem. Res. **63** (12), 5237–5248 (2024).
8. Zheng X. et al., ACS Appl. Mater. Interfaces **15** (23), 28606–28617 (2023).
9. Lu Z. et al., ACS Appl. Nano Mater. **7** (15), 17958–17966 (2024).
10. Randhawa K. S. et al., J. Inorg. Organomet. Polym. Mater. **33** (2), 625–635 (2023).
11. Lin Y. et al., J. Phys. Chem. C **114** (41), 17434–17439 (2010).
12. Bhattacharya A. et al., Phys. Rev. B **85** (3), 035415 (2012).
13. Zhao D. et al., Sci. Rep. **14** (1), 10619 (2024).
14. Salazar-Beltrán D. et al., Polym. Test. **68**, 87–94 (2018).
15. Zulfajri M. et al., Adv. Colloid Interface Sci. 103115 (2024).
16. Xu J. et al., eScience 100312 (2024).

About authors

Loktionova Inna Vladimirovna, Candidate of Physical and Mathematical Sciences, Associate Professor Southwest State University (305040, Russia, Kursk, 50 Let Oktyabrya st., 94). E-mail: ms.chuhaeva@mail.ru ORCID: 0009-0005-7272-2939, SPIN code: 9474-8070, AuthorID: 738514

Abakumov Pavel Vladimirovich, Candidate of Physical and Mathematical Sciences, Associate Professor Kursk State Medical University (305041, Russia, Kursk, K. Marx st., 3). E-mail: abakumovpavel18@gmail.com ORCID: 0009-0009-1055-4019, SPIN code: 7660-5667, AuthorID: 677269

Kuzmenko Alexander Pavlovich, Doctor of Physical and Mathematical Sciences, Professor, Chief Research Scientist Southwest State University (305040, Russia, Kursk, 50 Let Oktyabrya st., 94). E-mail: apk3527@mail.ru ORCID: 0000-0001-7089-0692, SPIN code: 2312-6978, AuthorID: 41744

Kolpakov Artem Igorevich, Postgraduate Student, Southwest State University (305040, Russia, Kursk, 50 Let Oktyabrya st., 94) E-mail: artem.kolpakov.96@mail.ru ORCID: 0009-0004-8571-8544, SPIN code: 8221-5955, AuthorID: 1243978

Mamontov Vladimir Alexandrovich, Postgraduate Student Southwest State University (305040, Russia, Kursk, 50 Let Oktyabrya st., 94). E-mail: vladimir-mamontov2013@yandex.ru ORCID: 0000-0003-0592-3851, SPIN code: 1627-8010, AuthorID: 1118347

Novikov Evgeny Alexandrovich, Candidate of Physical and Mathematical Sciences, Senior Lecturer, Southwest State University (305040, Russia, Kursk, 50 Let Oktyabrya st., 94). E-mail: novikov.2403@mail.ru ORCID: 0000-0002-8824-1540, SPIN code: 7321-5660, AuthorID: 1040884

Petrova Lyudmila Pavlovna, Candidate of Physical and Mathematical Sciences, Associate Professor Southwest State University (305040, Russia, Kursk, 50 Let Oktyabrya st., 94). E-mail: galarina55555@mail.ru ORCID:0009-0007-8883-5983, SPIN code: 7656-4073, AuthorID: 651895

Investigation of vacuum-tight cooled assemblies for FPAs

E. D. Korotaev[1,*], D. I. Guryev[1], A. I. Guryev[1], A. A. Zinkovsky[1], D. I. Morozov[1]
and A. A. Sharov[1,2]

[1] *RD&P Center Orion, JSC, Moscow, 111538 Russia*
* E-mail: korotaevrus@gmail.com
[2] *Moscow State University of Geodesy and Cartography, Moscow, 105064 Russia*

An investigation of the properties of vacuum-tight brazed joints produced by induction brazing for use in components of vacuum cryogenic assemblies of cooled focal-plane arrays (FPAs), specifically in their cold fingers. The specific design features and operational conditions of these joints in micro-cryogenic FPA cooling systems were taken into account. To monitor the helium leak rate, dedicated tooling was developed, which significantly enhanced the ultimate sensitivity of the helium leak detector. The measured helium leak rate of the fabricated assembly samples is 5×10^{-13} Pa·m³/s.

Many types of matrix photo-receiving infrared devices require cooling of the photosensitive element (PSE), including to cryogenic temperatures. To solve the problem of providing the necessary operating temperature of PSE, microcryogenic machines are often built according to the Stirling reverse cycle which can be created both in integral design and according to the Split-Stirling system [1]. The structurally cooled photoreceiver is a microcryogenic machine integrated with a sleeve holder on a cold finger which is equipped with cooled PSE. Sleeve holder acts as a functional element of the body of microcryogenic machine inside which the regenerator with a displacer type piston moves. The inner cavity of the machine and, accordingly, the sleeve holder is filled with a working gas (usually, helium) under high pressure (from 20 to 50 kgf/cm²). At the same time, the sleeve holder is simultaneously a part of the body (cryostat) of the photodetector (usually, evacuated or, less often, gas-filled).

Thus, based on the functional feature of the sleeve holder, the following basic requirements apply to:
 − leak-tightness:
 − freeze-thaw resistance;
 − low levels of heat input;
 − corrosion resistance of materials used for the manufacture of sleeve holders, as well as special requirements for their thermal coefficients of linear expansion (TCLE): to ensure geometrical stability of the device they must be small, and the material of the PSE placement site, additionally, must have a TCLE as close as possible to the TCLE of the PSE material to avoid temperature stresses in their connection.

The listed requirements are best provided in the typical design of the sleeve holder shown in fig. 1.

Such a sleeve holder consists of the basic sleeve 1 made of stainless steel, which is directly connected to the body of the microcryogenic machine, a bush 2 is connected to the basic sleeve which is made of thin-walled stainless steel to minimize heat flow. End cell 3 of sleeve holder

on which the cooled PSE is directly mounted is a disk made of material with a normalized TCLE value, for example, covar or invar. Shape and

dimensions of sleeve holder can vary depending on the parameters of specific PSE and used microcryogenic machine.
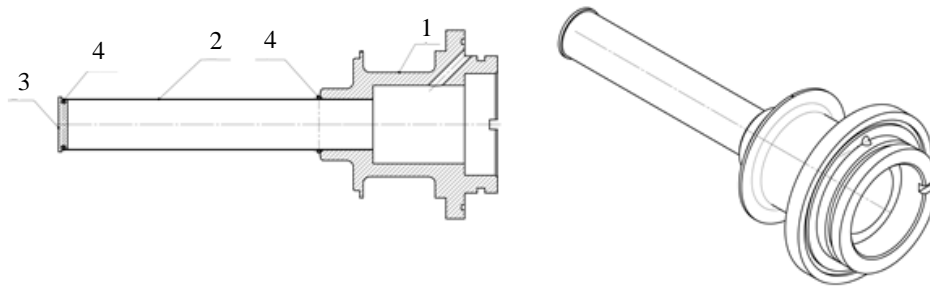
Fig. 1. Design of the sleeve holder: 1 – basic bush; 2 – sleeve; 3 – end cell; 4 – brazing alloy

One of the important technological tasks when manufacturing the sleeve holder is ensuring reliable connection of sleeve holder components to each other which guarantees meeting the conditions of leak-tightness and geometrical stability under cryogenic temperatures. As usual, this can be reached by using welding or soldering. Fig. 1 shows the sleeve holder the components of which are connected by soldering. The locations of alloy brazing are indicated in fig. 1 by pos. 4.

Induction heat is often used in industrial practice to connect metal parts by smoldering [2]; such heat is provided by the occurrence of thermal effect in the connected parts and alloy brazing under the influence of electromagnetic field (Foucault vortex currents).

At the same time, during the heating process, if it is conducted in an air atmosphere, accelerated oxidation of the surfaces of parts and solder invariably occurs, which is not unacceptable for sleeve holder due to the specification of its application, moreover, it can lead to a violation of the tightness of the brazed seam.

Specialists of JSC "SPA "Orion"", as part of solving the problem of manufacturing sleeve holders, tested the creation of vacuum-tight brazed joints by induction brazing which does not lead to oxidation of the connected parts.

Induction heater is used for brazing; its structural diagram is shown in fig. 2.

Connected parts of the sleeve holder 1 and 2 and brazing alloy 3 are placed in the electromagnetic field created by inductor 4. Inductor 4 is connected to the electrical power generator 5 through transformer 6. Inductor 4 together with condenser 7 connected in series to the primary winding of transformer 6 make

oscillation LC-circuit. Depending on the inductance of the coil of inductor 4, condenser 7 capacity, as well as characteristics of the connected parts, the resonant frequency of the LC-circuit may change. This change through the self-excited oscillator 8 keeps the circuit in resonance by changing the frequency depending on the inductance value of the inductor 4. Connected parts 1 and 2 have axially symmetrical shape and are located coaxially to the inductor 4, support 9 contains bearing 10 in which rotary platform 11 is installed, rotation of platform 11 is ensured by drive 12. Seat 13 is installed on platform 11 and it is coaxial to the rotation axis of platform 11. When rotating the connected parts during heating, the installation errors of the connected parts relative to the inductor have a smaller impact on the homogeneity of connection heating.
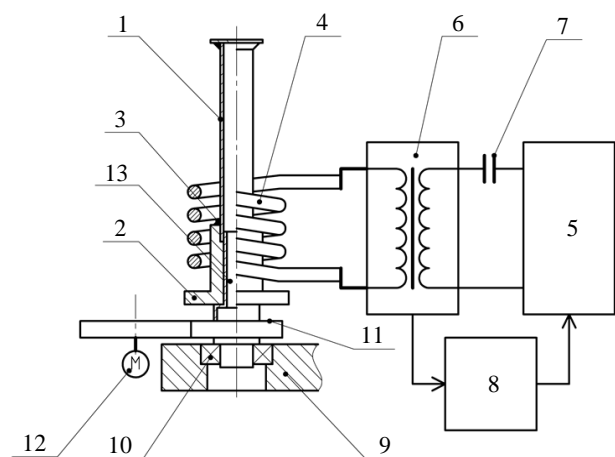
Fig. 2. The diagram of the device for induction brazing of sleeve holders: 1, 2 – components of sleeve holder; 3 – brazing alloy; 4 – inductor; 5 – electrical power generator; 6 – transformer; 7 – condenser; 8 – self-excited oscillator; 9 – support; 10 – bearing unit; 11 – rotary platform; 12 – drive; 13 – seat

The development of induction brazing of sleeve holders was carried out in three main directions:

– obtaining brazed joints under vacuum conditions;

– obtaining brazed joints in the inert gas;

– obtaining brazed joints using protective compounds.

To ensure a vacuum, the inductor and connected parts were placed in a tight chamber from which air was pumped using a high-pressure vacuum pump until reaching residual pressure not exceeding 1×10^{-3} mm Hg. Using a tight chamber also allows to implement the second method by injecting inert gas (for example, argon) in it, replacing air, which allows to create an inert gas environment in the soldering area.

Both in vacuum and inert environment high-quality brazing connections were obtained corresponding to the requirements above. It should be noted that one of the main advantages of soldering under vacuum conditions compared to a gaseous environment is the stable production of brazed joints without voids and cavities which makes the joint vacuum-tight.

However, the use of a tight chamber is unpractical for mass production requiring minimal operating time and minimizing production costs. The thing is that when using a chamber, the access to the connected parts is limited during the soldering process and makes visual inspection over the process more complicated. Moreover, vacuum production or creation of a gaseous environment in the chamber takes significant time and is carried out every time a new set of parts is installed.

One of the solutions to the problem is carrying out induction brazing in the inert gas environment without creating pressurized volume. In this case a setup is used in which inert gas is supplied to the area of brazing joint formation under pressure. With this method, despite the satisfactory quality of the obtained joint and significant reduction in the time of operation, the main disadvantage is the increased consumption of inert gas which makes the process more expensive.

For the mass production of holders, JSC "SPA "Orion" has developed induction brazing in the air environment allowing to ensure high-quality connection and excluding the appearance of oxide film on the surfaces of connected parts. For this purpose, protective compounds are used during brazing which are applied on the surface of parts and prevent oxidation of these surfaces and simultaneously improve the wetting of the molten solder. Soldering fluxes of certain grades can be used as such compounds.

Soldering process with the use of protective compounds is carried out as follows. Before starting soldering, surfaces of parts and solder are covered with flux for protection against environmental influence and improvement of distribution of molten solder. At the same time, unlike the usual practice of using soldering fluxes, the whole surface of parts is covered in flux, not only sections in the soldering area. Connected parts can be manufactured from stainless or covar. At the same time, it is possible to connect parts from different materials. Solder is used for soldering, which melting point is lower than the temperature of high tempering of steels. In case of connection by soldering of parts made from the materials listed above, silver containing solder is used, and as flux – high-temperature soldering flux based on boron acid. Then the connected parts, solder and flux are heated with an inductor at a set speed to a temperature at which flux has the best wetting – ability to maintain contact with a solid surface due to intermolecular force (the practice shows that the temperature is 420 °C when using the flux). The parts are exposed at this temperature and then heated up to the solder melting temperature (for the example considered 595–605 °C). Then the heating is turned off and the parts cool down to room temperature and the residual flux is removed in a weak sodium hydroxide solution.

Due to the induction heating at the junction of soldering parts, the bush surface and holder tube are oxidized which can negatively affect the evacuation of the holder as part of the cryostat. To remove the formed oxide film on the bush surface, washing in a hot aqueous solution of versene is used, the operating principle of which is based on the extraction of cations of insoluble salts that make up the oxide film, in the oxidation degree of +2, +3 and their replacement with sodium cations, practically all salts of which are soluble in water. As versene is not an oxidizing agent, interaction with metal in the zero oxidation

degree does not occur. The complex soluble ferritic salts occurring on the holder's surface are easily removed by flushing in hot water.

The advantage of this method is the possibility of conducting soldering in the open air without using a chamber. This also makes it possible for parts to cool down quicker after heating and shortens the operation time. You can accelerate the cooling process by applying forced air cooling. Due to the convenience of access to the connected parts and inductor, it is possible to ensure a more accurate alignment of parts relative to the inductor.

According to the results of studies and development of the induction brazing method, a patent [4] was obtained for an induction soldering method.

The conducted work allowed to ensure stable mass production of sleeve holders. The appearance of the mass-produced holders is shown in fig. 3.

Fig. 3. Appearance of the mass-produced sleeve holders

One of the most important requirements for sleeve holders is ensuring the brazing joint tightness. Check of tightness is conducted with the use of special a tool shown in fig. 4. The device reproduces the operation conditions of the holder as part of the ISS and vacuum cryostat at elevated helium pressure (20 - 50 kgf/cm^2) inside the sleeve holder. Thus, it is the leakage of helium from the holder that is controlled which is specific to its operation as part of a cryogenic system and not the inleakage into the holder as with the traditional method of inspection using a leak detector.

Fig. 4 shows: the inspected sleeve holder 1 which is tightly connected with body 6 using O-ring 3 (solder wiring is used as sealing material) and flange 8. Through the filling valve 4 in the body 6, sealed with a solder disc, the inner cavity of the sleeve holder is filled with gaseous helium with set overpressure. Next the sleeve holder is aligned with bush 9 through fluorinated rubber O-ring 2. The bush has flanges on both sides, one of which 11 (KF standard) is fixed by clamp 5 on the housing 5 ensuring clamping force from the side of bush 9 on the inspected sleeve holder 1; another flange 7 (KF standard) is similarly connected with a helium leak detector.
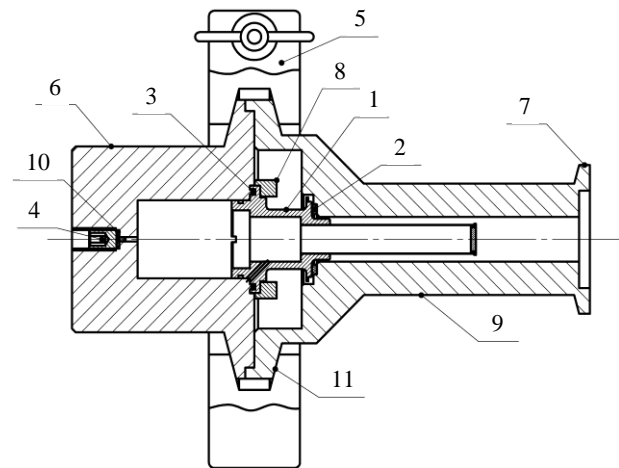
Fig. 4. Design of the device for the tightness test: 1 – inspected sleeve holder; 2, 3 – O-rings; 4 – valve; 5 – clamp; 6 – body; 7 – attachment flange KF; 8 – flange; 9 – bush; 10 – filling hole; 11 – flange KF

Such design allows to search for leaks with greater sensitivity. The registered helium leakage rate is 5×10^{-13} Pa·m^3/s which corresponds to the limit sensitivity of the used helium leak detector.

Conclusions

Results of the conducted studies made it possible to ensure a stable mass production of holders of evacuated cryostatic bodies with high operational specifications. When checking the tightness, it was confirmed that the leakage rate of the gas (helium) from the holder's working cavity is not more than 5×10^{-13} Pa·m^3/s.

REFERENCES

1. Novotelnov V. N. et al., Cryogenic machines. St. Petersburg, Polytechnica, 1991.
2. Vologdin V. V. et al. Induction soldering. Leningrad, Mashinostroenie, 1989.
3. Lashko S. V. and Lashko N. F. Soldering of metals. Moscow, Mashinostroenie, 1988.
4. Bannikov M. V., Korotaev E. D. and Sharov A. A. Induction soldering method. Patent RU 2824969. 2024.

About authors

Korotaev Evgenii Dmitrievich, Engineer Cat. 1, RD&P Center Orion, JSC (111538, Russia, Moscow, Kosinskaya st., 9). E-mail: korotaevrus@gmail.com SPIN code: 7229-7672

Guryev Dmitry Igorevich, design engineer cat. 2, RD&P Center Orion, JSC (111538, Russia, Moscow, Kosinskaya st., 9). E-mail: ptokrs@mail.ru

Guryev Andrej Igorevich, testing engineer, RD&P Center Orion, JSC (111538, Russia, Moscow, Kosinskaya st., 9). E-mail: wwwesche@gmail.com

Zinkovsky Alexander Aleksandrovich, Head of the Center of engineering support and development of technology, RD&P Center Orion, JSC (111538, Russia, Moscow, Kosinskaya st., 9). E-mail: Rabota2114@yandex.ru

Morozov Dmitry Igorevich, process engineer cat. 1, RD&P Center Orion, JSC (111538, Russia, Moscow, Kosinskaya st., 9). E-mail: morozovdi1995@mail.ru

Sharov Alexander Aleksandrovich, Ph.D. of Technical Sciences, Deputy Head of the Center of Microphotoelectronics RD&P Center Orion, JSC (111538, Russia, Moscow, Kosinskaya st., 9). Moscow State University of Geodesy and Cartography (105064, Russia, Moscow, Gorokhovsky lane 4).

Experimental and numerical study of cooling efficiency of a channel cooling with EHD flows

V. V. Voevodin[1,2,*], Ya. E. Zharkov[1], A. S. Kirillov[1], O. I. Korzhova[1], S. I. Moshkunov[1] and V. U. Khomich[1]

[1] *Institute for Electrophysics and Electric Power of the Russian Academy of Sciences,*
St. Petersburg, 191181 Russia
[*] *E-mail: vvvoevodin@ieeras.ru*
[2] *Kutateladze Institute of Thermophysics of the Siberian Branch of the Russian Academy of Sciences,*
Novosibirsk, 630090 Russia

A combined numerical and experimental study was conducted on a model channel cooling system utilizing forced air convection and auxiliary electrohydrodynamic (EHD) flows generated by a corona discharge. Geometric parameters of the channel and the power supplied to the devices generating the cooling flows were varied. For the given conditions, the range of effective use of EHD flows was demonstrated, and a non-linear relationship between the channel wall temperature and the power of the corona discharge generating the EHD flow was revealed.

Introduction

The current trend in electrical engineering development is characterized by a steady growth of the speed of electronic components and their constant miniaturization. This inevitably leads to a significant rise in the heat release rate from the surfaces of active elements. A wide range of cooling systems (CS) are currently used for heat removal: those based on calorimetric and thermoelectric effects, those utilizing heat and mass transfer via electrohydrodynamic (EHD) flow, liquid-based systems, etc. [1, 2]. A typical feature of many forced convection cooling systems is the use of channels through which cooling gas is pumped. To control the flow in the channel and create mixing disturbances to intensify heat exchange between heated surfaces and gas, special inserts in the flow [3] can be used, which, however, add to the aerodynamic resistance. In recent years, researchers have been

focusing on the possibility of using so-called "electric wind" or electrohydrodynamic flow as a secondary flow generator [4–6]. The EHD flow is generated in the gas discharge and is caused by collisions of formed charged particles with gas molecules in a strong electric field. Advantages of its use include the absence of moving mechanical parts, relatively low aerodynamic resistance of the electrodes creating the discharge, and the possibility of creating distributed cooling systems with randomly shaped electrodes that can be integrated into hard-to-reach areas of a cooling system. Their exploitability as part of CSs has been repeatedly demonstrated both by experiments in open air [7] and by simulating in variously shaped channels [8, 9]. At the same time, there is few experimental data on the operation of the combined CS of this kind in the available literature.

The aim of this work was to experimentally investigate the effectiveness of cooling heat-

loaded elements in a channel using both an independent EHD flow generated by a corona discharge (CD) and in combination with forced convection created by a fan.

Setup Description

A structure representing a horizontal channel assembled of ABS plastic (Fig. 1) was used as a model cooling system. The structure's dimensions were $115 \times 55 \times 2d$ mm³, where d is the distance from the plates to the mounting points of electrode for creating EHD flows. Forced convection in the channel was created by a centrifugal fan through a designed power-controlled laminarization unit (0.3–1.2 W; 1–3 m/s in the channel, gas flow rate m = 0–2 g/s). The inner walls of the channel were made of grounded, thermally insulated plates made of polished aluminum. The plates was heated from their ends using film ceramic resistors, with the heating power varying from 10 to 30 W. Temperature of the plates was monitored with type K thermocouples attached at their centers and connected to CENTER 303 instrument (accuracy ± 0.7 °C).

To generate the EHD flow, copper wires with a diameter of 50 μm were stretched transversely in the middle of the channel. These wires were connected to stabilized negative-polarity high-voltage DC power supply Spellman SL20*2000, with the current in its circuit measured with Fluke 17B+ multimeter, which allowed for estimating the average CD power P_{CD}. The wire-to-plate distance (d) and wire-to-wire distance (L) could be varied in the range of 6–10 mm.

The fan and heating resistors were powered from stabilized, controlled DC power supplies. Heating power was adjusted to maintain temperature of $T_0 = 100$ °C at the plate center under conditions of natural convection without EHD flow. The temperature of the air injected into the channel was 22 °C with 40 % humidity.

As part of the experiments, the temperature drop relative to steady-state values, $\Delta T_{CD} = T_{vent} - T_{comb}$, was recorded. It was defined as the difference between the plate temperature under forced convection, T_{vent}, and under its combination with EHD flow, T_{comb}. Values were read off at various combinations of corona discharge power P_{CD}, fan flow rate m, and different channel widths d. To determine the effectiveness of EHD flow application, the ratio of the temperature drop to the consumed CD electrical power, $\Delta T_{CD}/P_{CD}$, was calculated.
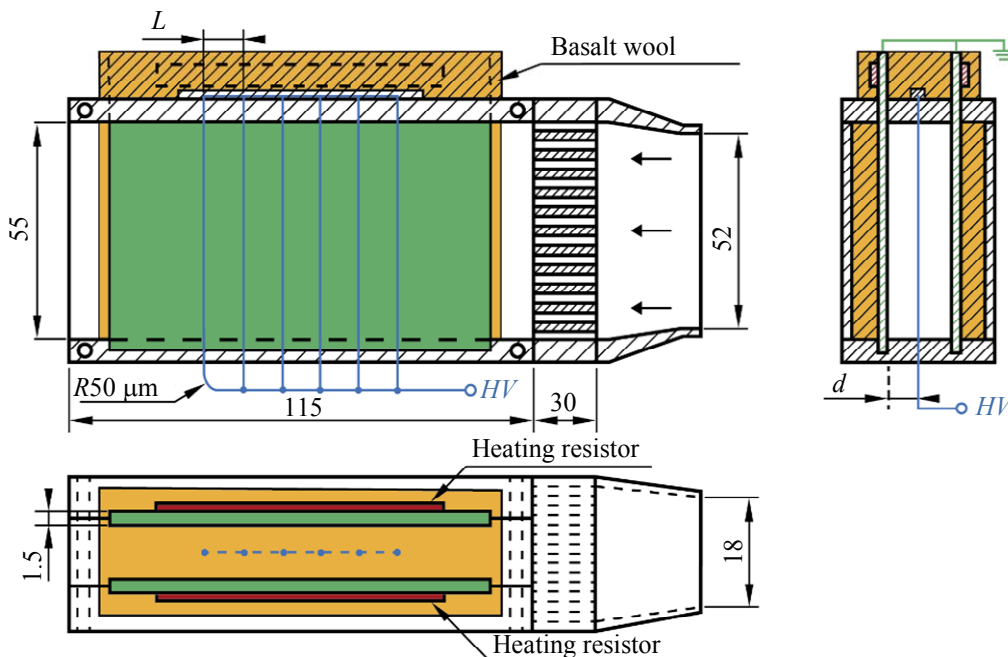
Fig. 1. Schematic of the experimental cooling channel featuring forced convection (shown with arrows) and the capability for generating EHD flows (heating resistors shown in red, plate anodes in green, wire cathodes in blue)

Mathematical Model and Calculation Results

To explain the obtained results, a channel model featuring the geometry similar to that used in the experiment was built using the finite element numerical simulation software package. The model implements an iterative coupled calculation of CD and thermal hydrodynamic field in air. On each iteration, the gas dynamics problem is first solved using the RANS approximation with the $k-\omega$ turbulence model [10] and accounting for convective heat transfer between solid and gas domains. Then the distribution of electric potential (Poisson's equation) and space charge density (convection-diffusion equation for a single carrier type) is calculated, based on the obtained temperature and velocity fields. Charge injection on conductor surfaces is enabled when the local electric field strength exceeds the ignition threshold determined by Peek's formula [11] and is implemented via a weak form of the boundary value. To stabilize the iterative process, the field exceedance is filtered similarly to the *RC* circuit, which suppresses oscillations when this threshold is crossed. The resulting distribution of volumetric charge and electric field is used to calculate the electrodynamic force, which is introduced into the motion equation as a volumetric source in the next iteration, thus ensuring a self-consistent solution.

The simulation model shown as a diagram in Fig. 2 is a two-dimensional geometry comprising an air channel and an adjacent heated aluminum plate. To reduce computational complexity, the problem was solved in the middle of the symmetric system using a symmetry condition along the channel's central axis. At the inlet boundary, the gas mass flow rate $\dot{m}$ was specified, which was determined according to the characteristic of the fan used, with its constant temperature equaling to 293 K. At the system outlet named as "Sink", the zero static pressure and a heat loss condition were set. Within the solid domain (the aluminum plate), the heat conduction equation was solved considering the total applied heating power P_{heat}. Thermal insulation condition was applied to all external surfaces of the plate, including sections outside the channel. Hydrodynamic boundary values on all solid walls were defined as no-slip conditions using a low-Reynolds-number approximation, thus ensuring proper resolution of the viscous sublayer. Potential $\phi = V_{var}$ on the conductors was varied to achieve the specified CD power in the system in correspondence with the one obtained in the experiment. Charge injection on the wire surfaces was enabled when the local electric field strength reached the threshold value determined by Peek's formula using parameters $E_0 = 30$ kV/cm and $\gamma = 0.03$ [11].
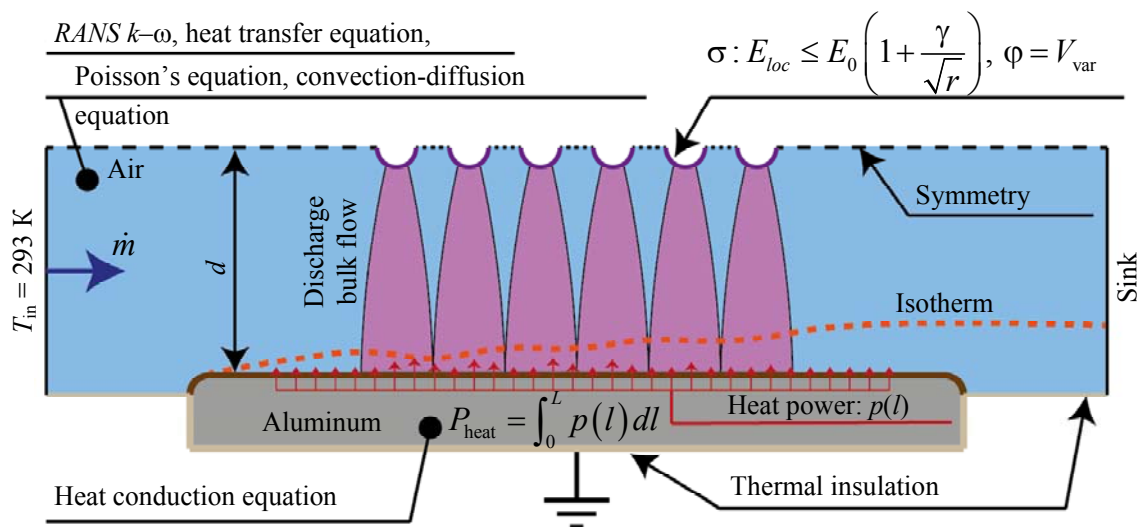

Fig. 2. *Scheme of the computational domain with the air channel, heated aluminum plate, and the system of corona electrodes*

Key results of the parametric study are shown in Fig. 3. The increase in the additional cooling temperature ΔT_{CD} as a function of corona discharge power is shown to correspond to a squared relationship, which is consistent with the current-voltage characteristic of the discharge recorded during the experiment.
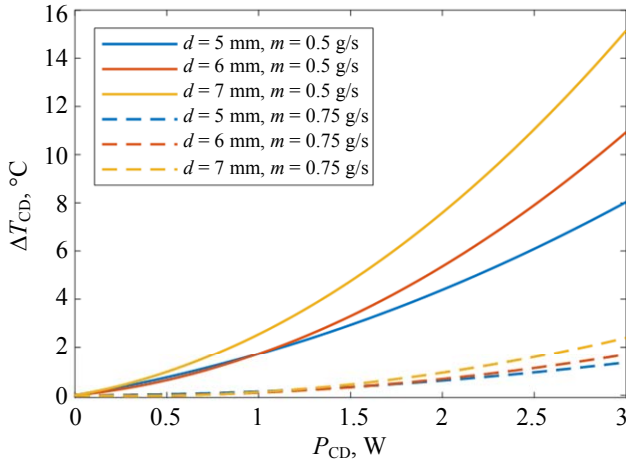

Fig. 3. Calculated curve of temperature drop ΔT_{CD} of the cooled plates vs. corona discharge power for various channel widths d and volumetric flow rates m.

As can be seen from the curves in Fig. 3, the flow velocity is the determining parameter. At a mass flow rate of 0.75 g/s, the energy contribution of bulk forces to the total power of mass transfer is insufficient to have a significant influence on the temperature distribution, and the magnitude of ΔT_{CD} remains relatively small. In the case of a lower flow rate equaling to 0.5 g/s, a pronounced increase in additional cooling (rise of ΔT_{CD}) is observed for all investigated distances between the wire and the aluminum plate (5, 6, and 7 mm): as the gap increases, the channel expands, the average velocity decreases, and cooling efficiency grows.

The spatial distributions of temperature and velocity fields derived from the calculation also showed that, within the parameter range under consideration, the "*blocking effect*" [4] is practically absent: the vortex structures formed by the discharge do not lead to noticeable disruption of the through-flow.

Experimental Results

Figure 4*a* shows the curve of steady-state temperature drop ΔT_{CD} after corona discharge ignition vs. its power P_{CD} for the fixed fan volumetric flow rate $m = 0.8$ g/s. It can be noted that the EHD flow demonstrates the highest efficiency in the range of low CD power values (up to 0.5 W) under the studied conditions, which is consistent with the calculated results. Subsequently, the temperature drop changes over to saturation, and increasing the CD power become impractical.

The maximum ratio of the temperature drop achieved during cooling by the EHD flow to the power consumed for its generation, calculated across the entire dataset for different forced convection flow rates m and channel widths d (Fig. 4*b*), supports the conclusions about the necessity of ensuring that EHD flow bulk forces are sufficient to change heat and mass transfer processes near heated surfaces, which will intensify heat exchange most effectively. At the air flow rate around 0.8 g/s, it is possible to achieve a temperature reduction of 30-40 °C per 1 W of electrical power input into CD.

However, several contradictions can be found in the simulation results. Channel width d has a relatively weak and non-systematic influence on the ΔT_{CD} values recorded during the experiments at fixed air flow rates m. Furthermore, the saturation effect of ΔT_{CD} is not reproduced in the calculations, with P_{CD} increasing. It can be assumed that this may be related to both gas heating by intense CD [12] and development of conditions for the formation of stagnant zones near heated surfaces [4]. This calls for a more detailed reproduction of the channel's geometric features, operation of the pressure fan, and CD burning conditions.
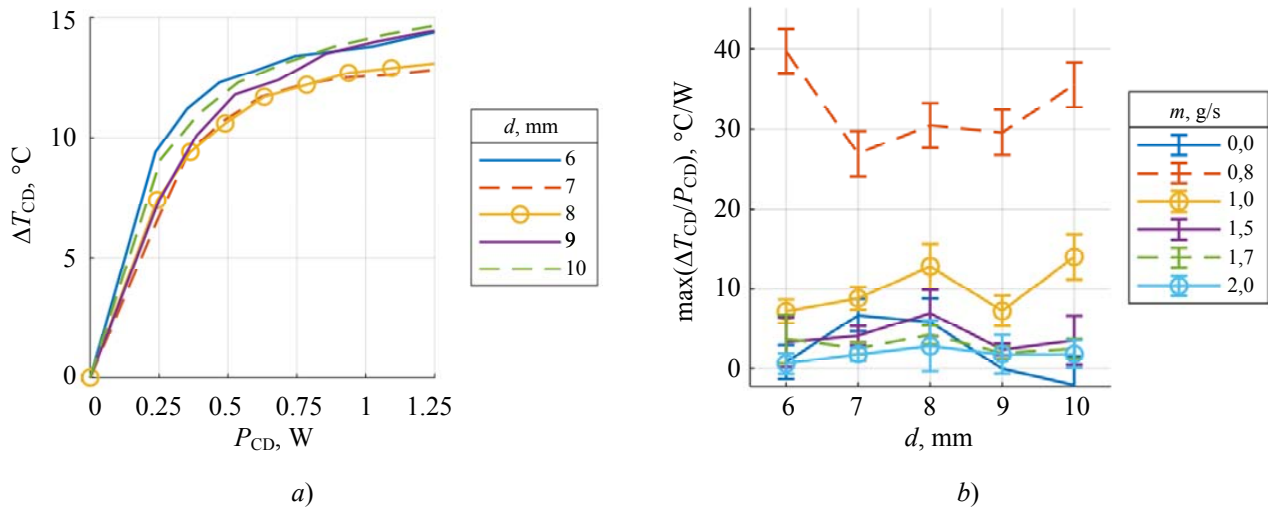
Fig. 4. Temperature drop ΔT_CD vs. CD power P_CD for various channel widths d at fixed fan flow rate m = 0.8 g/s (a) and maximum ΔT_CD/P_CD ratio at various d and m (b)

Conclusions

The study performed to calculate the effectiveness of cooling using EHD flows in a rectangular channel with forced air convection has shown that the application of EHD flows is energy-efficient provided that the energy contribution of the generated bulk forces is sufficient to modify the main flow. Experimental results revealed a complex dependence of the channel wall temperature reduction on the channel's geometric parameters and EHD flow power, which may be related to air heating processes within the discharge or development of a "blocking effect". The obtained data will be used for further development of a combined cooling device utilizing EHD flows.

REFERENCES

1. Maria C. et al., Applied Thermal Engineering **227**, 120427 (2023).
2. Iranshahi K. et al., International Journal of Heat and Mass Transfer **232**, 125895 (2024).
3. Jadhao R. R., Chitragar P. and Kamble D., Physica Scripta **100** (3), 32002 (2025).
4. Wang Y. B. et al., Physics of Fluids **35** (11), [article number] (2023).
5. Khomich V. Yu. and Yamshchikov V. A., Uspekhi Fizicheskikh Nauk **187** (6), 653–666 (2017).
6. Moshkunov S. I. et al., Applied Physics, № 6, 32–38 (2011) [in Russian].
7. Voevodin V. V. et al. In Proceedings of the XII All-Russian Conference with International Participation "Fuel Combustion: Theory, Experiment, Applications", Novosibirsk, 2024, pp. 25.
8. Ming G. et al., International Communications in Heat and Mass Transfer **153**, 107344 (2024).
9. Reza B. L. and Majid M., Journal of Electrostatics **70** (1), 31–42 (2012).
10. Wilcox D. C. Turbulence Modeling for CFD. La Cañada, DCW Industries 1998.
11. Peek F. W. Jr. Dielectric Phenomena in High Voltage Engineering. New York, McGraw-Hill Book Company, inc., 1915.
12. Jones J. E., Journal of Electrostatics **66** (1–2), 84–93 (2008).

About authors

Voevodin Vadim Vadimovich, Cand. Sci. (Eng.), Senior Research Scientist Institute for Electrophysics and Electric Power of the Russian Academy of Sciences (191181, Russia, Saint Petersburg, 18 Dvortsovaya Emb., Letter A); Kutateladze Institute of Thermophysics of the Siberian Branch of the Russian Academy of Sciences (630090, Russia, Novosibirsk, 1 Academician Lavrentiev Avenue,). E-mail: vvvoevodin@ieeras.ru SPIN code: 1049-1177, AuthorID: 1013023

Zharkov Yaroslav Evgenievich, Research Scientist Institute for Electrophysics and Electric Power of the Russian Academy of Sciences (191181, Russia, Saint Petersburg, 18 Dvortsovaya Emb., Letter A). E-mail: yarik77794@mail.ru SPIN code: 1619-1493, AuthorID: 1142014

Kirillov Alexander Sergeyevich, Junior Research Scientist Institute for Electrophysics and Electric Power of the Russian Academy of Sciences (191181, Russia, Saint Petersburg, 18 Dvortsovaya Emb., Letter A). E-mail: caduceus.kas@gmail.com SPIN code: 3924-1556, AuthorID: 1193477

Korzhova Olga Igorevna, Junior Research Scientist Institute for Electrophysics and Electric Power of the Russian Academy of Sciences (191181, Russia, Saint Petersburg, 18 Dvortsovaya Emb., Letter A). E-mail: oikorzhova@ieeras.ru SPIN code: 1627-1919, AuthorID: 1260716

Moshkunov Sergey Igorevich, Dr. Sci. (Eng.), Corresponding Member of the Russian Academy of Sciences, Head of the Research Direction "Pulse Technology and Electrophysics Institute for Electrophysics and Electric Power of the Russian Academy of Sciences (191181, Russia, Saint Petersburg, 18 Dvortsovaya Emb., Letter A). E-mail: serg-moshkunov@yandex.ru SPIN code: 4103-8401, AuthorID: 161510

Khomich Vladislav Yuryevich, Dr. Sci. (Phys.-Math.), Academician of the Russian Academy of Sciences, Scientific Supervisor Institute for Electrophysics and Electric Power of the Russian Academy of Sciences (191181, Russia, Saint Petersburg, 18 Dvortsovaya Emb., Letter A). E-mail: khomich@ras.ru SPIN code: 6924-8941, AuthorID: 167051

========== PHYSICAL EQUIPMENT AND ITS ELEMENTS ==========

Optical-acoustic radiation receivers with a freely suspended membrane

P. E. Kotlyar

Institute of Automation and Electrometry of the Siberian Branch of the Russian Academy of Science,
Novosibirsk, 630090 Russia
E-mail: kotlyarpe@iae.nsk.su

The evolution of the main unit of an optical-acoustic pressure transducer-sensor is considered. A consistent transition from a membrane pressure sensor with rigid fixation of the membrane along the contour, leading to uncontrolled mechanical stresses and changes in the main metrological parameters to cantilever pressure sensors in which only one side is fixed, which leads to an increase in sensitivity by more than 140 times, is shown. It is shown that by chemical etching of four L-shaped narrow through grooves on a membrane foil in one technological cycle, a four-point Z-shaped skew-symmetric suspension can be formed, containing a completely deformation-free central membrane element of a square shape, a four-point angular elastic suspension in the form of four narrow elastic sensor elements located along the lateral sides of the non-deformable membrane element and rigidly fixed to the support contour, and a support contour.

Introduction

Membrane pressure transmitters are among the critical structural elements of opto-acoustic radiation detectors and determine metrological characteristics of the device to a significant extent [1, 2]. Operating principle of **membrane pressure transmitters** is based on deformation of the elastic membrane, which responds to changes of external pressure. A capacitive membrane transmitter is capable of measuring a pressure very accurately over a range of 3.5 to 4 orders of magnitude, with the lower limit down to 10^{-5} mbar and accuracy of $\pm (0.15\text{–}0.35)$. Readings of a capacitive membrane transmitter do not depend on the type of gas filling the expansion and compensation chambers. Developed by Knowles (Illinois, USA) using the in-house CMOS/MEMS technology platform launched in 2002, SiSonic™ series silicon-based microphones are now in their fourth generation and are sold worldwide in the amounts exceeding 1 billion pieces per year.

Membranes

The sensitivity of an opto-acoustic detector (OAD) is defined as the minimum radiation power at the input that allows for reliable signal extraction at the background level and the converter's inherent noise. It can be calculated as the product of partial sensitivities of photothermal (S_{I-T}), thermoacoustic (S_{T-P}), acoustomechanical ($S_{P-\delta}$), and electromechanical ($S_{\delta-U}$) conversion stages:

$$S_{\text{OAП}} = S_{I\text{-}T} S_{T\text{-}P} S_{P-\delta} S_{\delta-U} = \frac{\Delta T}{\Delta I} \frac{\Delta P}{\Delta T} \frac{\Delta \delta}{\Delta P} \frac{\Delta U}{\Delta \delta}.$$

Theoretical and experimental studies have shown that the limiting stage in the conversion chain is acoustomechanical stage $S_{P-\delta}$ implemented as a pressure transmitter.

Sensitivity δ (deflection magnitude at the center of a flat membrane rigidly fixed along its contour) for small displacements under pressure P is expressed by formula [3]:

$$\delta = \frac{3\left(1-\mu^2\right)PR^4}{16Rh^3},$$

where R is the membrane's working radius (along the fixation contour); h is the membrane thickness; E, μ are the Young's modulus and Poisson's ratio of the membrane material, respectively. In existing OAD designs, membrane deflections at the threshold values of the measured radiation fluxes amount to a few angstroms.

Physico-mechanical properties of membranes depend strongly on the material, structure, surface properties, and technology. It can be derived from the given expression that the membrane transducer sensitivity is determined by the physical properties of the membrane material (E, μ) and design parameters (R, h). Superlinear dependencies of sensitivity on R^4, h^3 cause the supersensitivity of membrane sensors to changes in device parameters, which is a difficult to handle when designing large-dimensional matrix devices.

Membrane Manufacturing Material

Designs have been evolving by changing sequentially from metallic membranes made of duralumin, silver, nickel, titanium, and titanium alloys VT16 or VT35 with thicknesses of 40-100 nm, to bimorph polymer membranes coated with a reflective silver or antimony layer approximately 100 A thick [4]. Membrane devices designed using MEMS technologies and widely employed for microminiaturization are usually made of: silicon Si membrane which is formed by etching a substrate down to thicknesses of 2-5 µm; silicon dioxide SiO_2, silicon nitride Si_3N_4, silicon carbide SiC, carbon C, aluminum nitride AlN, boron nitride BN produced both from the gas phase and by ion-chemical deposition methods. Silicon nitride (Si_3N_4) is used as the base material for ultrathin membranes since it is one of the primary materials in microelectronics with a well-established fabrication technology and known properties [5, 6].

Promising materials for creating membranes are kapton and graphene. Kapton is a polyimide filmused in various space tools

developed byDuPont in the 1960s . Kapton is an elastic dielectric, which is stable over a wide temperature range from −273 to +400 °C, which allows handling the embrittlement in metal and polymer membranes at low temperatures. It is used for manufacturing flexible printed circuit boards and outer layers of spacesuits [7].

Graphene The known works on designing a new generation of opto-acoustic transducers [8, 9] attribute the choice of single-layer graphene (SLG) for fabricating a flexible membrane to such main factors as the extremely small thickness and extremely high elasticity and mechanical strength of the material, which guaranteed a significant increase of sensitivity. Additionally, the use of single-layer graphene membranes allows not only to achieve the record-breaking sensitivity enhancement but also to almost entirely eliminate such traditional drawbacks of transducers as high susceptibility to acoustic and vibrational noise, while ensuring increased response speed, expanded dynamic range, and ability to operate not only at room temperatures but also under extreme deep cooling.

Numerous experiments on selecting membrane shapes were aimed not at increasing sensitivity, but primarily at obtaining the required frequency response.

The study of the possibilities of enhancing the sensitivity of opto-acoustic transducers with membranes of various geometric shapes (square, circular, and rectangular) rigidly fixed along the perimeter has revealed that the use of a circular membrane provides the maximum change in the sensing element's capacitance under pressure as compared to those of sensing elements with membranes of other geometric shapes [10].

The technological challenges, which have not been fully resolved to date, are related to poor control of mechanical stresses from the rigid fixation of membranes and to the difficult control of the etching thickness of ultrathin (about 1 µm or less) membranes in MEMS technologies, which calls for individual calibration of pressure transducers.

Cantilever

A thin reflective film rigidly fixed on one side in a conventional photoacoustic cell used instead of a classical flexible membrane was first

proposed in the paper by de Paula [11]. An elastic cantilever, as a precision micro-dynamometer with a threshold of 1 piconewton, was first used in an atomic force microscope in 1982.

A cantilever is a thin, elastic U-shaped plate of length α, width b ($b < \alpha$), and thickness h ($h \ll \alpha$, b), which is rigidly fixed along the narrow side b. The geometry of the cantilever determines its stiffness varying over a wide range. The cantilever's stiffness coefficient $K = Ebh^3/4\alpha^3$, where E is the Young's modulus of the cantilever material, b is the width, h is the thickness, and a is the length of the rectangular cantilever. The cantilever's stiffness coefficient, which largely determines the sensitivity of the device, can vary over a very wide range ($10^{-4} \div 10$ N/m).

The main property of a cantilever is its deflection under the action of an applied force. Its main characteristic is its elastic constant. The sensing element of the cantilever-type pressure transmitter of the opto-acoustic detector (OAD) shown in Fig. 1 is structurally different from the cantilevers used in atomic force microscopy [12]. It consists of a substrate that completely covers the acoustic aperture of OAD housing a movable cantilever element separated from the substrate on three sides by a narrow through micro-groove several micrometers wide. A reflective coating (platinum, gold, aluminum) is applied on the cantilever side facing the compensation chamber for the optical readout system.
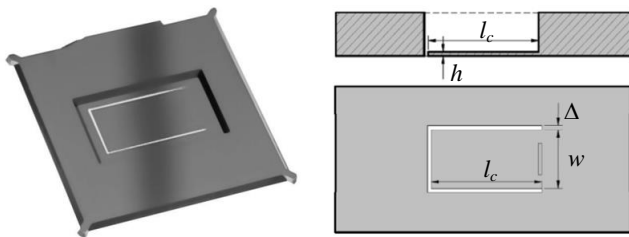

Fig. 1. Photo and schematic diagram of the OAD cantilever as per [13]

The relationship between cantilever's deflection δ and applied stress P is determined by Stoney's formula: $\delta = \dfrac{3P(1-\mu)}{E}\left(\dfrac{L_C}{h}\right)^2$, where E, μ are the Young's modulus and Poisson's ratio of the cantilever material, respectively; L_C is the beam length; h is the cantilever beam thickness.

Cantilever's stiffness is defined by expression $k = \dfrac{Ewh^3}{4L_C^3}$, where w is the cantilever's width.

The maximum deflection of such beam under uniformly distributed load $\delta_{max} = \dfrac{PL_C^4}{8EI}$ and maximum deflection angle $\theta_{max} = \dfrac{PL_C^3}{6EI}$ where I is the moment of inertia $I = \dfrac{wh^3}{12}$. Then

$$\delta_{max} = \frac{3PL_C^4}{2Ewh^3} \text{ and } \theta_{max} = \frac{2PL_C^3}{Ewh^3}.$$

Cantilever's deflection $\delta_L = \dfrac{PL^2}{12EI} +$

$$+\left[2L_cL - 3L_c^2 - \frac{L^2}{2}\right].$$

The theoretical assessment of the sensitivity of a classical rigidly-fixed circular membrane and a rectangular cantilever of equal area showed that the deflection of the cantilever's free end exceeds that of the circular membrane's center by 140.6 times [13]. Experimental studies [14] demonstrated for cells with a simple microphone, a differential microphone, and a cantilever pressure transmitter, with deflections measured using a laser interferometer, that their sensitivity values were 3.1×10^{-7}, 1.7×10^{-7} and 2.2×10^{-9} cm^{-1}·W·Hz$^{1/2}$, respectively, which is in good agreement with the theoretical estimate.

Cantilever's stiffness $k = \dfrac{Ewh^3}{4L_C^3}$ is typically 2 to 3 orders of magnitude lower than that of the membrane, and displacement of the cantilever's end can reach tens of micrometers without any nonlinear or limiting effects. This significant increase in sensitivity is due to the fundamental difference in the behavior of plates (where bending deformations prevail) as compared to membranes (where tensile deformations prevail) in case of linear and nonlinear deformations.

Currently, the research groups of Stanford University are the leaders in development of cantilever-type micromechanical devices. They have designed cantilevers with a stiffness of 10^{-5} N/m capable of detecting forces as low as 10^{-18} N, and cantilevers with a mechanical

response time of 90 ns [15].

For the purpose of calculation [16], the cantilever is considered a rigidly-fixed beam with structural length L_C, width w, and thickness h loaded by uniformly distributed load P (see Fig. 2).
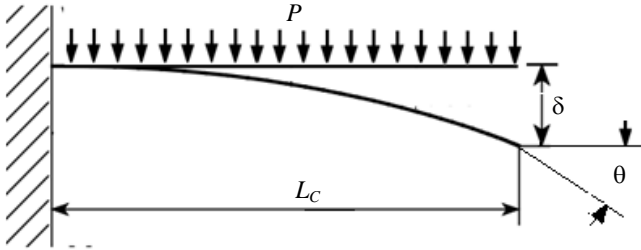
Fig. 2. Calculation diagram for the cantilever beam under uniformly distributed load

Free-Suspended Membrane

To overcome the main disadvantage of classical membrane pressure transmitters, that is uncontrolled mechanical stresses arising in the membrane due to its rigid fixation, and to increase the sensitivity and expand the dynamic range, a precision pressure transmitter for OAD has been proposed. This transmitter is based on a square conductive membrane element freely suspended at four points using elastic sensing elements, which are rigidly fixed to a support frame with a capacitance displacement sensor for the membrane element.
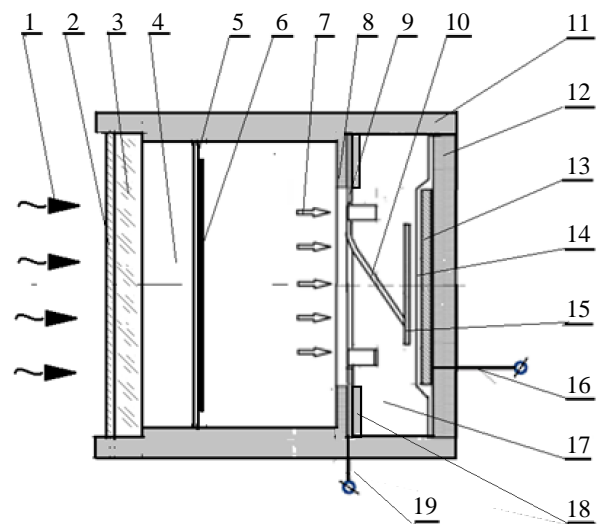
The structural diagram of the opto-acoustic detector of infrared and THz radiation with a free-suspended membrane is shown in Fig. 3. It comprises a cylindrical housing containing a system of an expansion chamber and a compensation chamber that are pneumatically connected and filled with helium at low pressure. One end of the expansion chamber serves as an input window with an anti-reflection coating. Inside the expansion chamber, parallel to the input window, is a collodion film with a metal absorbing element in the form of a thin metallic film deposited on it and thermally isolated from the expansion chamber walls. The expansion chamber is separated from the compensation chamber by a dividing partition, which is a disc-shaped thin elastic plate of conductive material secured between a support washer and a clamping washer. The diameter of the dividing partition is equal to the inner diameter of the compensation chamber. Four through-etched lines, each

3–30 μm wide, are made on the dividing partition (Fig. 4) using the precision photolithography technology. Each line consists of two orthogonal, equal-length segments of length a. The first segment starts at distance b from the corner of the central square ($a \times a$) and is oriented along the square side. The second segment is made at a 90° angle to the first and runs parallel to the square side with an offset equaling to $b + \Delta$, where Δ is the width of the gap formed by the through etching. This process forms:

– non-deformable membrane element 15 of the square shape ($a \times a$), with side $a = 0.6D$, located at the center of dividing partition 9 and covering most of the acoustic aperture and is capable of moving translationally along an axis perpendicular to its plane under the pressure of the expanding gas.

– a four-point corner elastic suspension in the form of four narrow ($a \times b$) elastic sensing elements 10 positioned along the lateral sides of non-deformable square membrane element 15 and rigidly fixed to the support frame;

– support frame 9 representing the peripheral part of the dividing partition secured with clamping washer 18.

Fig. 3. Structural diagram of the opto-acoustic receiver of infrared and THz radiation with a free-suspended membrane: 1 – input radiation; 2 – anti-reflection coating; 3 – input window; 4 – expansion chamber; 5 – film with through porosity; 6 – metal absorbing element; 7 – pressure wave; 8 – washer-shaped partition; 9 – support frame; 10 – elastic sensing element; 11 – cylindrical housing; 12 – rear wall of the compensation chamber; 13 – fixed electrode of the dynamic capacitor; 14 – protective dielectric coating; 15 – non-deformable square membrane element; 16 – fixed electrode terminal;

17 – compensation chamber; 18 – clamping washer; 19 – dividing partition terminal
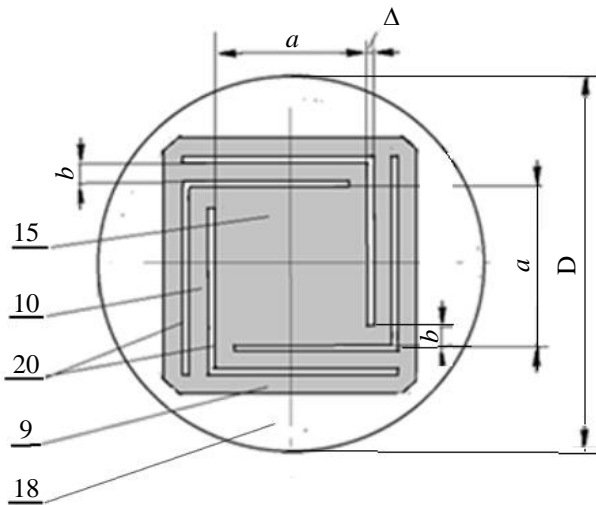
Fig. 4. Structural diagram of the sensitive element of the pressure transmitter with a free-suspended membrane element, where 9 – support frame of the sensitive element, 10 – elastic sensing beam, 15 – non-deformable square membrane element, 18 – clamping washer, 20 – through-etched line

Under the pressure of the expanding gas, each of four sensing elements 10 will experience bending deformations caused by: distributed load: $\delta_{distr.} = qa^4/8EI$, where $\delta_{distr.}$ is the sensing element's deflection; q is the specific pressure; a is the sensing element's length; E is the elastic modulus of material; I is the moment of inertia of the rectangular cross-sectional area of the sensing element $I = bh^3/12$, and concentrated load caused by pressure P on one quarter of membrane element's area $\delta_{cocp} = QEI\dfrac{a^3}{3}$, where $Q = 0.75Pa^2/4$ and $h_{conc.} = 075Pa^5/Ebh^3$.

The total displacement of the corner of non-deformable membrane element 15 will be $\delta = \delta_{distr.} + \delta_{conc}$. With sensing elements being completely identical, this ensures the translational movement of non-deformable square membrane element 15, which serves as a traveling electrode in the capacitance pressure transmitter.

The sensitivity of such pressure transmitter is determined by sensing elements' width b, where $b = (0.1–0.05)a$, and dividing partition

thickness h, which is equal to several micrometers.

Expansion chamber 4 and compensation chamber 17 become pneumatically connected through the gaps of the through-etched lines in the dividing partition. This provides pneumatic feedback between the chambers similarly to a capillary channel in the classical OAD scheme, and eliminates the stiffness increase due to gas compression in compensation chamber 17.

Conclusion

The proposed free-suspended membrane forms a third group of sensing elements for opto-acoustic detectors (OAD) (membrane, cantilever, free suspension). A similar free suspension is known as a 4-point Z-shaped skew-symmetric suspension for axial accelerometers [17]; however, it has not been considered as a membrane suspension for pressure transmitters in the known literature. This suspension provides the sensitivity increased by more than three orders of magnitude as compared to a circular membrane made of the same material and having the same thickness and active area. The translational movement of the freely suspended conductive membrane element ensures the effective conversion of pressure changes in the expansion chamber into capacitance changes. If a dashed reflective mask is applied on the membrane element surface, the suspension, due to its rotational motion, simultaneously allows for optical readout of the displacement using the Toepler "schlieren" technique.

REFERENCES

1. Gibin I. S. and Kotlyar P. E., Applied Physics, № 2, 90–97 (2020) [in Russian].
2. Kotlyar P. E. and Potaturkin O. I., Avtometriya, № 3, 77–95 (2025).
3. Andreyeva L. Ye. Uprugiye elementy priborov. Moscow, Mashinostroyeniye, 1981, p. 463.

4. Hasikin K., Soin N. and Ibrahim F. Proc. of the IEEE Int. Conference on Semiconductor Electronics. Malacca, Malaysia, 2010, pp. 293–296.

5. Palatnik L. S. and Il'inskiy A. I., UFN **95** (4), 613–645 (1968).

6. Dedkova A. A. et al., Zhurnal tekhnicheskoy fiziki **91** (10), 1054–1465 (2021).

7. Poliimidnyye plenki DuPont™ Kapton®. www.dupont.com. 03.04.2023.

8. Baglioni G. et al., Nanoscale **15**, 6343–6352 (2023).

9. Fan K., Suen J. Y. and Padilla W. J., Opt. Express **25** (21), 25318–25325 (2017).

10. Tun P'o Vin., Simonov B. M. and Timoshenkov S. P., Izvestiya vuzov. Elektronika **28** (2), 222–231 (2023).

11. de Paula M. H. et al., J. Appl. Phys. **64**, 3722–3724 (1988).

12. Getmanenko N. Yu., Vostochno-Yevropeyskiy zhurnal peredovykh tekhnologiy **4/7** (52), 30–35 (2011).

13. Mikko Saarinen. Cantilever enhanced gas sensing using photoacoustic spectroscopy. Finland, Aalto university school of science and technology, 2010, p. 83.

14. Lindley R. E. et al., Applied Physics B **86**, 707–713 (2007).

15. Bykov A. V., Izvestiya Yuzhnogo federal'nogo universiteta. Tekhnicheskiye nauki, 141–151 (2014).

16. Feodos'yev V. I. Izbrannye zadachi i voprosy po soprotivleniyu materialov. Moscow, Nauka, 1967.

17. Raspopov V. Y. Mikromekhanicheskiye pribory. Moscow, Mashinostroyeniye, 2007.

About the author

Kotlyar Pyotr Efimovich, Doctor of Geological and Mineralogical Sciences, Professor, Leading Researcher Institute of Automation and Electrometry of the Siberian Branch of the Russian Academy of Science (630090, Russia, Novosibirsk, Prospekt Akademika Koptyuga, 1). E-mail: kotlyarpe@iae.nsk.su AuthorID: 60366

Rules for submission, reviewing and publishing of scientific papers
(as revised in 2025)

1. The "Applied Physics" journal is mainly intended for urgent publication of short papers concerning recent achievements in physics that have a potential of applied (technical and scientific) use. The journal is included in the new List of the Higher Attestation Commission, which came into effect on December 1, 2015.

By sending the article manuscript to the journal's editorial board, the authors grant the editorial board, founder and publisher of the journal a free, non-exclusive right to publish it in Russian as an article in the printed version of the journal, in the electronic version of the journal in the Internet and on laser disks. At the same time the authors retain their intellectual rights to the article manuscript (including "copyright"). In this regard and considering Part Four (Section VII) of the Civil Code of the Russian Federation, the authors shall submit a letter to the editor in the following form:

License agreement for transfer of the publish right (publishing license agreement)

We, the undersigned, the manuscript authors _____, grant the editorial board, founder and publisher of "Applied Physics" journal a free, simple (non-exclusive) license to publish the article manuscript in both printed and electronic journal versions.

We confirm that this publication does not violate the intellectual rights of other persons or organizations. Signatures of authors: _____ (full name, academic degree, date)

The article shall be signed by all authors. If there are several authors, the name of the author responsible for message exchange with the editorial board shall be indicated. The article manuscript shall be sent to the address of the journal's editorial board: 111538, Moscow, Kosinskaya st, 9, AO NPO Orion, editorial board of "Applied Physics" journal or by e-mail: advance@orion-ir.ru

2. The article manuscript shall be submitted to the editor only in Russian.

3. The article manuscript shall be accompanied by an expert opinion whether its publication in the open media is allowed, which shall be drawn up in accordance with the established procedure.

4. The article size (including figures, bibliography and the English-language part) shall not exceed **7 pages** of A4 format with single line spacing. (A larger article is proposed to be sent to the affiliated **"Applied Physics Advances"** journal intended for publication of detailed articles and reviews). The article material shall be submitted in printed form (on paper) and in electronic form on a CD/DVD disk with the text in Word format (font type – Times New Roman, font size – 12), and the text shall already include figures with captions under them in the proper places. However, overly detailed and cumbersome mathematical transformations and expressions should be avoided in the text. The article styling shall be as follows:
  – title of the journal section;
  – UDK index;
  – PACS classification code (https://publishing.aip.org/wp-content/uploads/2019/01/PACS_2010_Alpha.pdf);
  – article title;
  – initials and surnames of authors;
  – abstract of the article (10–15 lines describing the purpose of the paper and its main findings);
  – keywords;
  – scientific specialty code.

5. The main text of the article shall begin with the "Introduction" section clearly stating the purpose and objectives of the paper along with arguments in favor of its preparation against the background of the existing state of the problem addressed in the article. The further text of the article shall also have meaningful headings (sections and subsections) without being numbered. The article shall end with a separate section, "Conclusion," listing the main findings, conclusions that follow from them, and, if possible, proposals for the research advance and use of its findings.

The bottom of the first page of the text shall accommodate a separate paragraph (in bold) containing contact information about the author (or authors) **(mandatory section)**: surname, first name, patronymic (in full), **e-mail (of all authors),** profiles and registration numbers in scientometric databases (SPIN code, RINTS Author ID, ArXiv Author ID, Orcid ID, Scopus Author ID), academic degree, title, position, postal address of the enterprise).

Also a person responsible for message exchange with the editorial board shall be specified.

Authors can suggest potential reviewers (2–3 people by indicating their full name, place of work, and email address). The proposed candidates shall not work in the institutions where the authors do.

The main text shall be followed by the list of references called "Bibliography".
Examples of designations of references used in the "Bibliography" section.

Articles shall be referred to as follows: Surname, initials, journal title, year, volume, issue, page numbers.
Ivanov I. I. / Applied Physics. 2022. No. 1. P. 12–18.
Lang D. V. / J. Appl. Phys. 1974. Vol. 45. No. 7. R. 3023–3034.
Reference to **books**: Surname, initials, book title, city, publisher, year. (When a specific chapter or page in a book is referred to, the page number is placed after the year.)
Korn G., Korn E. Mathematical Handbook. – Moscow: Nauka, 1974.
Biberman L. M., Vorobiev V. S., Yakubov I. T. Kinetics of non-equilibrium low-temperature plasma. – Moscow: Nauka, 1982. P. 371.
Ultraviolet technologies in the modern world / edited by Karmazinov F.V. Kostyuchenko S.V., Kudryavtsev N.N. – Dolgoprudny: Intellekt, 2012.

Reference to **conference proceedings:** Surname, initials, title of publication, place and date of publication, page numbers.
Romanov A. V., Stepovich M. A., Filippov M. N. / Proceedings of the XVII International Conference "Radiation Physics of Solids". – Sevastopol, 2007. P. 592–599.

Reference to **patents**: Surname, initials, title, type, number, year.
Davydov S. G., Dolgov A. N., Yakubov R. H. Vacuum spark gap. Patent of invention No. 2654494 (RF). 2018.

Reference to **dissertations and Abstracts**: Surname, initials, title of paper (abstract), diss. … Candidate (Doctor) of Physics and Mathematics, city, organization, year.
Grechikhin V. A. Development and analysis of computer algorithms for processing single-particle signals of laser Doppler anemometers: Abstract from diss. by Candidate of technical sciences. – Moscow: MPEI, 1996.

Further, detailed English-language information about the article required for indexing the entire journal, the given article and its authors in international scientometric databases shall follow, namely: PACS, article title, authors' surname and initials (English transliteration), enterprise, its postal address, author(s) e-mail, abstract, keywords, references; since the journal is also distributed abroad, the editorial board reserve the right to correct the English part of the text without changing its meaning.

Styling of the References in the English part of the article has its own peculiarities. In particular, if the cited book or monograph is a translation into Russian from a foreign publication, the original data of this publication (authors, book title, publisher, city or country, year of publication) shall be given, as well as the Russian publisher and the year of publication in Russian. Given below are the main examples of designation of used references in the References section:
Article from the journal:
Ivanov I. I., Applied Physics, No. 1, 12–18 (2022) [in Russian].
Lang D. V., J. Appl. Phys. **45** (7), 3023–3034 (1974).
Note: if a Russian journal has a printed English analogue, the English title of the analogue shall be used and page numbers shall be taken therefrom. If there is no English analogue, the English transliteration of the Russian name shall be used.

Book:
Korn G. and Korn E., Mathematical Handbook. New York-London, Mcgraw-Hill Book Company, 1968; Moscow, Nauka, 1974.
Ultraviolet technologies in the modern world / ed. Karmazinov F. V., Kostyuchenko S. V., Kudryavtsev N. N. Dolgoprudny, Intellect, 2012 [in Russian].

Conference proceedings:
Romanov A. V., Stepovich M. A., and Filippov M. N. Proc. XVII Intern. Meeting on Radiation Physics of Solid State. Sevastopol, 2007, pp. 592–599.

Patents:
Davydov S. G., Dolgov A. N., Yakubov R. H. Vacuum spark gap. Patent for invention No. 2654494 (RF). 2018.
Dissertations and Abstracts:
Grechikhin V. A. Development and analysis of computer algorithms for processing single-particle signals of laser Doppler anemometers: Abstract. Diss. Candidate of Technical Sciences. M., MEI, 1996.

6. The list of references ("References") shall correspond to all references to external sources used in the text of the article. These references shall be enclosed in square brackets, for example, [1–3], [7, 8]. Internal references, i.e. references to formulas, figures and tables of the article shall be enclosed in round brackets, for example, formula (3), equation (1), (Fig. 2), (Table 3). Any references in figure captions or in the figures are not recommended.

7. The number of figures and photos for a typical article shall not exceed 4. If one figure contains two, three or more variants of graphic (or photo) images of the type "Fig. 2*a*", "Fig. 2*b*", etc., each individual variant is considered as a separate figure. If the above limit number of figures (photos) is exceeded, the article is sent back to the authors for revision. Graphics (black and white and color) shall be put directly in the proper place in the article and in the proper scale. Next to the graph axes, the displayed physical quantities shall be indicated only (**strictly!**) using symbols (letters), and after a comma - the quantity dimension in Russian (in direct font). It is recommended to number different curves on graphs, even if they are identified by a different color or line type. Graphs shall be submitted only (**strictly!**) against the white background. Auxiliary grids are not allowed in the graph area.

8. Captions under the corresponding figures shall be out in the proper places in the text. Each caption shall be as short as possible, but meaningful in terms of its content. Any physical (technical) symbol included in the caption shall have its verbal explanation there.

9. Simple formulas shall be included in the text in the format of the text editor used; more complex formulas shall included using MathType formula editor. Standard mathematical notations (e.g. max, log, sin, exp, etc.) shall be typed directly. The same is true about figures and numbers. Formula numbers shall written in parentheses on the right. To indicate non-vector physical (technical) quantities using symbols, use only the Latin and Greek alphabets, while using a straight font for Greek letters, and an oblique font (italics) for Latin letters in the text. Vectors and matrices shall be marked by a bold, upright font (preferred) or an arrow above the italic vector symbol (less preferred). For subscripts and superscripts, use Arabic numerals, Latin or Greek letters, but if the index, usually a subscript, is a short (abbreviated) form of the Russian characteristic word, it is allowed to use Russian letters in its designation (uppercase font), for example U_{in}, I_{out}, v_{gr}, etc. The dimension of physical quantities shall be always given only in Russian, using an uppercase font.

10. Tables shall be made in accordance with the following requirements: the top line contains the data name and dimensions; the following lines contain the data itself.

11. Formulas, tables and figures shall have their own separate continuous numbering system. If there are no additional (return) references to a specific formula in the text or it is used only once, it shall not be numbered. A table and/or a figure used only once do not require numbering either.

12. Manuscripts and CD/DVD will not be sent back by the editorial board.

13. Authors (or an author) of each article after it is published in a journal issue have a right to receive an electronic version of the article in PDF format (Adobe Acrobat editor) from the editorial board.

14. When published in the journal, each article is accompanied by a footnote with the copyright symbol © placed before the author's name (authors' names). The article shall also specify the date the article was received by the editorial board.